Disequilibrium sulfur degassing - a mixed volatile bubble-growth model

Saskia Willar-Sheehan

How to cite:

Willar-Sheehan, Saskia (2026) Disequilibrium sulfur degassing - a mixed volatile bubble-growth model. Masters thesis, Durham University.

Academic Support Office, The Palatine Centre, Durham University, Stockton Road, Durham, DH1 3LE
e-mail: e-theses.admin@durham.ac.uk Tel: +44 0191 334 6107
https://etheses.durham.ac.uk

Disequilibrium sulfur degassing - a mixed volatile bubble-growth model

Saskia Faye Marie Willar-Sheehan

Abstract

Volcanic eruptions are driven by bubble growth in magma, caused by the exsolution of volatiles within the melt. The most important magmatic volatiles are H_2O and CO_2, as they are the most abundant and exert the largest control on bubble growth. As a result, most experimental work involving magma degassing involves a simplified H_2O-only, or H_2O-CO_2 system. However, the most important magmatic volatile used in volcano monitoring is SO_2, because it is much easier to identify as unambiguously volcanogenic compared to CO_2 and H_2O. Because of the relative scarcity of research into sulfur degassing, most interpretations made from SO_2 emission data assume equilibrium conditions; however, given the relatively slow diffusion of sulfur in silicate melts, it is likely that disequilibrium sulfur degassing is common in natural systems.

In this study, a mixed volatile bubble-growth model has been adapted to include H_2O, CO_2 and S, and accounts for the kinetic limitations of degassing, allowing disequilibrium behaviour to be modelled. In order to account for the effect of sulfur speciation on sulfur solubility, techniques from the degassing model *Sulfur_X* have been implemented. This new bubble-growth model simulates degassing of a one-, two- or three-volatile system in basalts, and can determine under what conditions disequilibrium degassing occurs.

Results suggest that disequilibrium degassing of sulfur occurs within the range of decompression rates found in natural basaltic systems, suggesting that it may be more prevalent than previously thought, and could be affecting observed emissions. By recreating the conditions of Fagradalsfjall 2021, it has been concluded that equilibrium degassing occurred during effusive episodes, and significant disequilibrium degassing occurred during fountaining episodes, at an estimated decompression rate of $\sim$1 MPa/s. Results from the model agree very well with natural data, supporting the applicability of this new model to natural systems, and its use in volcano monitoring efforts.

Disequilibrium sulfur degassing - a mixed volatile bubble-growth model

Saskia Faye Marie Willar-Sheehan

MScR
Department of Earth Sciences
Durham University
September 2025

Contents

1 Introduction

Volcanic eruptions pose a significant risk to populations worldwide, with an estimated 800 million people living within 100 km of an active volcano (Brown et al., 2015). Additionally, volcanic eruptions can have a significant effect on our climate, something increasingly important to understand as we face modern climate change. Reducing volcanic hazard is therefore a global priority, requiring advances in volcano monitoring and continued development of eruption forecasting.

One of the most important tools in volcano monitoring is gas geochemistry, which can provide insight into eruption processes, magma transport at depth and magma storage conditions (Shinohara, 2008). Understanding volcanic gas output is also crucial for understanding climatic impacts, especially those associated with volcanic sulfur (Cole-Dai, 2010). By furthering understanding of volcanic gas geochemistry, particularly sulfur, more confident interpretations from gas emissions can be made, helping to improve volcano monitoring efforts and our ability to predict changes in eruptive behaviour. This study investigates the degassing of three main magmatic volatiles: H_2O, CO_2 and S, in order to constrain their behaviour under different conditions, and better understand their observed emissions.

1.1 Magmatic volatiles

Volcanic eruptions are driven by volatiles dissolved at depth. The most abundant is by far H_2O, followed by CO_2, S, Cl, F, and others in very small concentrations (Wallace et al., 2015). When magma rises and pressure decreases, the solubility (the ability to dissolve) of these volatiles drops, causing them to exsolve and form gas bubbles (Sparks, 1978). These bubbles increase the buoyancy of the magma, causing it to rise and experience further decompression, generating a positive feedback cycle resulting in a volcanic eruption (Wallace et al., 2015). Eruption style is also determined by volatiles, as factors such as bubble growth depth and rate can affect the pressure within the bubble (Wallace et al., 2015). Overpressure results in magma fragmentation, a key driver of explosive eruptions (Proussevitch & Sahagian, 1998). Magmatic volatiles are therefore the main drivers of volcanic eruptions and their explosivity, and understanding how they behave while degassing is vital for understanding the nature of volcanic eruptions, and reducing volcanic hazard.

Understanding bubble nucleation and growth within magmas is therefore needed in order to understand how these volatiles degas. Research into bubble nucleation and growth must be done experimentally and computationally, due to the inability to observe these processes at depth. As a result, numerical modelling is frequently used to simulate the exsolution of magmatic volatiles under different conditions (e.g. Proussevitch & Sahagian, 1998; Toramaru, 1995; Coumans et al. 2020), as well as laboratory experiments at high pressure and temperature (e.g. Martel et al., 2003, Toramaru et al., 2008). Such studies have provided insight into the mechanisms behind bubble nucleation and the main influential parameters.

The two main mechanisms behind bubble nucleation are homogeneous nucleation (without the assistance of other phases) and heterogeneous nucleation (on the surface of pre-existing crystals), with heterogeneous nucleation being able to occur at lower supersaturation pressures (Shea, 2017). The conditions for nucleation are controlled by composition (and importantly, the presence of crystals), volatile concentration and decompression rate (Gardner et al., 2022). All of these factors determine how volatiles exsolve from the magma, and are important for controlling the style of eruption.

1.1.1 H_2O and CO_2

The most important magmatic volatile is considered to be H_2O, as it is the most abundant and therefore is the main control on bubble growth, magma fragmentation and eruption explosivity, as well as other parameters such as melt viscosity (Wallace et al., 2015). CO_2 is also abundant, especially in mafic magmas, and so can also be considered an important volatile in affecting bubble nucleation and growth (Johnson et al., 1994). Importantly, CO_2 is far less soluble in silicate melts than H_2O, so the presence of CO_2 can initiate bubble nucleation at a much greater depth than in an H_2O-only system (Gardner et al. 2022). This is shown in Figure 1, which is adapted from Iacono-Marziano et al., (2012) and shows H_2O and CO_2 solubilities.

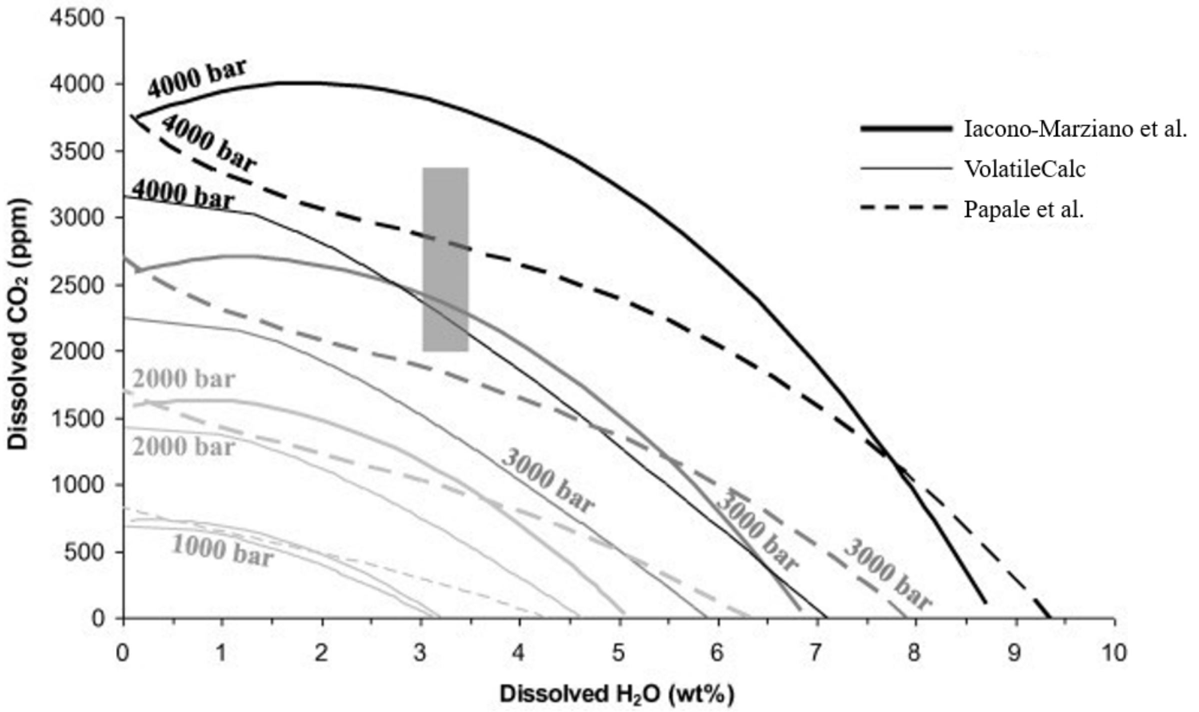

Figure 1: *Adapted from Iacono-Marziano et al., (2012). Results from three models (Iacono-Marziano et al. 2012, VolatileCalc (Newman & Lowenstern, 2002) and Papale et al. 2006) show mixed H_2O-CO_2 solubility. It can be seen that the amount of dissolved H_2O at a constant pressure (i.e. an isobar) varies greatly with dissolved CO_2 concentration, illustrating how the presence of CO_2 greatly impacts the solubility of H_2O, with more CO_2 allowing H_2O to exsolve at higher pressures.*

There are currently many existing models to describe the degassing of H_2O and CO_2, most of which describe their solubility under different conditions (e.g. Iacono-Marziano 2012, Ryan et al., 2015, Liu et al., 2005). Models also exist to describe their diffusivities in silicate melts (e.g. Zhang & Ni 2010, Zhang 2007), and Coumans et al., (2020) presents a more complex system combining these to produce a model for bubble growth of H_2O. Most experimental studies into magma degassing, including numerical models, have only considered H_2O (and sometimes CO_2, e.g. Yoshimura 2015) as the exsolving species, and assumed the less abundant volatile phases to have a negligible effect on the physics of bubble nucleation and growth (e.g. Coumans et al. 2020). However, it is the volatiles that have less of an effect on the physics that are largely used in gas geochemistry monitoring, and so this study aims to bridge this gap by incorporating sulfur into a model of physical properties of magma degassing.

1.1.2 Sulfur

There is very limited data on the supersaturation and bubble growth of other magmatic volatile phases, most significantly SO_2, which is used extensively in volcano monitoring. Understanding the degassing mechanisms of sulfur in magmatic systems therefore has large implications for how we interpret gas emissions from volcanic eruptions. Unlike H_2O and CO_2, SO_2 has few other natural sources, and so is often measured and used as a proxy for changes in volcanic activity. For example, this has been extensively done on Kilauea since the 70s, and shifts in emission rates have been correlated with eruptive episodes (Elias et al., 1998). Sulfur emissions are also used to make interpretations on processes occurring at depth, such as magma recharge (Wallace et al., 2011) and magma recycling (Lerner et al., (2021). However, despite sulfur's wide use in volcanology, there is still ambiguity around its solubility (Baker et al., 2011), diffusivity (Freda et al., 2005) and degassing behaviour (Sharma et al., 2004). While a lot of recent work has been done to reduce these ambiguities (e.g., O'Neill & Mavrogenes, 2022; O'Neill et al., 2018; Boulliung & Wood, 2022; Boulliung & Wood, 2023; Lesne et al., 2011; Masotta et al., 2016; Zajacz et al., 2012; Ding et al., 2023; Hughes et al., 2023), it is still important to understand how sulfur degases in volcanic systems in more detail, in order to justify our use of sulfur emissions and the interpretations made from them. There are currently very few degassing models which incorporate sulfur, most notably *D-Compress* from Burgisser et al., 2015 which simulates equilibrium degassing, and *SolEx* from Witham et al., 2012 which calculates mixed volatile solubility and exsolved gas composition.

1.2 Disequilibrium degassing of volatiles

An important mechanism to understand within volcanic eruptions is disequilibrium degassing. When volatiles exsolve from the melt, they must first diffuse through the melt via a chemical gradient and enter a bubble. The ability to exsolve is therefore defined by a timescale, relating to the distance travelled through the melt to reach a bubble (the lengthscale, L), and the volatile's diffusivity (D). The time needed for a volatile to exsolve from the melt can be described using Equation 1 (Okumura & Hirano, 2013).

$$t = \frac{L^2}{D} \tag{1}$$

Disequilibrium degassing refers to when the melt becomes supersaturated with a volatile because it cannot exsolve fast enough (i.e. the degassing time is less than the timescale of diffusion), resulting in a chemical disequilibrium between the melt and the fluid (Mangan & Sisson, 2000). By studying bubble nucleation and growth, it can be determined whether a system experiences disequilibrium or equilibrium degassing, which can affect fragmentation and therefore explosivity, and is determined largely by decompression rate and the effectiveness of volatile exsolution (Mangan & Sisson, 2000). While the extent of disequilibrium degassing of H_2O and CO_2 is fairly well studied (e.g.

Yoshimura 2015, Johnson et al., 2010), this is not the case for sulfur. Closed-system equilibrium degassing of sulfur has been modelled (e.g. Lerner et al. 2021, Burgisser et al., 2015), but such models do not take into account the relatively slow diffusion rates of sulfur (~ 10^{-12} m^2/s at 1150 °C; Behrens & Stelling, 2011). This could prove very significant, as slower diffusion rates coupled with sulfur's tendency to degas at shallow depths (Lerner et al., 2021) could mean that in natural systems, there is not enough time for sulfur to exsolve, leading to extensive disequilibrium degassing. This may have implications for interpretations from sulfur emissions, which assume total equilibrium degassing (e.g. Scaillet et al., 2003). It is therefore important to account for the kinetic effects which may limit sulfur degassing and alter volatile concentrations in samples.

1.3 Study motivation

While models for volatile degassing have been described in the previous sections, none are able to model a mixed H_2O-CO_2-S system, and account for the kinetic limitations during degassing. Therefore, a comprehensive degassing model incorporating the effects of bubble growth, volatile solubilities, diffusion and sulfur speciation is required to more accurately represent degassing of the three main volatiles in magmatic systems, and exhibit disequilibrium behaviour. This study aims to take the approach of Coumans et al., (2020), and extend it to include CO_2 and most importantly, sulfur, in order to more accurately recreate the processes ocurring in natural systems. A comprehensive, mixed volatile, disequilibrium degassing model could have applications in both experimental work and natural systems, by reproducing observed volatile concentrations to constrain degassing histories, and calculating important parameters such as saturation depths and the amount of each volatile in the vapour phase at different points in time. It could also have a large impact on volcano monitoring, by helping to more accurately interpret SO_2 emissions and, for the first time, be able to provide insight on whether the system could be experiencing disequilibrium degassing. Such information can be invaluable for forecasting future eruptive behaviour. By improving our understanding of these small-scale processes, the accuracy of volcano monitoring and eruption forecasting can be improved, helping to reduce volcanic hazard.

2 Background

In order to model volatile degassing, it is important to understand the physical behaviours of each volatile. In order for volatiles to degas from a magma, the melt needs to become supersaturated. This is determined by the solubility of the volatile, which changes depending on factors such as pressure, temperature and composition. In order for the volatile to exsolve, it must diffuse through the melt and enter a bubble. Therefore diffusivity is also an important control on volatile degassing, as it determines how quickly the melt can re-equilibrate with changing conditions. Previous studies of magma degassing have been able to constrain the solubilities, diffusivities and speciation of different magmatic volatiles, all of which are necessary for numerical modelling (e.g. Iacono-Marziano et al., 2012, Zhang et al., 2007, Coumans et al., 2020).

Additionally, information on volatiles' solubilities and diffusivities can be used to interpret natural samples. Melt inclusions formed at depth can provide a valuable snapshot of pre-eruptive conditions, and models for solubility and diffusivity can be used to interpret volatile concentration profiles, providing estimates such as saturation depth and degassing regime (Moore, 2008).

Studies into magmatic volatile solubility and diffusivity are therefore crucial for gas geochemistry, and an integral part of understanding magmatic degassing.

2.1 H_2O

Due to the importance of H_2O in magmatic systems, the physical behaviours of H_2O are well studied and well constrained. Experimental work has allowed the solubility and diffusivity of H_2O in silicate melts to be investigated, and this information is used to interpret natural samples (Moore, 2008).

2.1.1 Solubility

In order to understand H_2O degassing, the solubility of H_2O as a function of pressure, temperature and composition must be known. This has been investigated through experimental work since the 1950s (e.g. Tuttle & Bowen, 1958; Burnham & Jahns, 1962; Hamilton et al., 1964). In order to constrain solubility, a known fluid-saturated composition is equilibrated under known P-T conditions, and then quenched to a glass (Moore, 2008). The dissolved volatile content in the resulting glass is then determined. In the case of a mixed-volatile system, the concentration of each volatile in the vapour phase must also be constrained (Moore, 2008).

In order to constrain H_2O solubility, it is important to understand how H_2O dissolves in silicate melt and its speciation. H_2O dissolves in silicate melt in at least two species: H_2O molecules (H_2O_m), and OH^- groups bonded to network-forming cations, such as Si–OH, Al–OH, Na–OH etc. (Scholze, 1960). When dissolved H_2O_m reacts with the network to form OH^- groups (Equation 2), Si–O–Si links are disrupted, which modifies the silicate network and depolymerises the melt. This is why dissolved H_2O has such a large effect on melt properties (Zhang, 1999).

$$H_2O_{(\mathrm{melt})} + O^{2-}_{(\mathrm{melt})} \rightleftharpoons 2\,OH^-_{(\mathrm{melt})} \tag{2}$$

The development of the Fourier Transform Infrared (FTIR) technique in the 1980s and 90s allowed the speciation of dissolved H_2O to be directly measured, facilitating further studies into H_2O solubility and the factors affecting speciation (Moore, 2008). At low total H_2O content (H_2O_t) in the melt, OH^- is the dominant species, and the importance of H_2O_m increases as H_2O_t increases (Figure 2, Moore, 2008). This therefore strongly determines the solubility behaviour of H_2O (Zhang, 1999).

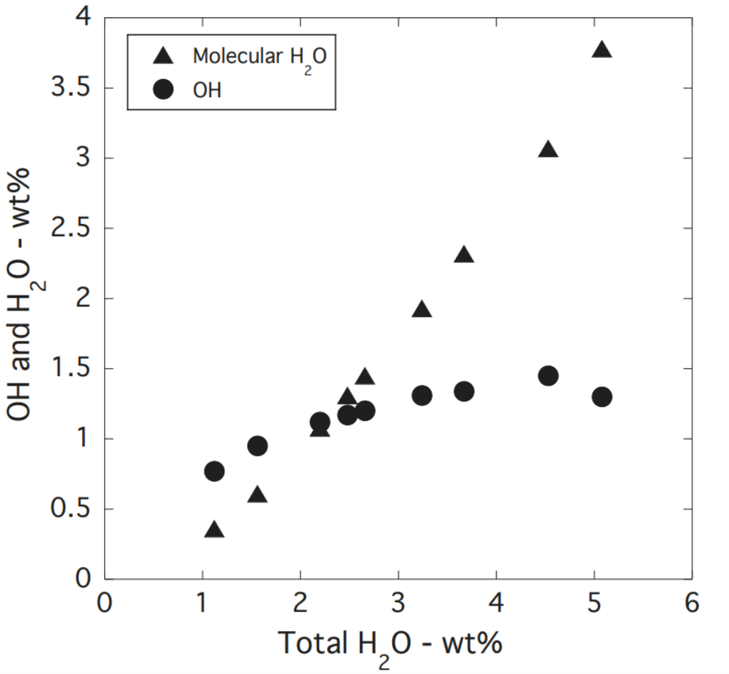

Figure 2: *From Moore (2008). H_2O speciation of dissolved H_2O versus total H_2O in rhyolite, measured using FTIR spectroscopy. At low total H_2O content, OH^- is the dominant species, but this changes to H_2O_m as total H_2O content increases.*

By understanding H_2O speciation, it has been possible to determine how different factors affect H_2O solubility, and develop empirical and thermodynamic models for calculating the equilibrium H_2O_t content in the melt under certain conditions.

For example, at low pressures, the solubility of H_2O_t is lower, and OH^- the dominant species. Therefore, H_2O_t is roughly proportional to the square root of the pressure. Similarly, at high pressures, the solubility of H_2O_t is higher, and H_2O_m the dominant species. Therefore, H_2O_t solubility increases more significantly than the square root of the pressure (Zhang, 1999).

In general, H_2O solubility is highly pressure dependent, to some extent dependent on temperature, and sensitive to changes in composition at higher pressures (Mysen, 1977). A general overview of H_2O solubility is displayed in Figure 3.

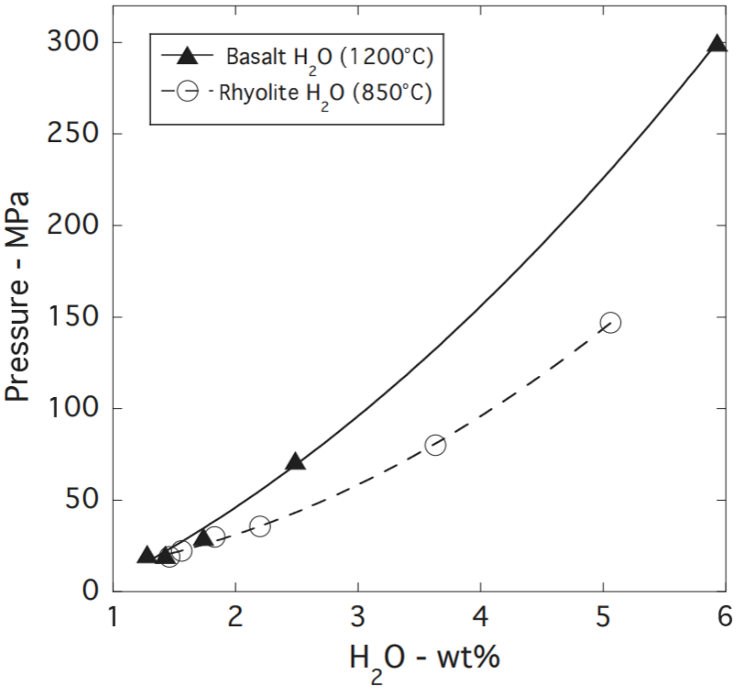

Figure 3: *From Moore (2008). Pure* H_2O *solubility in silicate melts, for mafic and silicic compositions. The basalt data is at 1200 °C (Hamilton et al. 1964; Dixon et al. 1995) and the rhyolite is at 850 °C (Silver et al. 1990).*

It can be seen that the difference in solubility of H_2O in rhyolites versus basalts is less significant at lower pressures, but at higher pressures the lower solubility of H_2O in basalts becomes prevalent. It has also been shown that adding alkalis also greatly increases the solubility of H_2O (e.g. Larsen & Gardner, 2004). This is due to the melt structure being more able to accomomdate OH^- groups (Ni et al., 2015).

There are an abundance of models for H_2O solubility in various compositions available in the literature, some of the most widely-used being VolatileCalc (Newman & Lowenstern, 2002), MafiCH (Allison et al., 2022), which both model melt-vapour equilibria using H_2O solubility models (VolatileCalc uses Dixon et al., 1995 and Silver (1988), and MafiCH incorporates the model of Lesne et al., 2011). Widely used empirical models include Iacono-Marziano et al., (2012) and Liu et al., (2005).

2.1.2 Diffusivity

Like solubility, H_2O diffusivity is largely dependent on speciation, and data is mainly collected experimentally. Such studies usually involve hydrating a sample by exposing it to H_2O vapour or fluid, and juxtaposing it against a dehydrated sample. Diffusion profiles are then measured using a variety of techniques, though infrared spectroscopy allows for H_2O_m and OH^- to be measured separately (Zhang & Stolper, 1991). More modern examples of such studies include Behrens, (2010), Zhang & Ni, (2010), and Zhang et al., (2010).

Coupled speciation and diffusivity studies have allowed the effects of H_2O speciation on diffusivity to be determined (e.g., Zhang & Stolper, 1991). One of the most important effects is the depolymerisation of the melt from the formation of OH^- groups. As H_2O dissolves, it reacts with oxygen in the melt and forms OH^- groups bonded to network formers (cations which form a network of tetrahedra linked by oxygen atoms, Zhang & Gan, 2022); this reaction is shown in Equation 2. This interferes with the silicate structure of the melt and depolymerises it, facilitating easier diffusion of molecules through the melt. However, the main diffusing species of H_2O is H_2O_m, not OH^-, because it is a neutral molecule and does not need to break strong bonds in order to diffuse (Zhang & Ni, 2010). Therefore the diffusivity of H_2O is proportional to H_2O_m (Zhang & Stolper, 1991).

As well as H_2O content and speciation, other important parameters affecting diffusivity are pressure, temperature, composition and redox contitions. However, while it has been suggested that increasing oxygen fugacity converts more Fe^{2+} to Fe^{3+} and therefore repolymerises the melt and inhibits diffusion, the full effect of redox conditions on diffusivity is still unconstrained (Ni et al., 2015).

The effect of temperature on H_2O diffusivity follows the general trend for all volatiles in silicate melt. This is known as the Arrhenian relationship, which describes how increasing temperature exponentially increases diffusion, as more molecules can overcome the activation energy barrier (Zhang & Gan, 2022). A summary of H_2O diffusion with temperature in basalts is shown in Figure 4 from Zhang et al., (2007).

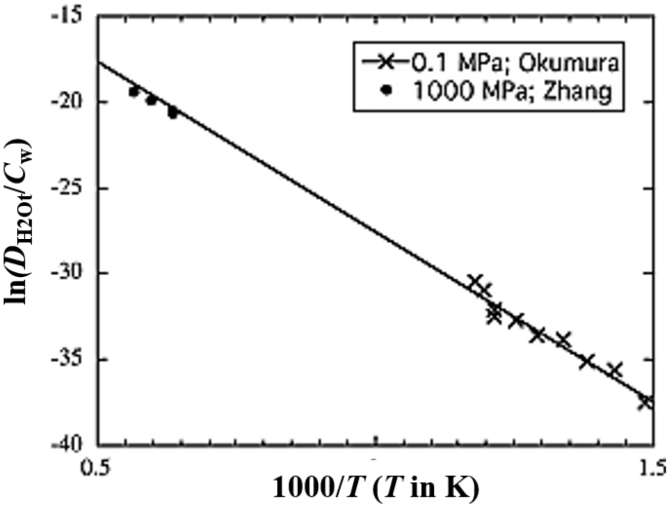

Figure 4: *From Zhang et al., (2007). Diffusivity of H_2O in basaltic melts. The vertical axis is* $\ln\left(\frac{D_{H_2Ot}}{C_w}\right)$*, where* D_{H_2Ot} *is* H_2O_t *diffusivity in* $m^2\,s^{-1}$ *and* C_w *is* H_2O_t *in wt.%. Data sources are Zhang & Stolper (1991) and Okumura & Nakashima (2006).*

The relationship with pressure is more complicated, and much weaker. Pressure can either increase or decrease the diffusivity, depending on composition, temperature and current pressure (Zhang & Gan, 2022). For this study, the diffusivity of H_2O in basalts is of interest, for which there is thought to be a negligible pressure effect (Zhang et al., 2007).

H_2O diffusivity is also dependent on the major oxide composition of the melt, due to the silicate structure and degree of polymerisation affecting how easily H_2O_m can move through the melt. This is however complicated and there is no theoretical formulation. Generally, the diffusivity in dry basaltic melt is higher than in dry rhyolite melt under the same conditions (Zhang & Gan, 2022).

There are several empirical models for H_2O diffusivity in different compositions of silicate melts, most notably those from Zhang & Ni (2010) due to their broad compositional and temperature applicability.

2.2 CO_2

CO_2 is the second most abundant magmatic volatile, and so like H_2O, the physical behaviours of CO_2 are well studied due to its importance in driving magma degassing. Studies since the 1960s have aimed to constrain solubility and diffusivity of CO_2, and investigate the main influential parameters (Lowenstern, 2001).

2.2.1 Solubility

The solubility of CO_2 in silicate melts is around an order of magnitude lower than H_2O, meaning at magma storage depths, CO_2 is the primary volatile in the exsolved phase (Lowenstern, 2001). This means there has been extensive research into the solubility of CO_2 in silicate melts, using similar experimental techniques as for H_2O.

The solubility of CO_2 in silicate melts is largely determined by its speciation. Like H_2O, it can dissolve as either molecular CO_2 or as carbonate groups, bonded to network modifiers. This reaction is shown in Equation 3 (Blank & Brooker, 1994).

$$CO_{2\,(\mathrm{melt})} + O^{2-}_{(\mathrm{melt})} \rightleftharpoons {CO_3}^{2-}{}_{(\mathrm{melt})} \tag{3}$$

In basaltic melts, the preferred dissolving species of CO_2 is as carbonate groups, and as molecular CO_2 in rhyolitic melts. Intermediate compositions contain significant amounts of both species (Mysen et al., 1975). Composition therefore has a large effect on the solubility of CO_2, and different models are required to describe these different behaviours.

In more mafic melts, because CO_2 dissolves to form carbonate groups which react with certain cations, its solubility is largely determined by the abundance of these cations, particularly Ca, K and Na (Lowenstern, 2001). Therefore, like H_2O, CO_2 is far more soluble in more alkali-rich basalts than tholeiites (Blank & Brooker, 1994). Importantly, CO_2 solubility does not vary much within the range of felsic compositions, as molecular CO_2 does not react with the melt (Lowenstern, 2001).

CO_2 solubility is also pressure-dependent. For all compositions, the solubility of CO_2 increases almost linearly with pressure (Lowenstern, 2001). This relationship is shown in Figure 5.

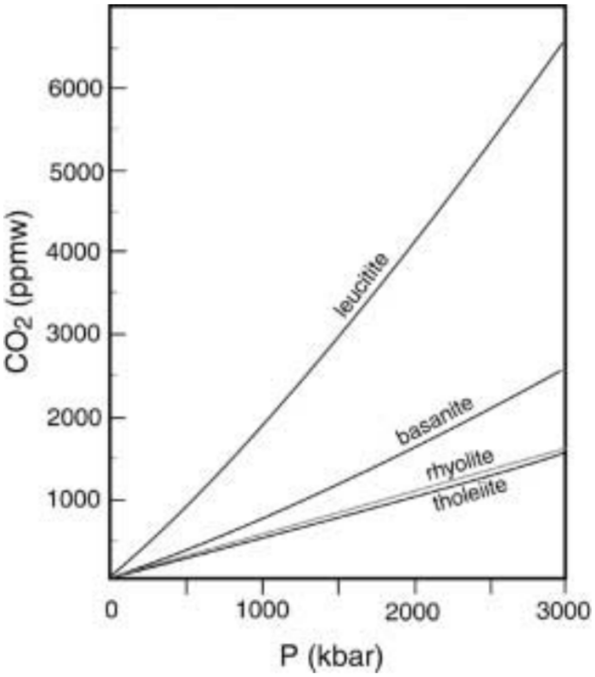

Figure 5: *From Lowenstern (2001). The solubility of total CO_2 with pressure, for four different compositions (ppmw parts per million per weight). Data from Holloway & Blank (1994) and Fogel & Rutherford (1990).The solubility of rhyolite and tholeiite basalt are very similar, and solubility increases with both pressure and magma alkalinity.*

It can be seen that the CO_2 solubility in rhyolite and tholeiite is very similar, because tholeiites do not contain as many Ca, K and Na cations as other basalts for the carbonate groups to bond with, reducing CO_2 solubility to similar levels as in rhyolites.

It is important to note that CO_2 solubility is also sensitive to temperature. In rhyolite compositions, the solubility of CO_2 decreases as temperature increases, in line with the typical inverse correlation between molecular gas solubility and temperature (Lowenstern, 2001). However, in general, the effect of temperature on CO_2 solubility is very small compared to those of pressure and composition (Blank & Brooker, 1994).

Due to the large variations in CO_2 solubility with composition, there are many models for CO_2 solubility covering a wide range of compositions. There is often very little agreement between these models, and so they must be used carefully and for the same composition as their calibration data. Figure 6 shows some of the most widely used CO_2 solubility models, and the discrepancies between them. For the purposes of this study, the model from Iacono-Marziano et al., (2012) is the most appropriate due to its empirical nature and ability to vary melt composition.

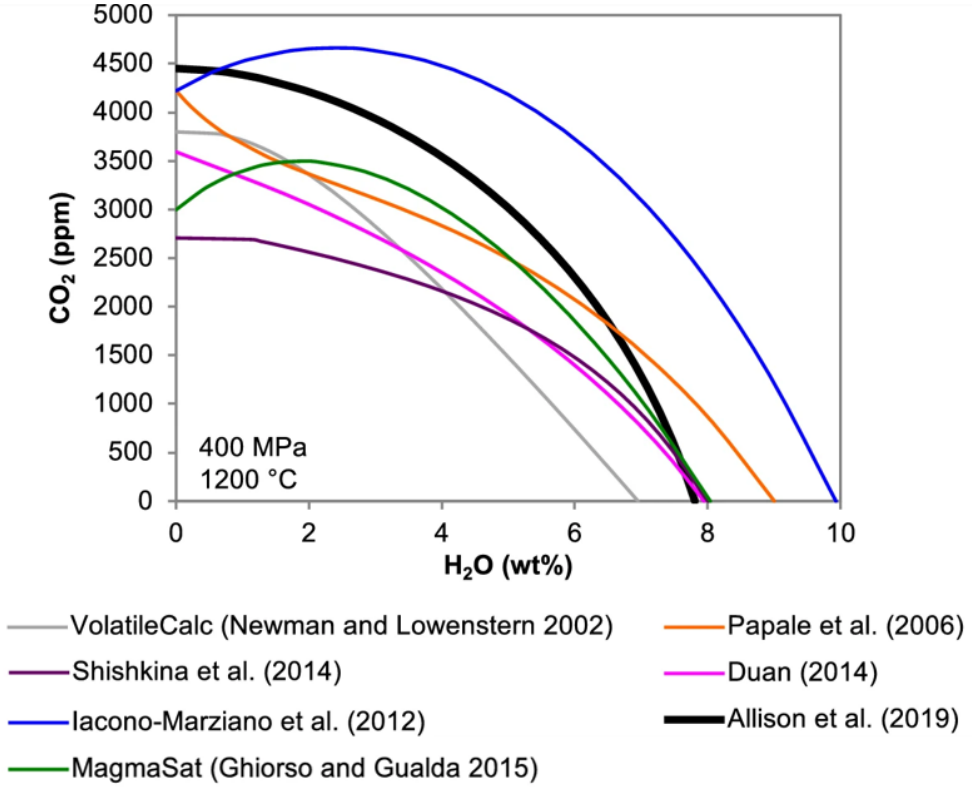

Figure 6: *Adapted from Allison et al., (2022). Summary of published CO_2 solubility models for mafic magmas, compared using an Etna composition at 1200°C.*

2.2.2 Diffusivity

CO_2 diffusivity depends on pressure, temperature and H_2O content. Its relationship with temperature is the same as H_2O, with increasing temperature increasing the diffusivity following an Arrhenian relationship, which is shown in Figure 7 (Zhang & Ni, 2010).

Importantly, CO_2 diffusivity is independent of anhydrous melt composition. This is surprising considering CO_2 dissolves as multiple species, but this actually creates this independence. Similar to H_2O, dissolved carbonate groups can be considered immobile, since they form strong bonds that require breaking in order to diffuse. Therefore molecular CO_2 is the only dissolved CO_2 species that diffuses under magmatic conditions. From a rhyolitic composition to basaltic composition, the diffusivity of molecular CO_2 increases (this is due to many factors, namely the reducing viscosity), increasing the total diffusivity of CO_2. However, the fraction of dissolved CO_2 as molecular CO_2 also decreases from rhyolite to basalt, decreasing the total CO_2 diffusivity. These two behaviours cancel each other out, making total CO_2 diffusivity independent of anhydrous melt composition (Zhang & Ni, 2010).

This makes CO_2 the only known magmatic volatile for which a general expression for diffusivity can be found (see Equation 24, Zhang et al., 2007). Total CO_2 diffusivity (D_{CO_2}) under different conditions using this general expression is shown in Figure 7.

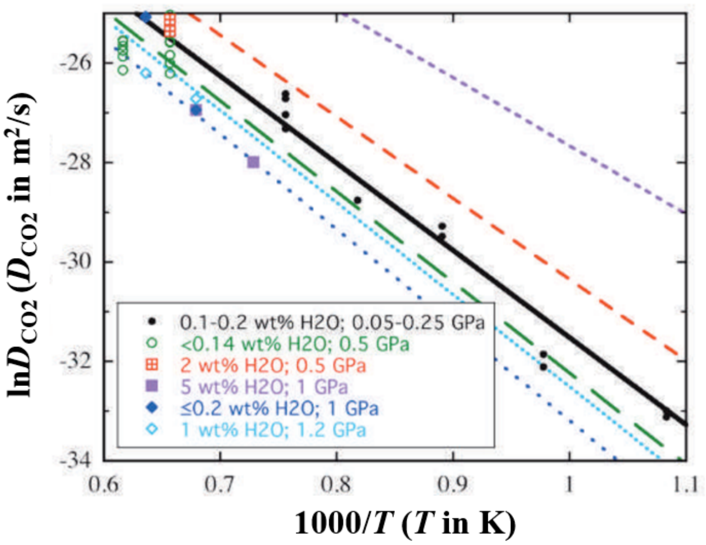

Figure 7: *Adapted from Zhang & Ni, (2010). Comparison of experimental data of CO_2 diffusivity with the general expression for CO_2 diffusivity from Zhang et al., (2007) under different conditions. Data sources: Blank (1993); Fogel & Rutherford (1990); Sierralta et al. (2002); Nowak et al. (2004); Baker et al. (2005); Zhang & Stolper (1991).*

CO_2 diffusivity is also dependent on total H_2O content, due to the depolymerisation of the melt as OH^- groups bond with network formers (see Equation 2). As a result, CO_2 diffusivity depends exponentially on OH^- content, and hence with total melt H_2O content, which is illustrated in Figure 8 (Zhang et al., 2007).

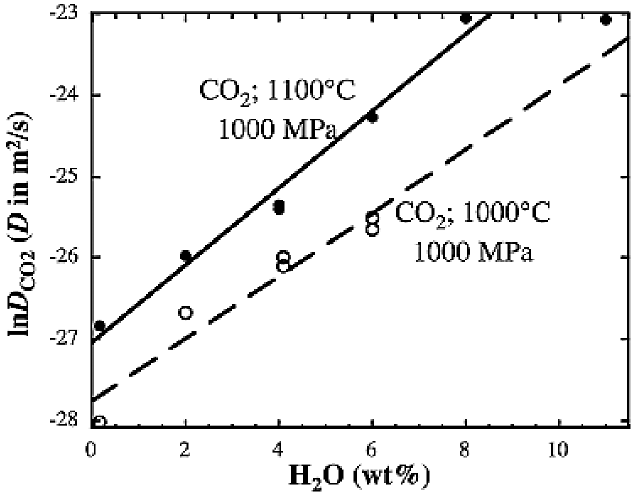

Figure 8: *From Zhang et al., (2007). CO_2 diffusivity as a function of H_2O content in the melt, for two different temperatures. Data from Watson (1991).*

Compared to the other parameters, pressure does not have a large effect on CO_2 diffusivity, though it follows an Arrhenian relationship similar to temperature, and generally pressure inhibits diffusion (Ni et al., 2015).

In general, the diffusivity of CO_2 is less than that of H_2O (Zhang & Ni, 2010). Additionally, it is important to note that while H_2O diffusivity is strongly dependent on its own concentration, the diffusivity of CO_2 is not, and is only dependent on H_2O concentration (Zhang & Ni, 2010).

2.3 Sulfur

The degassing of sulfur within magmatic systems is complex, due to the saturation of an immiscible liquid or solid phase (Gardner et al., 2022). Notable studies on sulfur degassing include Burgisser & Scaillet (2015), Aiuppa et al., (2007), Metcalfe et al., (2023) and Ding et al., (2023). However, more research is needed to address these complexities, including the incorporation of sulfur diffusion in silicate melts.

2.3.1 Solubility

In order to investigate the supersaturation and bubble formation of sulfur-bearing species, the solubility of sulfur in silicate melts needs to be constrained. This problem is complex, as sulfur has multiple oxidation states, therefore altering the dissolving species depending on the oxygen fugacity of the system (Boulliung & Wood 2022). Unlike H_2O and CO_2, sulfur-bearing gases do not dissolve in their molecular form, instead in reducing conditions ($<\Delta$FMQ+2), sulfur tends to dissolve as sulfide (S^{2-}), and in oxidising conditions($>\Delta$FMQ+2), as sulfate ($SO_4{}^{2-}$) (Fortin et al. 2015). This means sulfur solubility in silicate melts is highly sensitive to redox conditions, as is shown in Figure 9 from Fincham & Richardson (1954).

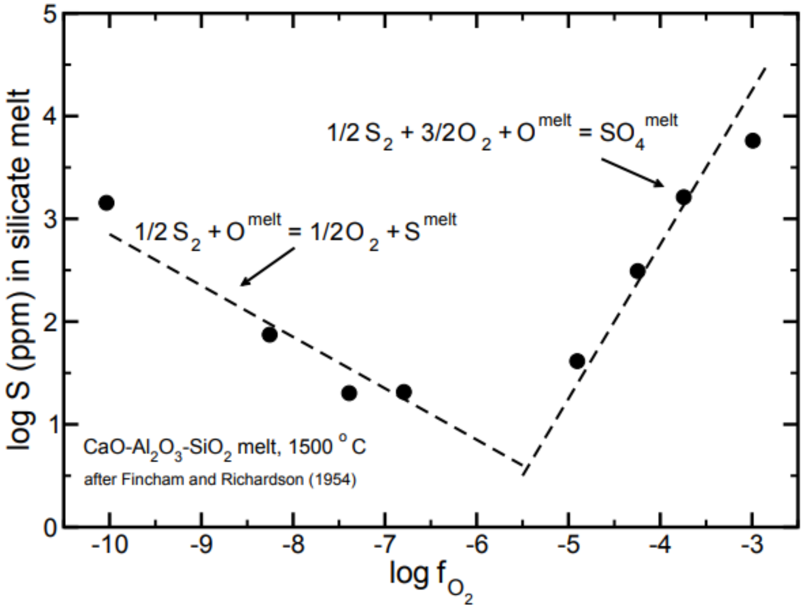

Figure 9: *From Fincham & Richardson (1954). Sulfur solubility in silicate melts with varying* fO_2*. The change in the dominant speciation reaction occurs at around -5.5 log* fO_2*, where sulfur solubility is at a minimum.*

Furthermore, when saturated, these two phases can exsolve and form immiscible solid or liquid phases that coexist with the silicate melt. S^{2-} often forms an immiscible liquid or pyrrhotite, and $SO_4{}^{2-}$ commonly forms anhydrite (Baker & Moretti, 2011). Therefore, the maximum sulfur concentration of the melt is determined by the concentration at sulfide (SCSS) or anhydrite saturation (SCAS). The complexity of additional sulfur phases makes modelling sulfur degassing extremely difficult due to the ambiguity of mass balance, and so the only current degassing model able to account for the presence of saturated S^{2-} and/or $SO_4{}^{2-}$ phases is that of Sun & Yao, (2024). However, the SCSS and SCAS have been constrained in the form of several empirical and thermodynamic models, developed from experimental studies (e.g. Haughton et al. 1974, Liu et al. 2007, Baker & Moretti, 2011). Such studies involve equilibrating a silicate liquid with a gas phase containing a known fugacity of S_2 and O_2. The liquid is quenched to a glass, and the dissolved S content determined. the saturation of the glass with an additional sulfide phase can be used to determine the SCSS under the conditions of the experiment (e.g. Haughton et al., 1974). The empirical models developed from these experiments allow for the determination of whether an additional, immiscible sulfur phase is present under certain conditions. The effects of pressure and temperature on the SCSS for anhydrous basaltic and andesitic melts are shown in Figure 10 from Wendlandt (1982).

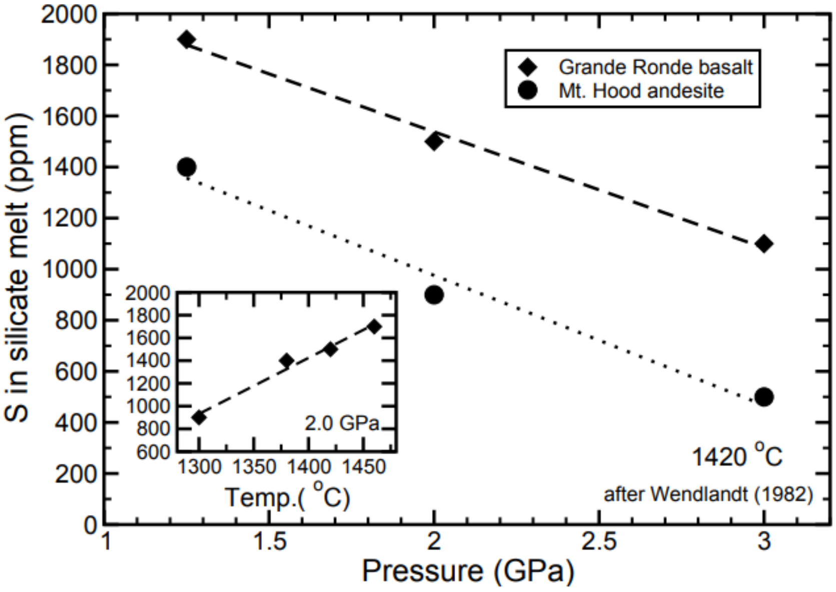

Figure 10: *From Wendlandt (1982). The effects of pressure and temperature (see inset) on the sulfur concentration at sulfide saturation (SCSS).*

Sulfur degassing therefore cannot be defined using simple solubility relationships like H_2O and CO_2, because at saturation additional sulfur phases form. Alternatively, sulfur solubility can be expressed as sulfide and sulfate capacities. Boulliung & Wood (2023) model sulfur degassing by calculating which is the dominant dissolving sulfur species, and then calculating the sulfide or sulfate capacity based on empirical models from experimental data. This method however does not account for sulfide/sulfate saturation, and works by calculating the maximum dissolved sulfide/sulfate concentration in the melt at which it remains undersaturated in an additional sulfur phase. The change in the concentration of dissolved sulfide or sulfate at each timestep (varying pressure and/or temperature) allows the amount of sulfur degassed to be calculated. While this allows equilbrium melt concenrations to be calculated, this method is limited due to the large generalisation of assuming a dominant sulfur species. Another way of describing sulfur solubility that overcomes the issue of multiple sulfur species is the use of a partition coefficient. In experimental studies where an additional sulfur phase has not formed, and the partial pressures of SO_2 and H_2S in the vapour phase are known, the partition coefficient between the sulfur in the melt and in the vapour phase can be determined (Wallace & Carmichael, 1992). Such partition coefficients can be used to model sulfur degassing, because as other volatiles (mainly H_2O and CO_2) exsolve due to the decrease in pressure, a certain proportion of sulfur fractionates into the vapour so that its concentration in the melt gradually decreases (Witham et al., 2012). This approach has been used by several models for sulfur degassing, to avoid the problem of calculating equilibrium melt concentrations of multiple sulfur species (e.g. Witham et al., 2012, Ding et al., 2023). However, it is also important to note other approaches that have been taken to address sulfur solubility when modelling sulfur degassing, such as sulfide and sulfate capacities (e.g. Moretti & Papale, 2004; Burgisser et al., 2015), and redox equilibria of iron (Sun & Yao, 2024).

The partitioning of sulfur between the melt and vapour phases (the partition coefficient) is described as the ratio of molar concentrations:

$$K_{d,S}^{v/m} = \frac{X_S^{\text{vapour}}}{X_S^{\text{melt}}} \tag{4}$$

Where X_S^{vapour} and X_S^{melt} are the mole fractions of sulfur in the vapour and melt (Ding et al., 2023).

K_d has been constrained from experimental studies (e.g. Burton et al., 2007) and melt inclusion data (e.g. Johnson et al., 2010), and several models exist for calculating its value under different conditions, such as *SolEx* (Witham et al., 2012) and *Sulfur_X* (Ding et al., 2023). However, because of sulfur's multiple dissolving species, additional phase saturation and sensitivity to redox conditions, such partition coefficients are specific to the experimental conditions they were determined from. For example, *SolEx* is only applicable to sulfur concentrations low enough to inhibit saturation, and under reducing conditions so S^{2-} is the dominant dissolving species. This greatly limits current models of sulfur degassing, resulting in large disagreement between them (Ding et al., 2023).

This limitation of partition coefficients is addressed in *Sulfur_X*, which utilises the approach of a combined partition coefficient, to describe the behaviours of both S^{2-} and SO_4^{2-}. In this study, we adopt the approach used in *Sulfur_X*, due to the importance of incorporating the effects of sulfur speciation. This approach is briefly outlined below (for a full explanation of *Sulfur_X* see section 3.3.1).

K_d is a function of temperature, pressure, melt composition and oxygen fugacity, according to existing data (Ding et al., 2023). Once again, redox conditions are important for determining sulfur speciation in the melt, which can be described through the following equation (Ding et al., 2023):

$$\mathrm{S^{2-}_{melt}} + 2\,\mathrm{O_{2,gas}} \;=\; \mathrm{SO^{2-}_{4,melt}} \tag{5}$$

Because sulfur can exist as either S^{2-} or $SO_4{}^{2-}$ in the melt and as H_2S or SO_2 in the vapour, it is important to consider their differing behaviour during degassing. The approach taken in *Sulfur_X* involves two partition coefficients, corresponding to the two degassing reactions occurring:

$$\mathrm{FeS_{melt}} + \mathrm{H_2\,O_{vapour}} \;=\; \mathrm{H_2S_{vapour}} + \mathrm{FeO_{melt}} \tag{6}$$

$$\mathrm{CaSO_{4,melt}} \;=\; \mathrm{SO_{2,vapour}} + \mathrm{CaO_{melt}} + 0.5\,\mathrm{O_{2,vapour}} \tag{7}$$

Note that Ca^{2+} in Equation 7 can be replaced with K^+, Na^+ and other major cations, which are considered within the model (Ding et al., 2023).

The sulfide/sulfate ratio under given conditions can be calculated, and this ratio is applied to the two partition coefficients. This results in a combined partition coefficient, where the behaviours of both S^{2-} and SO_4^{2-} are incorporated and weighted based on their abundance in the melt. This results in a comprehensive method to model sulfur degassing which takes into account sulfur speciation, making it more flexible for use under varying redox conditions, as is the case in natural systems.

2.3.2 Diffusivity

Diffusivity of sulfur in silicate melts is also complicated by sulfur's multiple speciation. Unlike H_2O and CO_2, there is no method for measuring the concentrations of different sulfur species, meaning detailed diffusion data for sulfur is limited (Zhang et al., 2007). However, it is possible to measure S^{6+}/S_T and total sulfur concentration, allowing the concentration of individual sulfur species to be calculated (Fleet, 2005).

Studies have found that S^{2-} is the main diffusing species regardless of SO_4^2 content, and oxygen fugacity only affects sulfur diffusion at extremely high oxygen fugacities well above the transition from S^{2-} to S^{6+} (Baker & Rutherford, 1996; Freda et al., 2005). Therefore, in sulfur diffusion studies, 'sulfur diffusion' refers to the diffusion of S^{2-}, as this is the dominant diffusing sulfur species in natural systems. Several studies have been conducted for both silicic (e.g. Watson et al., 1993) and mafic (e.g. Freda et al., 2005) compositions, but for the purposes of this study, we focus on sulfur diffusivity in mafic melts. Figure 11 shows sulfur diffusivity under different conditions.

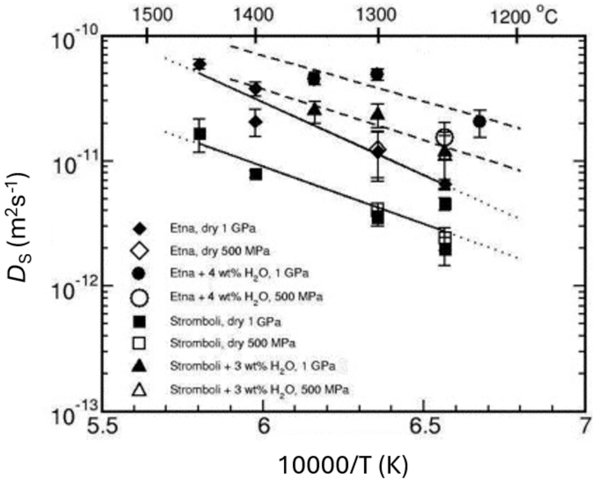

Figure 11: *From Freda et al., (2005). Sulfur diffusivity (D_S) in mafic compositions under different conditions.*

Sulfur diffusivity exhibits Arrhenian behaviour the same as CO_2 and H_2O, and is also very sensitive to H_2O concentration; sulfur diffusivity in hydrous melts is almost one magnitude higher than in dry melts (Freda et al., 2005). Pressure does not appear to have an effect on sulfur diffusivity in the range 0.5 - 1 GPa according to current studies, however data is limited in this area and further study is required to confirm this (Zhang et al., 2007). It has also been suggested that within basaltic melts, sulfur diffusivity is not sensitive to changes in composition (Freda et al., 2005).

Notably, sulfur diffusivity is sensitive to the oxygen fugacity, however further study on sulfur speciation and the effect of fO_2 on diffusivity is required to fully constrain this (Zhang et al., 2007).

Importantly, it has also been found that sulfur dissolves slower in basaltic melts than H_2O and CO_2, by up to two orders of magnitude. However, sulfur diffusion in basaltic melts is faster than in compositions with higher silica contents (Freda et al., 2005).

In general, there is very little research into sulfur diffusivity, and the limited number of models available in the literature restrict the conditions under which sulfur degassing can be modelled.

3 Methodology

In order to estimate whether disequilibrium degassing of sulfur in mafic magmas is occurring in natural systems, the open source bubble-growth model by Coumans et al., (2020) has been adapted from a single-volatile phase (H_2O) to include H_2O, CO_2 and S, with the model *Sulfur_X* implemented for calculating sulfur solubility. This allows us to computationally quantify exsolution and bubble growth in a multi-volatile system.

The bubble-growth model developed by Coumans et al., (2020) was chosen because it incorporates important physical processes associated with bubble growth in magmas, which can in turn affect the degassing of volatiles, such as time-dependent diffusion, surface tension and viscosity. This allows the model to exhibit disequilibrium conditions, and improve our understanding of how volatiles are exsolving from the melt on a very small scale.

3.1 Bubble-growth model

The original Coumans et al., (2020) model was developed for a H_2O-only system and is open-source and implemented in MATLAB. A full explanation of the model functionality and validation can be found in Coumans et al. (2020), but the main governing principles are as follows:

The model adopts the general mathematical framework of Blower et al. (2001), and extends it to include surface tension, as well as updated component models to account for material properties. This framework involves solving the hydrodynamics of the melt surrounding the bubble, the diffusion of H_2O through the melt, the equation of state of H_2O in the bubble, and the mass balance of H_2O between the melt and the bubble. The model outputs include the bubble radius through time, volatile melt concentrations through time, and bubble number density in a given space through time (i.e., the porosity).

3.1.1 Geometry

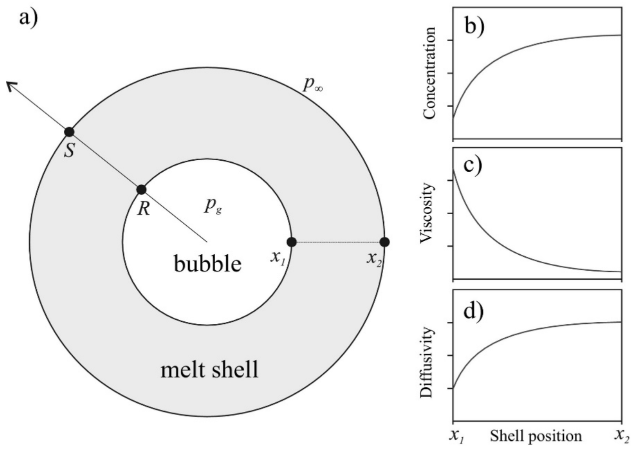

Figure 12: *a) The 'melt-shell' approach used in Coumans et al. (2020). A single, spherical bubble is surrounded by a spherical shell of melt. The line x1 → x2 is a radial transect across the melt shell. b–d) Schematic representation of spatial variation in concentration of dissolved* H_2O*, melt viscosity, and diffusivity of* H_2O*, across the radial transect x1 → x2 during bubble growth.*

The model works by generating a single spherical bubble and a shell of melt surrounding it (Figure 12), and computing the growth and resorption of the bubble in response to changes in pressure and temperature. The singular, spherical unit is representative of the entire bubbly magma, as it is assumed that the bubbles are uniform and identical.

The geometrical relationships of the bubble and melt shell are described by the following equations:

$$\begin{aligned} V_m &= \frac{1}{N_b} = \frac{V_g}{\phi} - V_g \\ V_g &= \frac{\phi V_m}{1-\phi} = \frac{4}{3}\pi R^3 \\ R &= \left(\frac{V_g}{\frac{4}{3}\pi}\right)^{1/3} \\ \phi &= \frac{V_g}{V_g + V_m} \end{aligned} \tag{8}$$

$$\begin{aligned} V_g + V_m &= \frac{4}{3}\pi S^3 \\ &= \frac{4}{3}\left(\frac{\pi R^3}{\phi}\right) \\ S &= R\phi^{-1/3} \\ &= L + R \end{aligned} \tag{9}$$

where V_m is the volume of melt in the shell, V_g is the volume of gas in the bubble, N_b is the bubble number density, ϕ is the gas volume fraction, R is the bubble radius, S is the melt shell radius, and L is the radial thickness of the melt shell.

3.1.2 Governing equations

To describe the hydrodynamics of bubble growth in a shell of liquid (ignoring inertial effects, due to the high viscosity and pressure conditions in bubbly magma), a modified form of the Rayleigh–Plesset equation is used:

$$p_g = p_\infty + \frac{2\Gamma}{R} + 4\eta\frac{dR}{dt}\left(\frac{1}{R} - \frac{R^2}{S^3}\right) \tag{10}$$

where p_g is the pressure of the gas in the bubble, p_∞ is the hydrostatic pressure acting on the outside of the liquid shell, $p_c = \frac{2\Gamma}{R}$ is the capillary pressure at the bubble wall, Γ is the gas-liquid interfacial tension, η is the viscosity of the liquid in the shell, and t is time.

In magmatic systems, melt viscosity is a function of dissolved H_2O content, and because the model involves diffusion of H_2O through the melt shell, it is important to account for the non-uniform H_2O content and therefore non-uniform viscosity within the melt. To address this, Blower et al. (2001) adapted Equation 10 to account for changes in the radial distribution of viscosity by integrating over the shell thickness in spherical coordinates. The Coumans et al. (2020) model adopts this approach, and also includes capillary pressure for very small bubbles:

$$p_g = p_\infty + \frac{2\Gamma}{R} + 12R^2\frac{dR}{dt}\int_{R_0}^{S_0} \frac{\eta(x)x^2}{(R^3 - R_0^3 + x^3)^2}\,dx \tag{11}$$

where R_0 and S_0 are the radius of the bubble and the melt shell at $t = 0$, and x is the radial Lagrangian coordinate. A Lagrangian coordinate system is used because the radial position x remains fixed as the bubble grows and shrinks. The Lagrangian radial coordinate x is related to the Eulerian coordinate A by conservation of volume:

$$A^3 - R^3 = x^3 - R_0^3 \tag{12}$$

To evaluate Equation 11, the spatial distribution of dissolved H_2O concentration in the melt shell, $C(x)$, is required in order to calculate the radial viscosity distribution $\eta(x)$. This is done at each timestep using the one-dimensional form of Fick's second law in spherical Lagrangian coordinates:

$$\frac{\partial C}{\partial t} = \frac{1}{x^2}\frac{\partial}{\partial x}\left(D\frac{A^4}{x^2}\frac{\partial C}{\partial x}\right) \tag{13}$$

where D is the diffusivity of H_2O in the melt, which can be generalised to different volatiles.

The H_2O concentration distribution is then used to calculate the mass of gas in the bubble m at the current timestep t, assuming conservation of H_2O mass within the bubble-shell unit:

$$m = m_0 + \frac{4\pi\rho_m}{100}\left(\int_{R_0}^{S_0} C(x,0)x^2\,dx - \int_{R_0}^{S_0} C(x,t)x^2\,dx\right) \tag{14}$$

where m_0 is the initial mass of gas in the bubble, ρ_m is the melt density, and C is in wt%.

Equations 8 through 14 can be solved numerically to compute R and ϕ at each timestep.

3.1.3 Material properties

To solve the governing equations, models are needed to describe physical properties of the system as functions of pressure, temperature (T), and H_2O content in the melt. These properties include:

- Solubility of H_2O in the melt phase $C_s(p_g, T)$
- Diffusivity of H_2O through the melt $D(C, p_\infty, T)$
- Equation of state for the gas phase $\rho_g(p_g, T)$
- Viscosity of the melt phase $\eta(C, T)$

3.1.4 Solubility

The solubility of H_2O determines the concentration boundary condition at the gas–melt interface, governing whether H_2O exsolves into the bubble or resorbs into the melt. For this study, the solubility model used is from Iacono-Marziano et al. (2012) for mixed H_2O–CO_2 in hydrous basalts, due to its widespread use (including within *Sulfur_X*) and established reliability:

$$\ln(\mathrm{H_2O_{eq}}) = 0.53\ln\left(10p_{b,\mathrm{H_2O}}\right) + 2.35\frac{\mathrm{NBO}}{\mathrm{O}} - 3.37 - \frac{0.021p}{T} \tag{15}$$

where $\mathrm{H_2O_{eq}}$ is the equilibrium water concentration in the melt (wt%), T is in K, p is the overall pressure of the system (same as p_∞) in MPa, p_{b,H_2O} is the partial pressure of H_2O in the bubble in MPa, and NBO/O is the ratio of non-bridging oxygen to total oxygen in the melt, defined on a hydrous basis as:

$$\begin{aligned} \text{NBO} &= 2 \times (X_{\text{H}_2\text{O}} + X_{\text{K}_2\text{O}} + X_{\text{Na}_2\text{O}} + X_{\text{CaO}} + X_{\text{MgO}} + X_{\text{FeO}} - X_{\text{Al}_2\text{O}_3}) \\ \text{NBO/O} &= \frac{\text{NBO}}{2X_{\text{SiO}_2} + 2X_{\text{TiO}_2} + 3X_{\text{Al}_2\text{O}_3} + X_{\text{MgO}} + X_{\text{FeO}} + X_{\text{CaO}} + X_{\text{Na}_2\text{O}} + X_{\text{K}_2\text{O}} + X_{\text{H}_2\text{O}}} \end{aligned} \tag{16}$$

where X_i is the mole fraction of oxide i in the melt.

Other solubility models in the open-source code include those by Ryan et al. (2015) and Liu et al. (2005).

3.2 Mixed volatile bubble-growth model

In this study, the bubble-growth model from Coumans et al., (2020) was adapted to include CO_2 and sulfur, as well as to improve flexibility for multi-volatile systems. For this adaptation the geometry and governing equations of the model remain the same, with the main alteration being the incorporation of partial pressures to account for the individual solubility of each volatile within a multi-volatile system, and new component models for material properties.

3.2.1 Solving a multi-volatile system

In order to include more than one volatile in the bubble-growth model, it is necessary to track the mass conservation of the three volatiles. In order to do this, the new bubble-growth model requires inputs of initial molar fraction of each volatile in the bubble, as well as their initial melt concentrations.

At the beginning of a model run, the initial pressure in the bubble is calculated using its initial radius and surface tension:

$$p_{b0} = p_{t0} + \frac{2\,\Gamma}{R_0} \tag{17}$$

where p_{t0} is the pressure at *t=0*, Γ is the surface tension, and R_0 is the initial radius of the bubble.

The initial total number of moles of gas in the bubble is then calculated using the ideal gas law, with absolute pressure as the pressure input:

$$n = \frac{pV}{RT} \tag{18}$$

Where p is pressure, V is the volume of the bubble, n is the total number of moles of gas in the bubble, R is the ideal gas constant, and T is the temperature at *t=0.* Note that the use of the ideal gas law is a simplifcation of the system, but since this study aims to quantify the overall behaviour of sulfur during degassing, this simplification can be justified for these purposes. Note that fugacity coefficients for H_2O, SO_2 and H_2S are calculated within the *Sulfur_X* portion of the model, and so more complex gas behaviour could be accounted for in future work.

The initial input molar fraction of each volatile in the gas phase is then multiplied by the total number of moles calculated from eq18, in order to calculate the number of moles of each volatile in the bubble, which can be converted to an initial mass of that volatile in the bubble using:

$$n_i = \frac{m_i}{Mr_i} \tag{19}$$

Where i refers to the volatile in question, n_i is the number of moles of the volatile, m_i is the mass of the volatile, and Mr_i is the molar mass of the volatile.

This calculated mass of each volatile defines their initial mass in the bubble at the beginning of the model run.

In order to quantify the amount of each volatile in the bubble at subsequent timesteps, this method is reversed, as the mole fraction of each volatile in the bubble is no longer predetermined. Once the model passes the first time step, the pressure and/or temperature change, defining new solubility conditions for each volatile. This means each volatile diffuses through the melt shell, changing the concentration gradient. By applying mass conservation, calculating the new melt concentration of the volatile allows the mass of each volatile in the bubble to be deduced using Equation 14. This can then be converted to the number of moles of each volatile in the bubble using Equation 19. This can subsequently be used to calculate a new mole fraction of each volatile in the bubble at each timestep, which is used to calculate the partial pressure.

The current solubility conditions for each volatile are then calculated. In the multi-volatile system, the individual solubility of each volatile is expressed using partial pressures. The sum of the partial pressures of each volatile equates to the absolute pressure of the system, such that the pressure in the bubble is equal to the pressure outside of it, ensuring its stability. The partial pressures of each volatile in the bubble are determined by the mole fraction of each volatile in the bubble, so that the following equation is always true:

$$p_{b,i} = X_i p \tag{20}$$

Where $P_{b,i}$ is the partial pressure of the volatile, X_i is the mole fraction of the volatile in the bubble, and p is the absolute pressure of the system.

The number of moles of each volatile in the bubble, along with the new bubble volume and current temperature are used to calculate the current partial pressure for each volatile in the bubble:

$$p_{b,\mathrm{i}} = \frac{n_\mathrm{i} R T}{V} \tag{21}$$

These partial pressures are then used as inputs into the component material property models for each volatile. Using partial pressures rather than the absolute pressure allows the specific conditions for each volatile to be represented, which is especially important for exhibiting the behaviour of volatile exsolution driving early exsolution of other volatiles. For example, if a bubble is composed of 99% CO_2 at depth, the partial pressure of H_2O will be very low, as its mole fraction in the bubble is very small. Since H_2O solubility is controlled by its partial pressure rather than the absolute pressure, a low partial pressure reduces the effective H_2O solubility and allows H_2O to exsolve at greater depths than would occur in a single-volatile system. This is representative of processes occurring in natural magmatic systems, and is an important feature to include in a multi-volatile model.

The new solubility conditions are then calculated using the current partial pressure of each volatile. The diffusivity of each volatile is then calculated using their constituent component models, with the system pressure as an input if necessary. This is because it is the pressure of the system which has a control on diffusion, not partial pressure across the bubble wall. The diffusivities of the volatiles and the calculations for melt viscosity are then used to calculate how much of each volatile exsolves at the current timestep. This allows the governing equations to be solved, and the concentration profile of each volatile through the melt shell to be calculated for each timestep.

Therefore, the multi-volatile system is solved by calculating the partial pressure of each volatile from the absolute pressure outside the bubble, determined by the mole fraction of that volatile in the bubble. This allows each volatile to exsolve under its own solubility conditions, and the bubble to grow and the proportion of each volatile in the gas phase to change as necessary. The model is therefore flexible, as the volatiles do not have to be CO_2 and S. To change the volatiles being modelled, all that is required are relevant component models, and adjusting the equations to use the molar mass of that volatile.

3.2.2 Component models

In order to include additional volatiles in the bubble-growth model, it is necessary to include relevant component models for their material properties. The material properties that are volatile-specific are solubility and diffusivity; the other component models do not require changing.

For the purposes of this study, the multi-volatile bubble-growth model needs to work for basaltic systems. As a result, the chosen component models are suitable for basaltic compositions, but the previous component models used in the original version (suitable for multiple different compositions) are still available to switch on/off. In addition, incorporating new empirical component models for different compositions is fairly straightforward.

Table 1 shows the chosen component models used in this study. The models in bold are those incorporated as part of this work, the others were pre-existing within the bubble-growth model.

	H_2O	CO_2	S
Solubility	**Iacono-Marziano et al., (2012), equation 13, hydrous**	**Iacono-Marziano et al., (2012), equation 12, hydrous**	***Sulfur_X* Kd_only (Ding et al., 2023)**
Diffusivity	Zhang & Ni (2010) equation 22	**Zhang et al. (2007) equation 32**	**Zhang et al. (2007) equation 31**
EOS (gas phase)	Ideal Gas Law		
Viscosity	Giordano et al., (2008)	-	-

Table 1: *Summary of component models used in the mixed-volatile bubble-growth model. Models in bold are those incorporated as part of this work, others are pre-existing in the single-volatile model.*

All of the component models incorporated as part of this work apart from *Sulfur_X* (see section 3.3) are empirical, and given below:

H_2O Solubility (Iacono-Marziano et al., 2012): See Equation 15.

CO_2 Solubility (Iacono-Marziano et al., 2012):

$$\begin{aligned}\ln(\mathrm{CO}_{2,\mathrm{eq}}) = &\left(-16.4X_{H_2O} + 4.4X_{\mathrm{Al}} - 17.1X_{\mathrm{FeO+MgO}} + 22.8X_{\mathrm{Na_2O+K_2O}}\right)\\ &+ \ln\left(10p_{b,\mathrm{CO_2}}\right) + 17.3\frac{NBO}{O} - 6 + \frac{1.2p}{T}\end{aligned} \tag{22}$$

Where CO_{2eq} is the equilibrium concentration of CO_2 in the melt (ppm), X indicates the mole fraction of an oxide in the melt, p is in MPa and T is in K.

H_2O Diffusivity (Zhang & Ni, 2010):

$$D_{H_2O} = H_2O_{wt\%}\exp\left(-8.56 - \frac{19110}{T}\right) \tag{23}$$

Where T is in K.

CO_2 Diffusivity (Zhang et al., 2007):

$$D_{\mathrm{CO_2}} = \exp\left(-13.99 - \frac{(17367 + 1944.8)p}{T} + H_2O_{wt\%}\frac{(855.2 + 271.2)p}{T}\right) \tag{24}$$

Where p is in MPa, and T in K.

S Diffusivity (Zhang et al., 2007):

$$D_S = \exp\left(-8.21 - \frac{(27692 - 651.6)H_2O_{wt\%}}{T}\right) \tag{25}$$

Where T is in K.

3.3 Implementation of *Sulfur_X*

In order to incorporate sulfur into the bubble-growth model, a component model for sulfur solubility was required. Unlike H_2O and CO_2, sulfur solubility is complex and cannot be expressed as a simple empirical equation, due to multiple sulfur species dissolving depending on the oxygen fugacity (fO_2), and the precipitation of additional sulfur phases upon saturation. In order to take into account the solubility of both dissolving sulfur species, sulfur degassing can be modelled using the partioning of sulfur into the gas phase, using a partition coefficient ($K_{d,S}^{v/m}$, see section 2.3.1). Ding et al., (2023) present an equilibrium degassing model for an H_2O-CO_2-S system, which calculates $K_{d,S}^{v/m}$ to describe sulfur solubility. They include a simplified 'Kd_only' version of their model to calculate this sulfur partition coefficient from a set of inputs, which is open source and implemented in Python. For the purposes of this work, when using the term *Sulfur_X* , this refers to the simplified 'Kd_only' model, unless specified otherwise.

While other models for calculating $K_{d,S}^{v/m}$ exist, many of these are tailored to specific volcanoes, do not account for changing fO_2 and sulfur speciation, or assume a perfectly closed system. The ability of *Sulfur_X* to account for several of these allows it to be implemented into our model and used for several situations, without compromising on accuracy (further validation of *Sulfur_X* can be found in Ding et al., 2023). Additionally, other model approaches for calculating sulfur solubility such as sulfide/sulfate capacity also exist (e.g. Moretti & Papale 2004), but in the context of our bubble-growth model and its setup, the use of a partition coefficient is more sensible.

In order to incorporate this model into the bubble-growth model as the component model for sulfur solubility, it was rewritten in MATLAB and executed as a function that is called at each timestep, just like the empirical component models.

3.3.1 How *Sulfur_X* works

The inputs for *Sulfur_X* are the current temperature, pressure, composition, fO_2 relative to FMQ, mole fractions of H_2O and S in the bubble, H_2O concentration in the melt, and the molar mass of the melt. All of these are calculated in the bubble-growth model at each timestep except for fO_2, which was added as an additional input at the beginning of the bubble-growth model, in the form of fO_2 relative to the FMQ buffer in log units.

To account for sulfur speciation, *Sulfur_X* calculates two partition coefficients, $K_{d,1}$, and $K_{d,2}$, relating to the two main reactions involved for sulfide (S^{2-}) and sulfate (SO_4^{2-}) exsolving a gas phase (Equations 6 and 7).

A combined partition coefficient is calculated by weighting the two partition coefficients with the sulfate ratio:

$$K_{d,\text{combined}} = K_{d,1} R_s + K_{d,2}(1 - R_s) \tag{26}$$

Where R_s is the sulfate ratio (S^{6+}/S_T). This combined partition coefficient ensures the system is sensitive to changes in fO_2 and sulfur speciation, allowing it to be applicable to multiple volcanic systems.

In order to calculate $K_{d,combined}$, the model must calculate the absolute fO_2, fugacity coefficients of H_2O, H_2S, and SO_2, fH_2O, $K_{d,1}$, $K_{d,2}$, and the sulfate ratio. This is explained in further detail in section 3.3.2.

3.3.2 MATLAB implementation

In order to be able to calculate $K_{d,combined}$ at each timestep within the bubble-growth model, *Sulfur_X* was rewritten in MATLAB and restructured to use functions instead of classes for a smoother implementation with the rest of the bubble-growth model.

This new version of *Sulfur_X* is structured as a function file, containing nested functions for each calculation within the model. Importantly, there are calculations at the beginning of the model normalising the composition and calculating oxide mole fractions. There are several versions of these calculations, as in the original *Sulfur_X* different calculations within the model require different composition components, for example when calculating oxygen fugacity, the composition does not include H_2O. In order to keep the new implementation of *Sulfur_X* identical to the original, all of these compositional differences are accounted for in each function.

The first calculation within *Sulfur_X* after normalising the composition is the calculation for oxygen fugacity:

$$\log_{10}\left(fO_{2,\text{FMQ}}\right) = \frac{-25096.3}{T} + 8.735 + \frac{0.110(p_b - 1)}{T} \tag{27}$$

Where $fO_{2,FMQ}$ is the absolute oxygen fugacity at the FMQ buffer, T is the current temperature in K, and p_b is the current pressure in bar. The input of fO_2 relative to FMQ in log units is then added to this value, in order to calculate $\log(fO_2)$ at the current timestep.

The next calculation is that for the iron ratio (Fe^{3+}/Fe_T), which is used later on to calculate sulfur speciation:

$$\text{R}_\text{f} = \frac{2\exp(0.196\ln fO_2 + \text{con})}{1 + 2\exp(0.196\ln fO_2 + \text{con})} \tag{28}$$

Where fO_2 is the absolute oxygen fugacity, and *con* is calculated from the pressure, temperature and composition (see Appendix A).

The model then calculates the fugacity coefficients for the three system components: H_2S, SO_2 and H_2O. For H_2S and SO_2 this is done using the model of Shi & Saxena (1992) (equations 3a, 9 and 10), and for H_2O using Zhang & Duan (2009). The full equations and parameters can be found in the appendices (see Appendix A.1), but simplified versions for each calculation are as follows:

SO_2:

$$\Phi_{\mathrm{SO_2}} = \exp\left[A\ln\left(\frac{p_r}{0.012703}\right) + B(p_r - 0.012703) + \frac{C}{2}(p_r^2 - 0.012703^2) - \ln p\right] \tag{29}$$

H_2S:

$$\Phi_{\mathrm{H_2S}} = \exp\left[A\ln\left(\frac{p_r}{0.011103}\right) + B(p_r - 0.011103) + \frac{C}{2}\left(p_r^2 - 0.011103^2\right) - \ln p\right] \tag{30}$$

Where Φ_{SO_2} and Φ_{H_2S} are the fugacity coefficients for SO_2 and H_2S, respectively, A, B and C are constants (see Appendix A.1), p is the system pressure in bar and p_r is the system pressure divided by the critical pressure of SO_2 or H_2S in bar.

H_2O:

$$\Phi_{\mathrm{H_2O}} = \exp(Z - 1 - \ln Z + S_1) \tag{31}$$

where

$$Z = \frac{p_m V_m}{RT_m}$$

and

$$p_m = \frac{3.0636(2.88)^3 p}{510}, \quad T_m = \frac{154\,T}{510}, \quad R = 0.08314467\ \mathrm{cm^3 bar/K\ mol}$$

where Φ_{H_2O} is the fugacity coefficient of H_2O, p_m and p are in bar, and T_m and T are in K.

The molar volume V_m is iteratively solved from the equation of state formula for H_2O from Zhang & Duan (2009):

$$\begin{aligned} p = \Bigg(1 &+ \frac{a_1 + \frac{a_2}{T_m^2} + \frac{a_3}{T_m^3}}{V_m} + \frac{a_4 + \frac{a_5}{T_m^2} + \frac{a_6}{T_m^3}}{V_m^2} \\ &+ \frac{a_7 + \frac{a_8}{T_m^2} + \frac{a_9}{T_m^3}}{V_m^4} + \frac{a_{10} + \frac{a_{11}}{T_m^2} + \frac{a_{12}}{T_m^3}}{V_m^5} \\ &+ \frac{a_{13}}{T_m^3 V_m^2}\left(a_{14} + \frac{a_{15}}{V_m^2}\right) e^{-a_{15}/V_m^2}\Bigg) \frac{RT_m}{V_m} \end{aligned} \tag{32}$$

where p is in bar, T_m is in K, and the coefficients a_i depend on temperature and are given constants (see Appendix A.1).

Finally, the term S_1 from equation 31 is defined as:

$$
\begin{aligned}
S_1 = {} & \frac{a_1 + \frac{a_2}{T_m^2} + \frac{a_3}{T_m^3}}{V_m} \\
& + \frac{a_4 + \frac{a_5}{T_m^2} + \frac{a_6}{T_m^3}}{2V_m^2} \\
& + \frac{a_7 + \frac{a_8}{T_m^2} + \frac{a_9}{T_m^3}}{4V_m^4} \\
& + \frac{a_{10} + \frac{a_{11}}{T_m^2} + \frac{a_{12}}{T_m^3}}{5V_m^5} \\
& + \frac{a_{13}}{2a_{15}T_m^3}\left(a_{14} + 1 - \left(a_{14} + 1 + \frac{a_{15}}{V_m^2}\right)e^{-a_{15}/V_m^2}\right)
\end{aligned}
\tag{33}
$$

The H_2O fugacity fH_2O is then calculated using the following:

$$
f_{H_2O} = X_{H_2O} p \Phi_{H_2O} \tag{34}
$$

Where X_{H_2O} is the mole fraction of water in the bubble and p is in bar.

The current pressure, temperature, composition, fugacity coefficients, fO_2, fH_2O and X_{H_2O} are then all used to calculate the partition coefficients.

The simplified expressions for kd_1 (partitioning of S^{2-}) and kd_2 (partitioning of SO_4^{2-}) are written below:

$$
k_{d1} = X_{H_2O} \exp\left(\mathrm{residual}_{\mathrm{rxn1}}\right) \tag{35}
$$

$$
k_{d2} = \exp\left(\mathrm{residual}_{\mathrm{rxn2}}\right) f_{O_2}^{-0.5} \tag{36}
$$

Where $\mathrm{residual}_{\mathrm{rxn1}}$ and $\mathrm{residual}_{\mathrm{rxn2}}$ are calculated from the temperature, pressure, composition and fugacity coefficients (see Appendix A.2 for the full calculations).

In order to calculate a combined partition coefficient for sulfur from kd_1 and kd_2, they are weighted by the sulfate ratio. *Sulfur_X* has three built-in models for sulfur speciation: Nash et al., (2019), O'Neill & Mavrogenes (2022) and Muth & Wallace (2021). Ding et al., (2023) reports the error of *Sulfur_X* to be larger than the difference between the three models, making the choice obsolete. Therefore, throughout this study we use the sulfur speciation of Nash et al., (2019) for consistency:

$$
R_s = \frac{10^{8\log_{10}\left(\frac{R_f}{1-R_f}\right) + \frac{8.7436\times10^6}{T_0^2} - \frac{27703}{T_0} + 20.273}}{1 + 10^{8\log_{10}\left(\frac{R_f}{1-R_f}\right) + \frac{8.7436\times10^6}{T_0^2} - \frac{27703}{T_0} + 20.273}} \tag{37}
$$

Where R_s is the sulfate ratio, R_f is the iron ratio (see Equation 28) and T_0 is the temperature in K.

$K_{d,combined}$ is then calculated using Equation 26.

All of these calculations were copied over from the original Python script into the new MATLAB function. However, in order to incorporate this as a solubility calculation for sulfur within the bubble-growth model, it requires an equilibrium sulfur melt concentration. This was done using the definition of $K_{d,combined}$ from Ding et al., (2023):

$$K_{d,\text{combined}} = \frac{X_{S,\text{vapour}}}{X_{S,\text{melt}}} \tag{38}$$

Where $X_{S,vapour}$ is the molar fraction of sulfur in the vapour, and $X_{S,melt}$ is the molar fraction of sulfur in the melt. Note that with the implementation of *Sulfur_X* in the bubble-growth model, only elemental sulfur is considered, not explicitly H_2S or SO_2. Therefore when including sulfur in the bubble-growth model, the molar mass of sulfur is used throughout, rather than the molar masses of H_2S and SO_2. This is because of the use of a combined partition coefficient, and the aim of investigating sulfur behaviour as a whole, rather than individual volatiles. However, it is important to note that this simplification means the effects of pressure-dependent degassing are not represented in this model, and neither are associated changes in fO_2, which is set to constant. This means that this model cannot be used to make inferences on changes in H_2S/SO_2, and while pressure-dependent trends are visible, it is important to remember that these are the combined behaviour of two volatile species.

Rearranging Equation 38 gives:

$$X_{S,\text{melt}} = \frac{X_{S,\text{vapour}}}{K_{d,\text{combined}}} \tag{39}$$

The bubble-growth model calculates the molar fraction of sulfur in the bubble at each timestep, meaning we can calculate $X_{S,melt}$ once we have $K_{d,combined}$. $X_{S,melt}$ can be converted into concentration (ppm) using the molar mass of the melt, which can be calculated from the composition and the current melt concentration of CO_2 and H_2O:

$$\text{S}_{\text{ppm}} = \frac{10^6\, X_{S,\text{melt}} M_r^{\text{S}}}{M_r^{\text{melt}}(1 - X_{S,\text{melt}})} \tag{40}$$

Where M_r^S is the molar mass of sulfur, and M_r^{melt} is the molar mass of the melt. These calculations, along with the implementation of *Sulfur_X* allow an equilibrium melt sulfur concentration to be calculated at each timestep within the bubble-growth model.

3.3.3 Limitations of *Sulfur_X*

It is important to be aware of the limitations of *Sulfur_X* which will be carried over into the bubble-growth model. Arguably the most notable limitation is its inability to account for the formation of an additional sulfur phase. This is because when sulfide or sulfate become saturated, they can exsolve to form additional phases, such as an immiscible liquid (sulfide), or anhydrite (sulfate). To combat this, using the empirical model from Fortin et al. (2015), we determine that for the scope of this study (primitive Fagradalsfjall basalts with a maximum sulfur content of 1171 ppm), it can be assumed that no additional sulfur phase forms, as the conditions consistently lie below the sulfur content at sulfide saturation (SCSS), which is calculated as 1659 ppm at saturation (1200°C, 672 MPa). To ensure this and improve the flexibility of the model for other volcanic systems, a warning has been built into the bubble-growth model that will flag if the sulfur concentration at any point in the melt 'shell' goes above the current value for the SCSS, based on the model of Fortin et al., (2015).

Additionally, we assume the change in fO_2 relative to FMQ throughout degassing to be negligible, due to sulfur degassing occurring at very shallow depths and over short timescales. Our implemented version of *Sulfur_X* therefore calculates exact fO_2 at every timestep, but it is always set as the same value relative to FMQ. While this is a simplification as it is known that fO_2 changes significantly throughout degassing, the aim of this study is to understand the effects of sulfur diffusion on degassing, rather than the complex changes in sulfur speciation and altering redox conditions during magma ascent. By keeping fO_2 the same relative to FMQ, some change in oxygen fugacity during magma ascent is accounted for, without adding an additional complexity that could obscure the effects of diffusion this study aims to quantify. While adding changing fO_2 is a possibility for future work (and very feasible due to many of the calculations already existing within the *Sulfur_X* portion of the model), for the purposes of this study, a constant fO_2 relative to FMQ can be considered suitable.

3.4 Mixed H_2O-CO_2-S solubility

The implementation of multiple volatiles in the bubble-growth model resulted in the need for several new inputs (component models for each volatile, initial mole fractions in the bubble, fO_2 and initial volatile melt concentrations), most of which can be found in the literature for a specific magmatic system (e.g. fO_2), but this is not the case for the molar fractions of each volatile in the vapour phase (X_{H_2O}, X_{CO_2}, X_S) at the start of the model run. In order to model the effects of decompression on volatile degassing, it is important the bubble-growth model begins under equilibrium conditions, to simulate a magmatic system at depth. The original bubble-growth model from Coumans et al., (2020) calculates the H_2O saturation at a given pressure, so a similar function was implemented into the multi-volatile model to calculate initial values of X_{H_2O}, X_{CO_2}, and X_S which correspond to equilibrium conditions.

This was done using the initial melt H_2O, CO_2 and S concentrations and the three solubility models to calculate their saturation pressure and corresponding partial pressures in the bubble (and as a result, their molar fractions in the vapour phase).

The function uses MATLAB's `lsqnonlin` nonlinear least-squares solver to solve for the partial pressures of each volatile (p_{bH_2O}, p_{bCO_2}, and p_{bS}) using their melt concentrations and the three solubility models. For H_2O and CO_2, this is done by using the initial guesses for partial pressure and total pressure (defined as the sum of the partial pressures of each volatile) to calculate the equilibrium melt concentrations, and refining the guesses until the equilibrium melt concentrations match the original input values. For sulfur, the solver uses *Sulfur_X* to calculate the mole fraction of sulfur in the bubble (X_S) from $K_{d,combined}$ and the mole fraction of sulfur in the melt (XS_{melt}), which is in turn calculated from the initial input for sulfur melt concentration. X_S is then multiplied by total pressure to calculate P_{bS}, which is compared to the current guess by the solver. The system is then iteratively solved to find values for P_{bH_2O}, P_{bCO_2}, and P_{bS} which correspond with the input melt concentrations. X_{H_2O}, X_{CO_2}, and X_S are then calculated from the partial pressures, and outputted by the function along with total pressure, which can be used as the initial pressure for the model run to ensure the system starts at saturation.

This function therefore allows the calculation of mixed H_2O-CO_2-S solubility and saturation pressure, and the proportion of each volatile in the vapour phase.

3.5 Summary

A comprehensive numerical model capturing physical behaviours of H_2O-CO_2-S degassing has been developed for basaltic systems. The model tracks volatile diffusion and partitioning into a vapour phase along variable P-T-t paths, allowing the quantification of disequilibrium degassing in a multi-volatile system. Sulfur solubility has been accounted for by implementing the methods of *Sulfur_X*, allowing mixed H_2O-CO_2-S solubility to be modelled and saturation pressures and vapour mole fractions to be calculated. The model is flexible, and can run with one, two or all three volatiles, and can be easily adapted for different volcanic systems. The full model script is available as a supplementary folder, see Appendix C for full instructions.

4 Model testing

4.1 Independence to numerical scheme

With all numerical models, it is important to determine that the results are independent of the numerical scheme used to solve the system of equations. With the bubble-growth model, this was tested by varying the number of nodes (i.e., the number of points within the melt shell where volatile concentration is calculated), and the numerical tolerance (maximum error the model is allowed during approximations), under the conditions of Fagradalsfjall 2021 (see Table 5). These conditions were chosen as they are used throughout this study, and are the conditions under which the model is thought to be most accurate (i.e., a basalt with low enough sulfur content to prevent the formation of an additional sulfur phase). The number of nodes and numerical tolerance were varied from zero to the maximum value at which the model could run without struggling and slowing down (i.e., the whole range of feasible values that the user can set). The default values for these parameters used throughout this study, including the sensitivity analysis, are 100 nodes and a numerical tolerance of 1×10^{-5}. The results for this sensitivity analysis are shown in Figure 13.

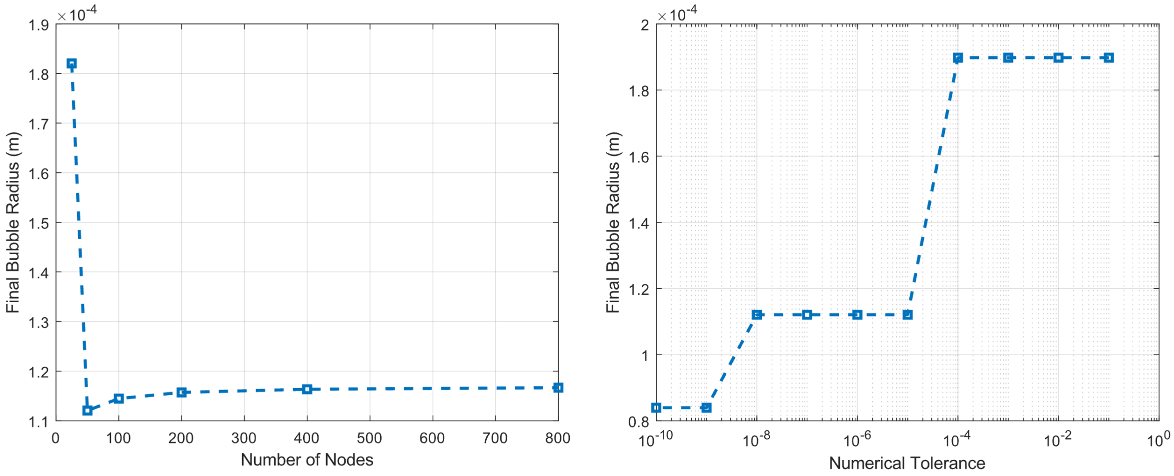

Figure 13: *Results from the sensitivity analysis of the numerical scheme of the model. The plot on the left shows the impact of changing the number of nodes on the final bubble radius, and the right plot shows the effect of changing the numerical tolerance. The sensitivity analysis was done under the conditions of Fagradalsfjall 2021 (see Table 5).*

The results show that by changing the number of nodes by a factor of 30, there is very little change in the final bubble radius. Therefore, it appears that above a critical value (around 50 nodes, based on the sensitivity analysis), the number of nodes stops having an impact on the final bubble radius. This suggests that the results of the model are largely independent of the number of nodes, so long as they are set to above 50. Therefore for all model runs used in this study, the number of nodes is never set below 50.

Changing the numerical tolerance of the model by 10 orders of magnitude changes the final bubble radius by 200%. This is because the numerical tolerance defines the maximum error allowed during the model's approximations, since it cannot be solved exactly. The value of the numerical tolerance therefore can affect the model outputs by altering its time-stepping behaviour. The numerical solver works by using adaptive time stepping, which involves taking a step forward in time, and then seeing how reasonable it was to take a step of that size. If the step size produced a result within the error tolerance, the solver will continue to take steps of that size. If not it will take smaller ones, until the results are considered reasonable. The pattern in Figure 13 relates to several numerical tolerances working for a similar stable step size, meaning tightening the tolerance does not have an effect on the model output. This is the case until a stricter tolerance threshold is reached at which the step size must be made smaller, resulting in an abrupt change in model outputs. This behaviour produces the observed step-wise pattern in model sensitivity to numerical tolerance.

Figure 13 shows the model is more sensitive to the numerical tolerance than the number of nodes. It can be seen that increasing the numerical tolerance can have a large impact on model outputs, especially over numerical tolerances of 1×10^{-5}. However, reducing the numerical tolerance to very small values ($<1 \times 10^{-7}$) causes the model to slow down significantly, reducing its usability. Therefore, a balance must be struck between maintaining the accuracy of model outputs, and keeping the model running smoothly enough to justify its use. Figure 13 suggests that most of the change in model outputs occurs at numerical tolerances $>1 \times 10^{-5}$, and so all of the model runs in this study use this value for the numerical tolerance. However, having to strike such a balance is not ideal, and this can be considered a limitation of the bubble-growth model that could be addressed in future work.

4.2 Component model benchmarking

During model testing, it is also important to ensure the implementation of different component models is correct, and so they must be benchmarked against the originals. In the case of the bubble-growth model, the most important component models are those for solubility, which are *Sulfur_X* Ding (2023) for sulfur and Iacono-Marziano et al. (2012) for H_2O and CO_2.

4.2.1 H_2O-CO_2 solubility

In order to compare the outputs of the bubble-growth model's implementation of the solubility model to those of the original, the web application version of the Iacono-Marziano model was used, which is linked to in their original paper (Iacono-Marziano et al., 2012). Importantly, this web application uses slightly different constants within the H_2O model to the ones listed in their paper, and so for the purposes of benchmarking, these parameters were adjusted in the bubble-growth model. The modified version of the H_2O solubility model is as follows:

$$\ln[\mathrm{H_2O}]^{\mathrm{wt\%}} = 0.521 \ln[10 p_{\mathrm{H_2O}}] + 2.116 \left[\frac{\mathrm{NBO}}{\mathrm{O}}\right] - 3.244 - 0.022 \frac{10p}{T} \tag{41}$$

Where p and p_{H_2O} are in MPa, and T is in K.

The composition was also adjusted, with MnO, P_2O_5 and F_2O being set to 0, as these are not inputs in the web application version of the model. For the benchmark test, the conditions of Fuego were used, as these are the conditions used in the original validation of *Sulfur_X*. These conditions are listed in Table 2.

Parameter	**Value**	**Source**
Composition	*see Appendix B*	Ding et al., (2023)
Melt density	2750 kg m^{-3}	Rose et al., (1978)
Bubble number density	1×10^{12} m^3	Rose et al., (2008)
Temperature	1100° C	-
Oxygen fugacity	$\Delta FMQ + 1.2$	Ding et al., (2023)
Initial H_2O concentration	4.5 wt%	Ding et al., (2023)
Initial CO_2 concentration	3300 ppm	Ding et al., (2023)

Table 2: *Input conditions used in the benchmark test for the constituent H_2O-CO_2* solubility models.

Importantly, the temperature was adjusted from the original value of 1030°C because the minimum temperature available in the web application is 1100°C. For the purpose of this test, sulfur concentration was set to 0.

The bubble-growth model's function for calculating saturation pressure was adjusted, allowing it to run through different combinations of H_2O and CO_2 concentrations. These were then plotted with saturation pressure on a 3D heat map, and isobars added (Figure 14). The isobar values were then input into the web application model, and the molar fraction of H_2O in the fluid varied, in order to determine different pairs of H_2O-CO_2 concentrations at that saturation pressure. This data was then plotted on top of the original heat map (Figure 14).

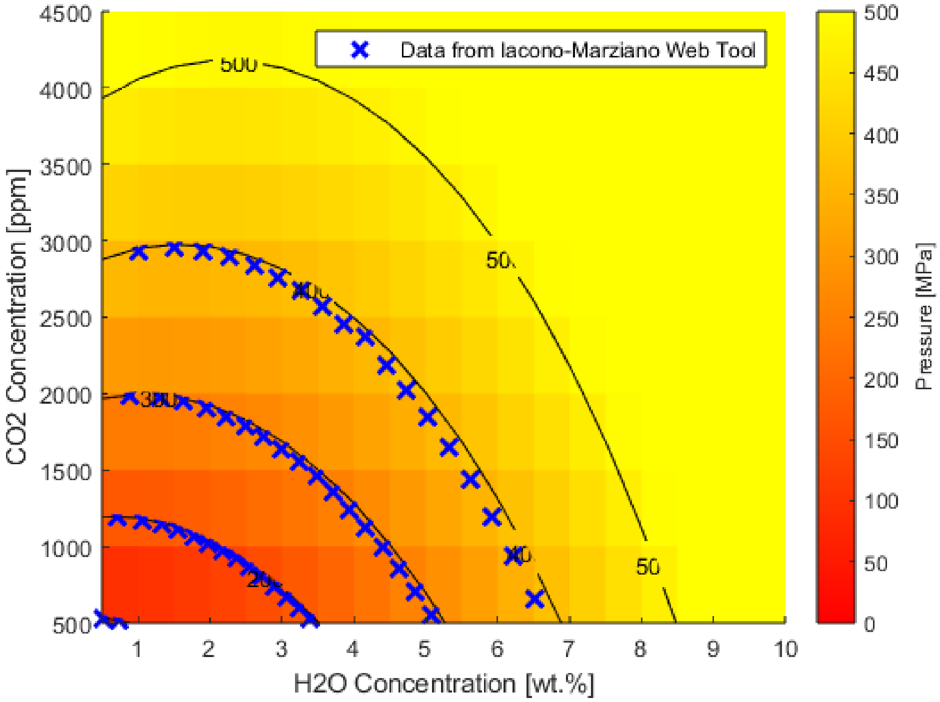

Figure 14: *Heatmap of outputs from the bubble-growth model's implementation of Iacono-Marziano et al. (2012). Outputs from the web application version of their model are plotted on top. A good agreement suggests successful implementation.*

It can be seen that there is a good match between the outputs from the bubble-growth model's implementation and those of the web application version. It can therefore be assumed that the mixed H_2O-CO_2 solubility model of Iacono-Marziano et al. (2012) has been successfully implemented into the bubble-growth model.

4.2.2 Sulfur solubility

To test our implementation of *Sulfur_X* against the original, the bubble-growth model's version was adjusted to run individually with specified input conditions, again simulating the conditions of Fuego volcano. These specific inputs are listed in Table 3.

Parameter	**Value**	**Source**
Composition	*see Appendix B*	Ding et al., (2023)
Temperature	1030°C	Ding et al., (2023)
Oxygen fugacity	$\Delta FMQ + 1.2$	Ding et al., (2023)
Initial H_2O concentration	4.5 wt%	Ding et al., (2023)
Initial H_2O fluid mole fraction	0.9	-

Table 3: *Input conditions used in both the MATLAB implementation of* Sulfur_X *and the original in the benchmark test.*

The MATLAB implementation of *Sulfur_X* was then run with varying pressures from 100 MPa to 10 MPa at intervals of 10 MPa, and the output partition coefficients recorded. The same was done using the original *Sulfur_X* 'Kd only' script in python. Importantly, output partition coefficients were recorded for all three sulfur speciation models available within *Sulfur_X* (Nash et al., 2019, Muth & Wallace 2021, and O'Neill and Mavrogenes 2022), to ensure these all work correctly and therefore the choice of speciation model has negligible impact on model results. The output partition coefficients from the bubble-growth model's implementation and the original *Sulfur_X* script are plotted in Figure 15, for each sulfur speciation model.

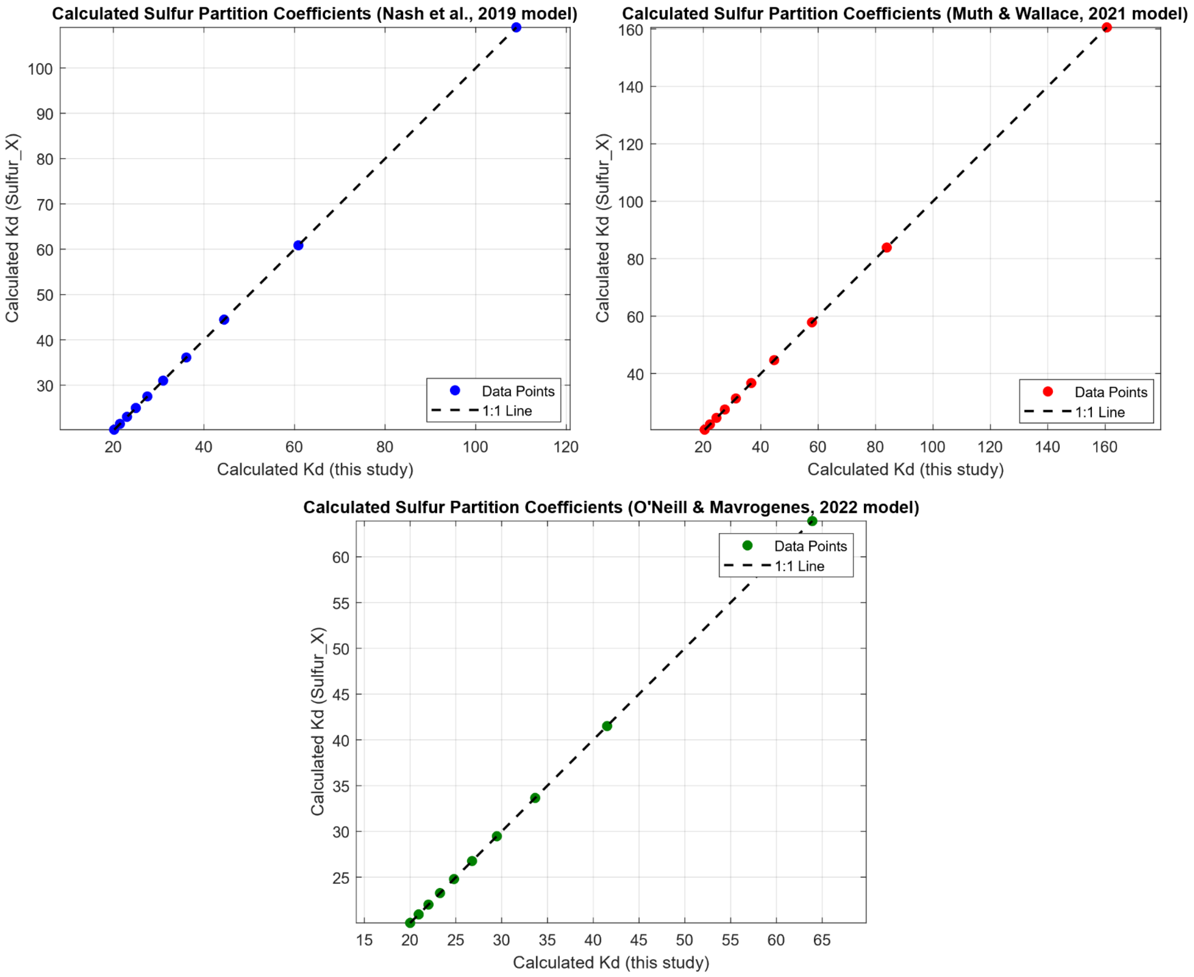

Figure 15: *Outputs from the Sulfur_X 'Kd only' model (Ding et al., 2023) vs. outputs from the version implemented in the bubble-growth model, for each of the sulfur speciation models available. The outputs are an exact match, indicating successful implementation.*

Figure 15 shows that the outputs from the MATLAB implementation of *Sulfur_X* match perfectly those produced by the original script. This suggests that this component model has been successfully implemented in the bubble-growth model.

5 Results

As well as recreating a specific eruption scenario, the model was used to investigate disequilibrium behaviour of sulfur during degassing, and the effects of other volatiles in the system. The model outputs are useful for gaining insight into the behaviour of sulfur and the complex interactions occurring within volcanic systems.

5.1 Interpreting model outputs

In order to interpret the results, it is important to understand the model outputs and the different behaviours they exhibit. Figure 16 shows an example model output for H_2O under equilibrium (dP/dt ~ 10^{-10} MPa/s) conditions for Fagradalsfjall 2021, from ~670 to 0.5 MPa (see Table 5 for a full list of conditions).

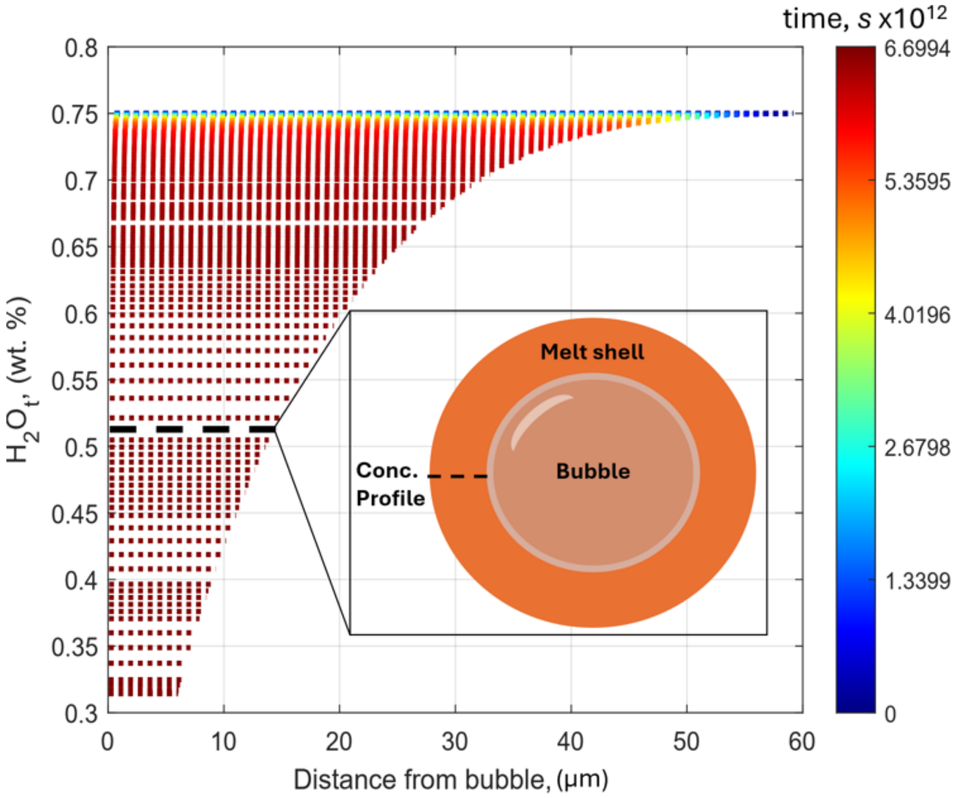

Figure 16: *Example model output for equilibrium H_2O concentration profiles through time. Schematic diagram illustrates the location of the concentration profile within the melt shell.*

The graph shows the concentration profile of H_2O through the melt shell (with 0 on the x axis representing the bubble wall), at each time step, with time shown in colour. Each line represents a H_2O concentration profile at a different moment in time, as illustrated in the schematic. It can be seen that at later time steps, the water concentration is lower, and the profiles shorter. Most of these profiles are also coloured in red, illustrating how the water concentration only began to significantly drop towards the end of the model run. The shortening of the concentration profiles with time relates to the thinning of the melt shell surrounding the bubble as the bubble grows, resulting in smaller distances from the bubble through time. This is illustrated in Figure 17, which shows how the porosity increases with the time, and the melt shell thickness reduces.

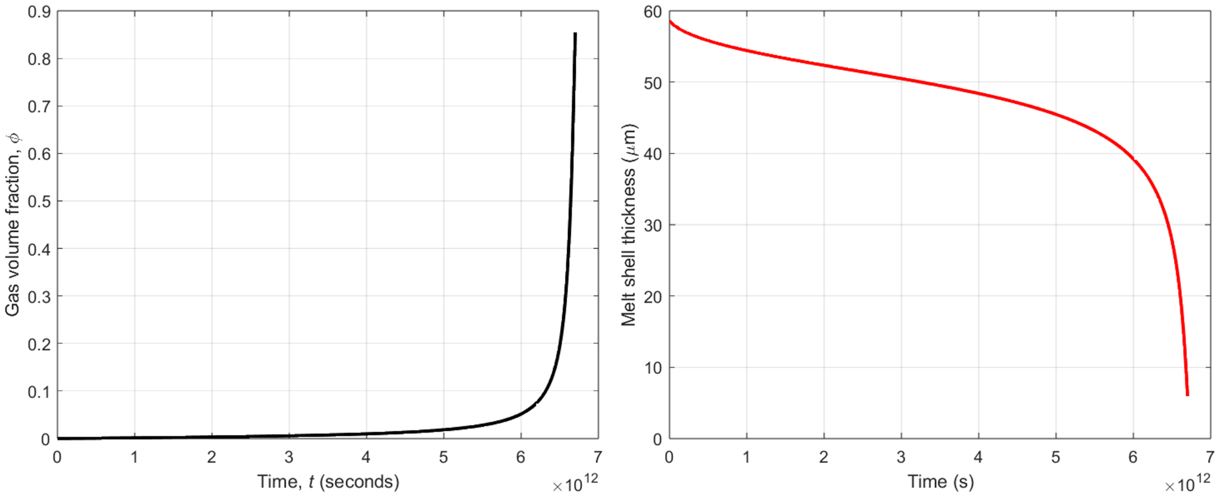

Figure 17: *Model output showing porosity and melt shell thickness with time, for the run shown in Figure 16. The porosity increases with time, and the melt shell thickness consequently decreases as the bubble grows.*

These outputs exhibit equilibrium conditions, as it can be seen in Figure 16 that each profile is a straight line: i.e., the concentration of H_2O through the melt at that point in time is uniform. The figure shows that the concentration of H_2O within the melt remained uniform throughout the entire run, suggesting there was sufficient time for H_2O diffusion through the melt shell in order for it to enter the bubble and adjust to the solubility conditions, equilibrating the system.

Figure 18 shows an example model output for CO_2 under disequilibrium conditions, using a decompression rate of ~10 MPa/s.

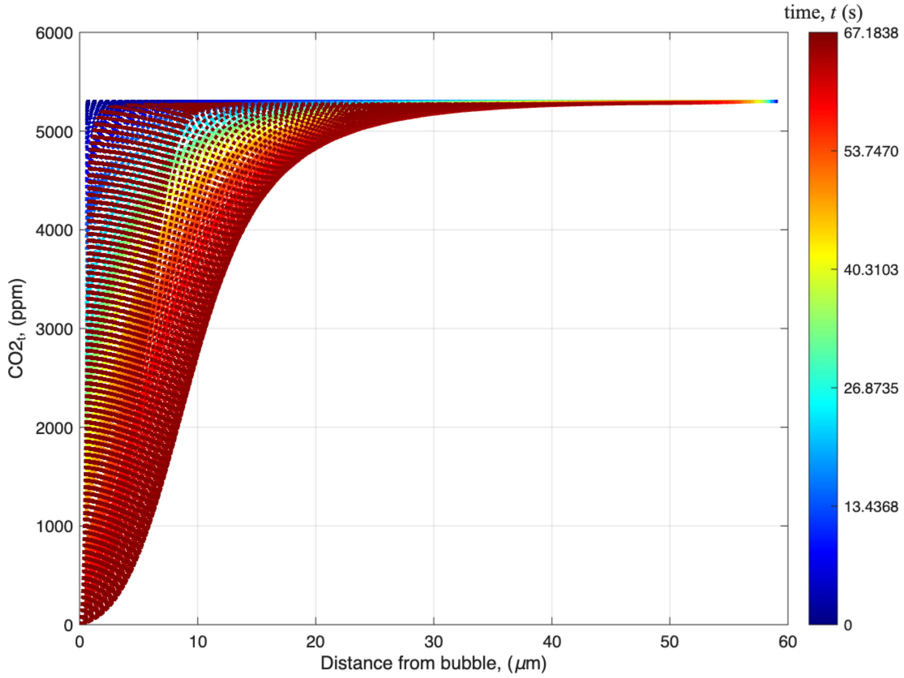

Figure 18: *Example model output for disequilibrium CO_2 concentration profiles through time.*

The system can be seen to be in disequilibrium, as the concentration profiles are not uniform. The CO_2 concentration increases with distance from the bubble in each profile, and this becomes more dramatic through time. This is because there is not enough time for the CO_2 to diffuse through the melt shell to enter the bubble, and so only the CO_2 closest to the bubble wall can exsolve. This results in non-uniform profiles through the melt. However, this trend is difficult to see in Figure 18, due to the appearance of the profiles to 'fold over' each other. this is an artefact from not normalising the distance from the bubble. Under extreme disequilibrium conditions, the later concentration profiles can show extreme differences between the CO_2 concentration at the bubble wall and the concentration at the edge of the melt shell. These profiles are also very short as at the end of a model run the melt shell is very thin due to the growth of the bubble. This results in a very steep curve in the output graph, as the entire range of CO_2 concentrations is found within a very short distance from the bubble. These steep curves appear to 'overlap' previous concentration profiles, resulting in the 'folding' visible in Figure 18. To remove this artefact, the distance along the melt shell can be normalised, allowing each concentration profile to be compared directly with each other, ignoring the effect of the thinning melt shell.

This is shown in Figure 19, which shows the same data as Figure 18, but with the distance from the bubble normalised.

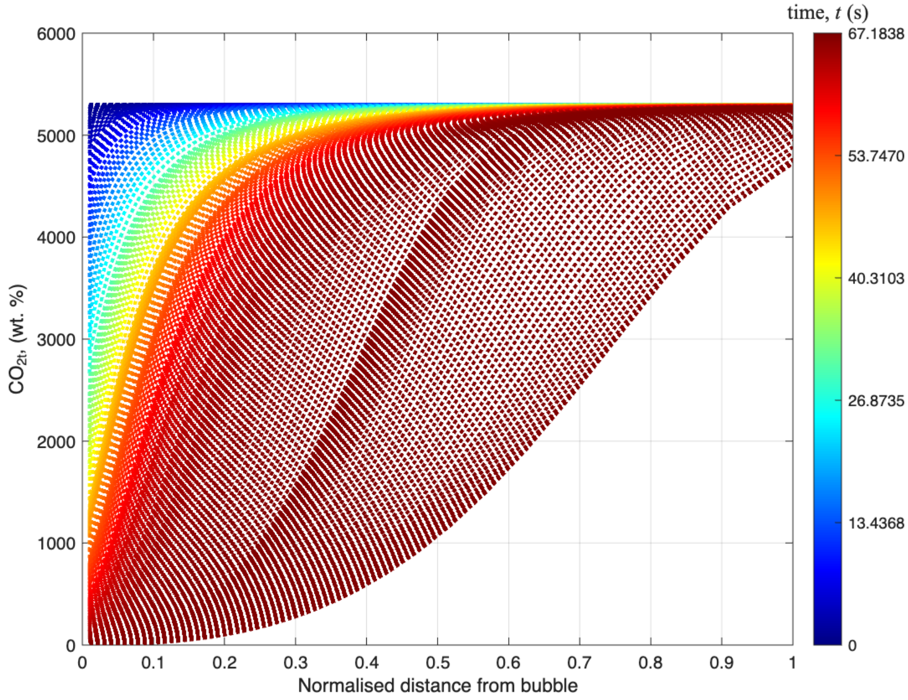

Figure 19: *Example model output for disequilibrium CO_2 concentration profiles through time, where the distance from the bubble wall has been normalised to make each profile the same length.*

By normalising the length of the melt shell, the ’folding’ effect has been removed from the graph, and it is clear how the profiles are not uniform due to the disequilibrium conditions. These graphs are generated by the model for all three volatiles, and they allow both the timescale of degassing and the degassing regime of each volatile to be presented in one figure.

Another important output from the model are degassing pathways. These show how the average concentrations of each volatile in the melt change over time, plotted against each other. An example is shown in Figure 20, which shows equilibrium H_2O-S and CO_2-S degassing pathways.

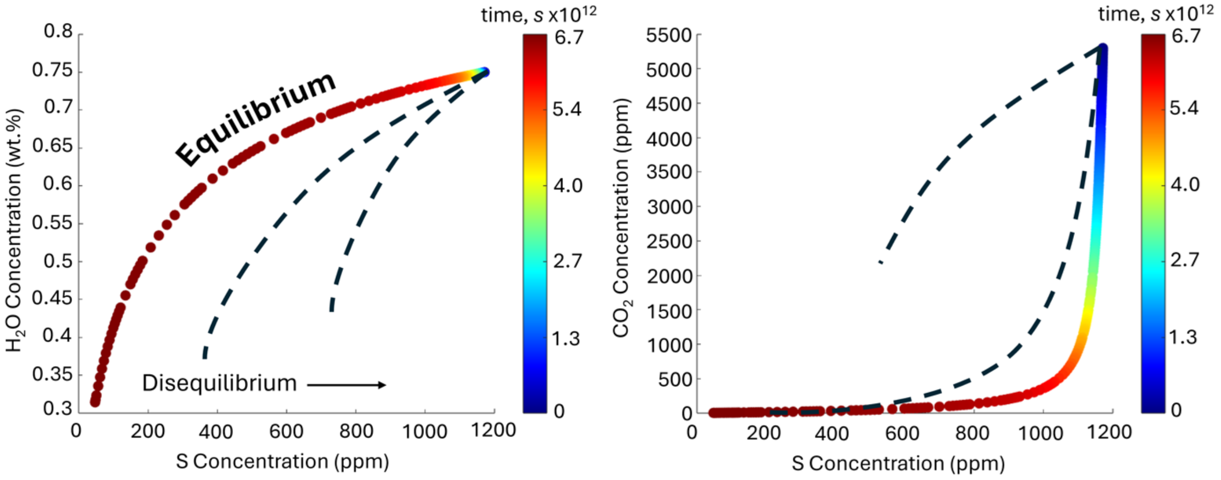

Figure 20: *Example output of degassing pathways under equilibrium conditions. Hypothetical disequilibrium pathways are indicated with a dashed line to illustrate the general trend (for actual observed disequilibrium pathways, see Figure 23).*

These represent how the average volatile concentrations in the melt change under equilibrium conditions. Possible degassing pathways for disequilibrium conditions are marked with the dashed lines. It can be seen that as the system degases further and further in disequilibrium, less and less of the volatiles exsolve and so the concentrations in the melt remain high, and do not drop as steeply. By comparing output degassing pathways to those known to be at equilibrium, the extent of disequilibrium degassing can be observed. Such plots are good for visualising how much excess of a volatile can remain in the melt under disequilibium conditions.

5.2 Disequilibrium degassing

Under the conditions of Fagradalsfjall 2021 (decompressing from ~670 to 0.5 MPa), the model was run using different decompression rates to investigate when disequilibrium degassing occurs. In order to simulate perfect equilibrium degassing, the decompression rate was set to an arbitrarily low value (10^{-10} MPa/s) to ensure all the volatiles have enough time to diffuse through the melt shell and enter the bubble.

Figure 21 shows the output concentration profiles for each volatile throughout equilibrium degassing (Panels A, B and C), and at a decompression rate of 1 MPa/s (Panels D, E and F).

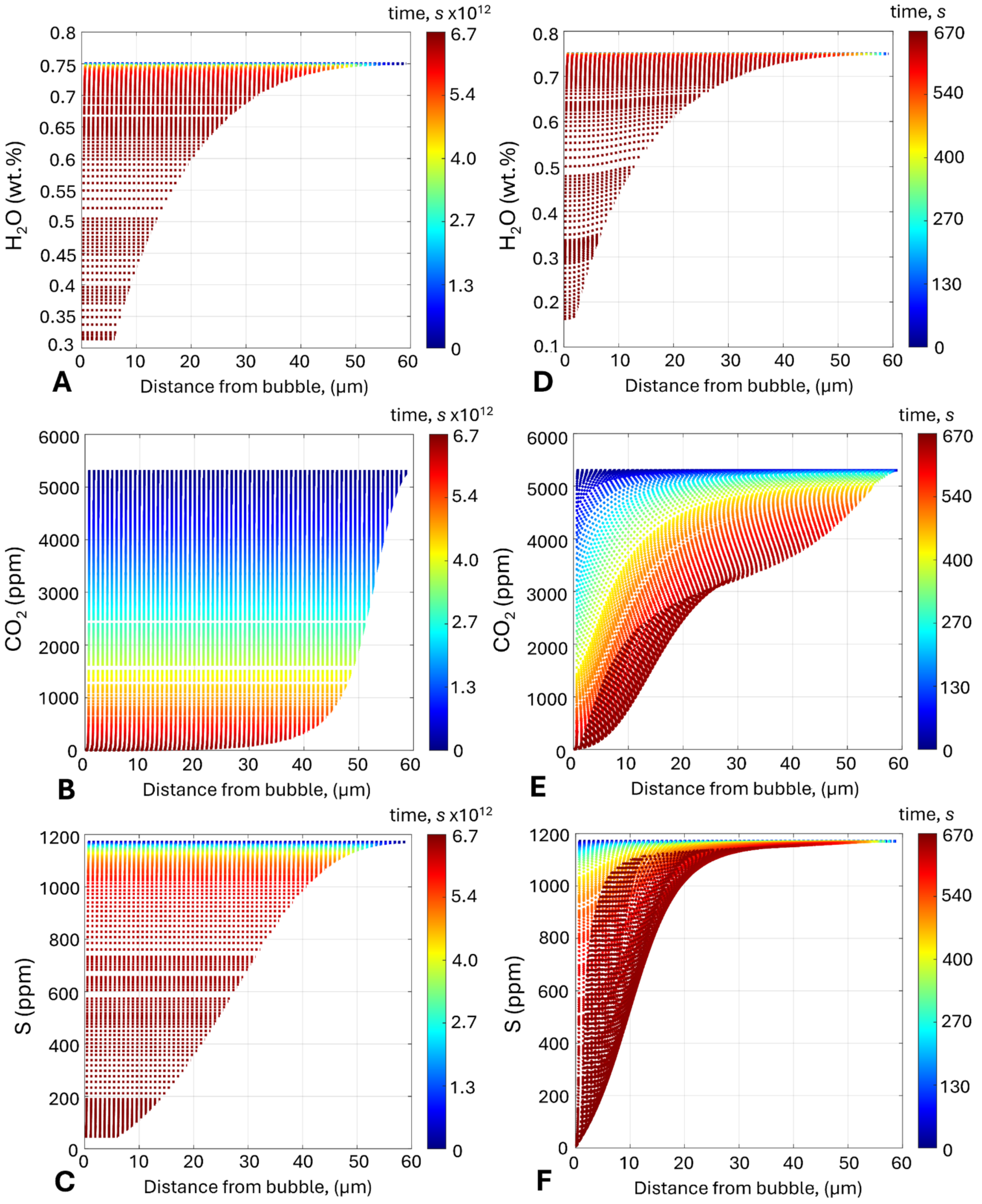

Figure 21: *Output concentration profiles for H_2O, CO_2 and S under equilibrium conditions (Panels A, B and C, respectively) and a decompression rate of 1 MPa/s (Panels D, E and F). Simulations were run using the conditions of Fagradalsfjall 2021, starting at ~670 MPa and decompressing to 0.5 MPa.*

It can be seen that under equilibrium conditions, the concentration profiles of each volatile through the melt shell are straight lines, as the concentration remains uniform throughout.

At a decompression rate of 1 MPa/s, however, these lines are no longer uniform, as the volatile concentration dramatically increases away from the bubble wall as there is not enough time for total diffusion. This disequilibrium behaviour is very minor in the H_2O profiles, with only slight instability visible at the edge of the melt shell. There is more significant disequilibrium degassing in the CO_2 profiles, with the concentration increasing much closer to the bubble wall than in the H_2O profiles, implying less diffusion occurring. Sulfur exhibits the most significant disequilibrium behaviour, with incredibly steep profiles implying only the sulfur at the bubble wall is managing to exsolve; the rest of the melt retains a higher sulfur concentration than the current saturation conditions.

As well as informing us of the disequilibrium behaviour of each volatile, Figure 21 also includes a time component, allowing inferences to be made on the timing of exsolution for each volatile. By looking at the profiles under regular equilibrium conditions, it can be seen that CO_2 begins to exsolve much earlier than the other two volatiles, which is indicative of its lower solubility. Panel B shows CO_2 to exsolve almost 50% of its original dissolved concentration in the first fifth of the total degassing period. Sulfur, alternatively, exsolves very slowly at the beginning, followed by a rapid release at lower pressures: 96% of the original dissolved sulfur was released in the final fifth of the total degassing period. H_2O exhibits similar behaviour to sulfur but more extreme: almost all of the H_2O exsolved during the final 10% of the run time. These behaviours are illustrated in Figure 22, which shows the percentage of each volatile degassed with time for equilibrium conditions of Fagradalsfjall 2021.

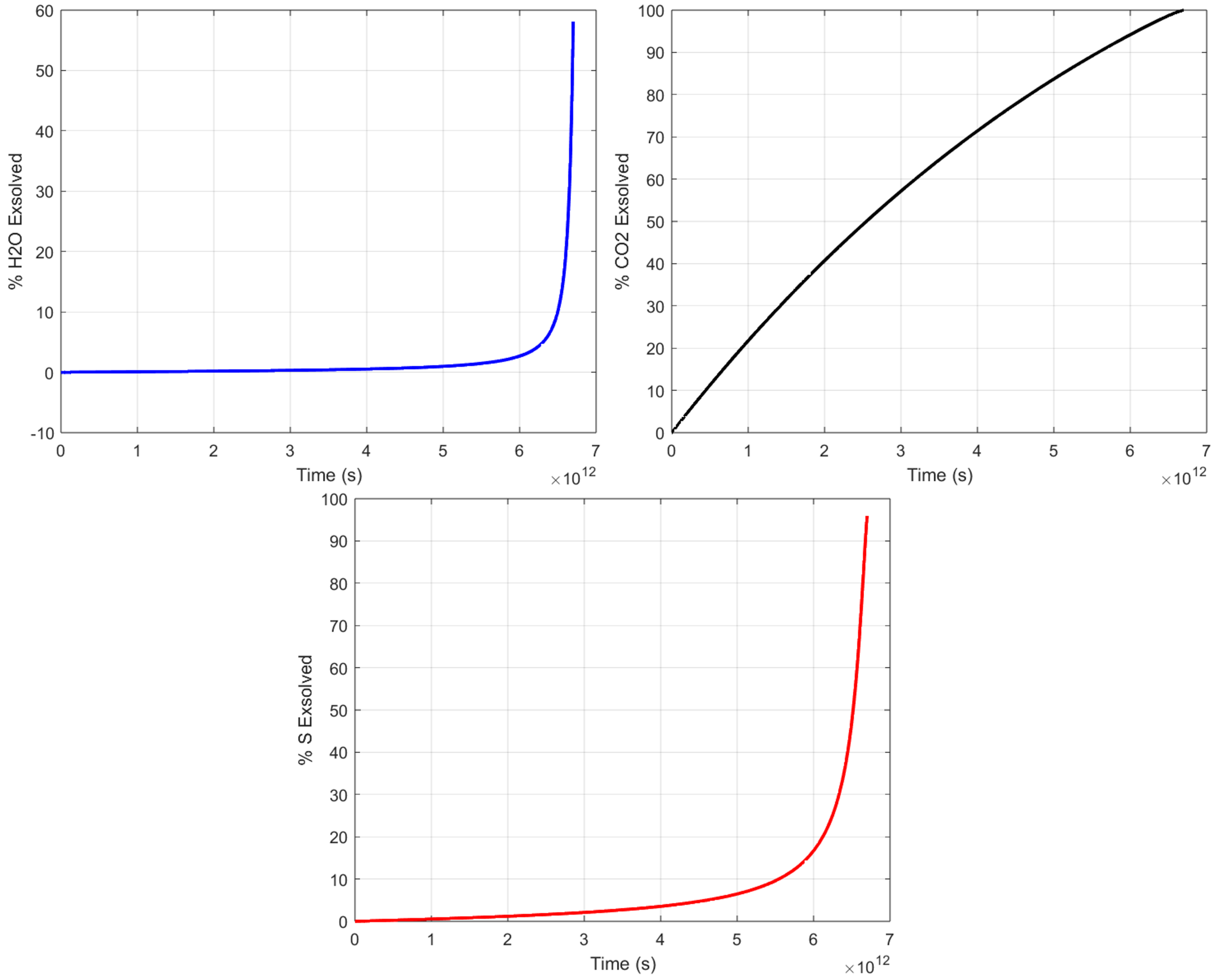

Figure 22: *Percentage of each volatile exsolved with time, for equilibrium conditions of Fagradalsfjall 2021. CO_2 exsolves early, followed by S and H_2O much later.*

5.3 Effects of decompression rate

In order to investigate the effects of disequilibrium degassing on volatile emissions, the decompression rate was varied and average concentrations of each volatile during decompression (~670 to 0.5 MPa) plotted, to visualise how degassing is affected by disequilibrium behaviour. The outputs are visualised in Figure 23.

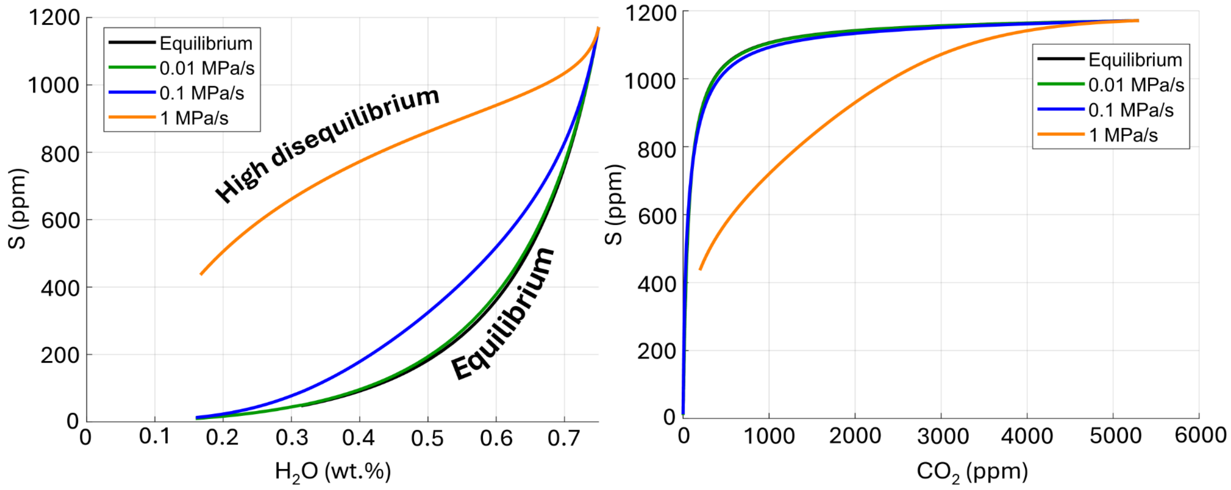

Figure 23: *Degassing pathways for a H_2O-CO_2-S system under the conditions of Fagradalsfjall 2021, using different decompression rates.*

Figure 23 shows that as decompression rate increases, the system strays further and further from equilibrium. The left plot shows the S-H_2O degassing pathway, and it can be seen that the sulfur concentration does not decrease as much as under equilibrium conditions, suggesting that sulfur's slow diffusion is playing an important role in the disequilibrium conditions. The plot on the right shows the S-CO_2 pathway, and it can be seen that both volatiles are not exsolving fast enough to meet the equilibrium line at the fastest decompression rate. Sulfur appears to be slightly more sensitive than CO_2, as the rapid exsolution of sulfur towards the end of the equilibrium runs is not occurring at faster decompression rates.

This tendency of sulfur to experience disequilibrium degassing at faster decompression rates is visualised in Figure 24.

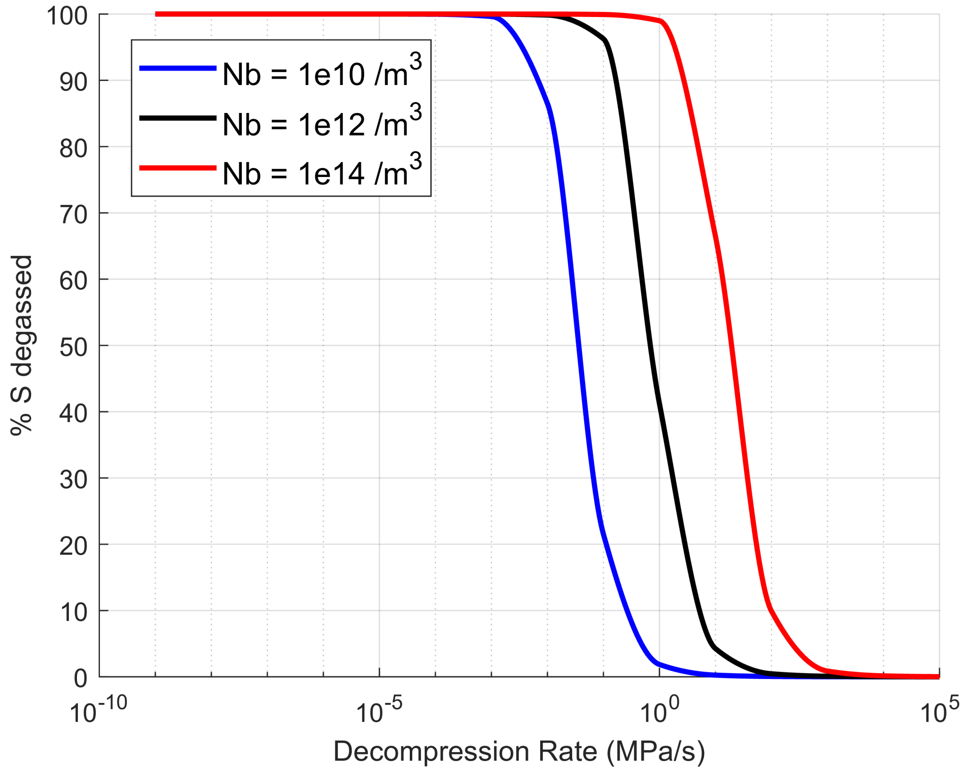

Figure 24: *Percentage of sulfur degassed against decompression rate for different bubble number densities (Nb). Modelled under the conditions of Fagradalsfjall 2021.*

It can be seen that for a bubble number density of 1×10^{12}, at a decompression rate of 0.01 MPa/s, almost 100% of the original sulfur in the melt is degassed, but at a decompression rate of 1 MPa/s, this drops to only 40%. For decompression rates above 10 MPa/s, the amount of sulfur degassed is <10%. There is therefore a very dramatic shift to disequilibrium behaviour over a relatively short range of decompression rates. This can be explained by diffusion timescales. The diffusivity of a volatile and the distance available for diffusion dictate the amount of time required for that volatile to fully diffuse. Using Equation 1, the time required for diffusion can be calculated, with varying bubble number densities represented by the change in L. Using the values for L for each bubble number density calculated by the model, and the diffusivity for sulfur, the time required for diffusion can be calculated. By comparing this time with the amount of decompression occurring, estimates can be made for the maximum decompression rate that allows sufficient time for diffusion. For bubble number densities of $\times 10^{10}$, $\times 10^{12}$ and $\times 10^{14}$ /m^3, these decompression rates are ~0.02 MPa/s, ~ 0.1 MPa/s and ~0.5 MPa/s, respectively. It can be seen that these values roughly correlate with the beginning of disequilibrium behaviour for each bubble number density in Figure 24.

5.4 Effects of other volatiles on solubility

The model for the first time allows mixed H_2O-CO_2-S solubility to be investigated, under different degassing regimes. Figure 25 shows the three-way degassing pathway for equilibrium conditions of Fagradalsfjall 2021, decompressing from ~670 to 0.5 MPa.

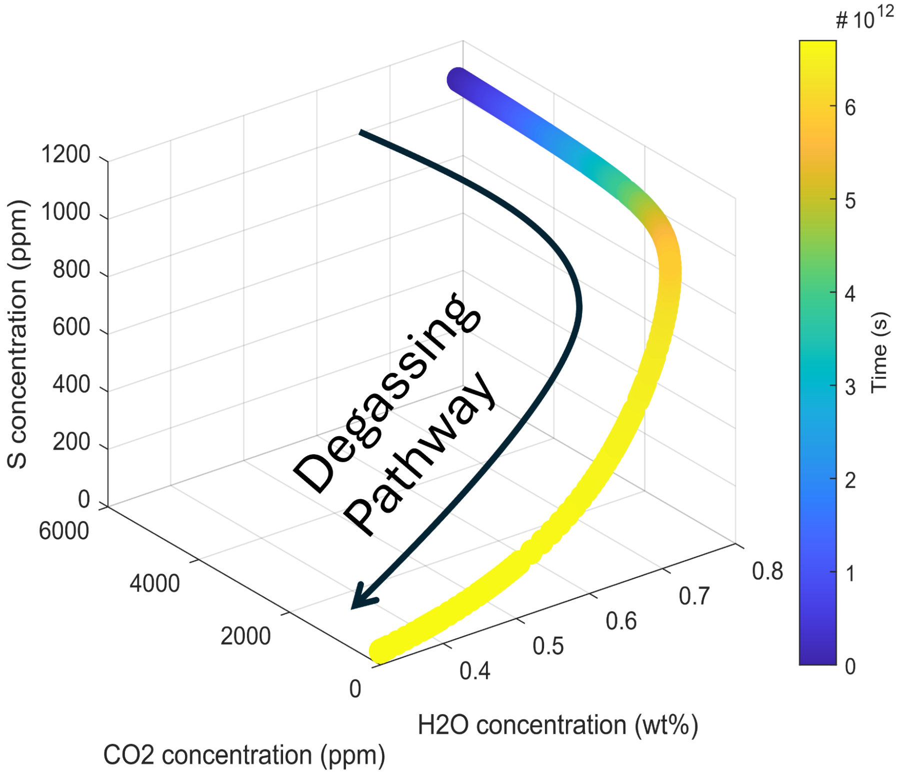

Figure 25: *Three-way degassing pathway for equilibrium conditions of Fagradalsfjall 2021, exhibiting mixed* H_2O-CO_2-*S solubility conditions.*

Figure 25 shows how CO_2 is the first to exsolve, due to it's low solubility. Sulfur exsolves very late, followed by H_2O at the very end of the run. This mixed solubility can also be used to investigate the effects of the volatiles on their exsolution depths. The flexibility of the model allows for degassing pathways to be generated for one, two or three volatile systems, allowing the effects of each on solubility to be constrained. Figure 26 shows the degassing pathways for each volatile in a three-volatile system, coloured with pressure to visualise the solubility of each.

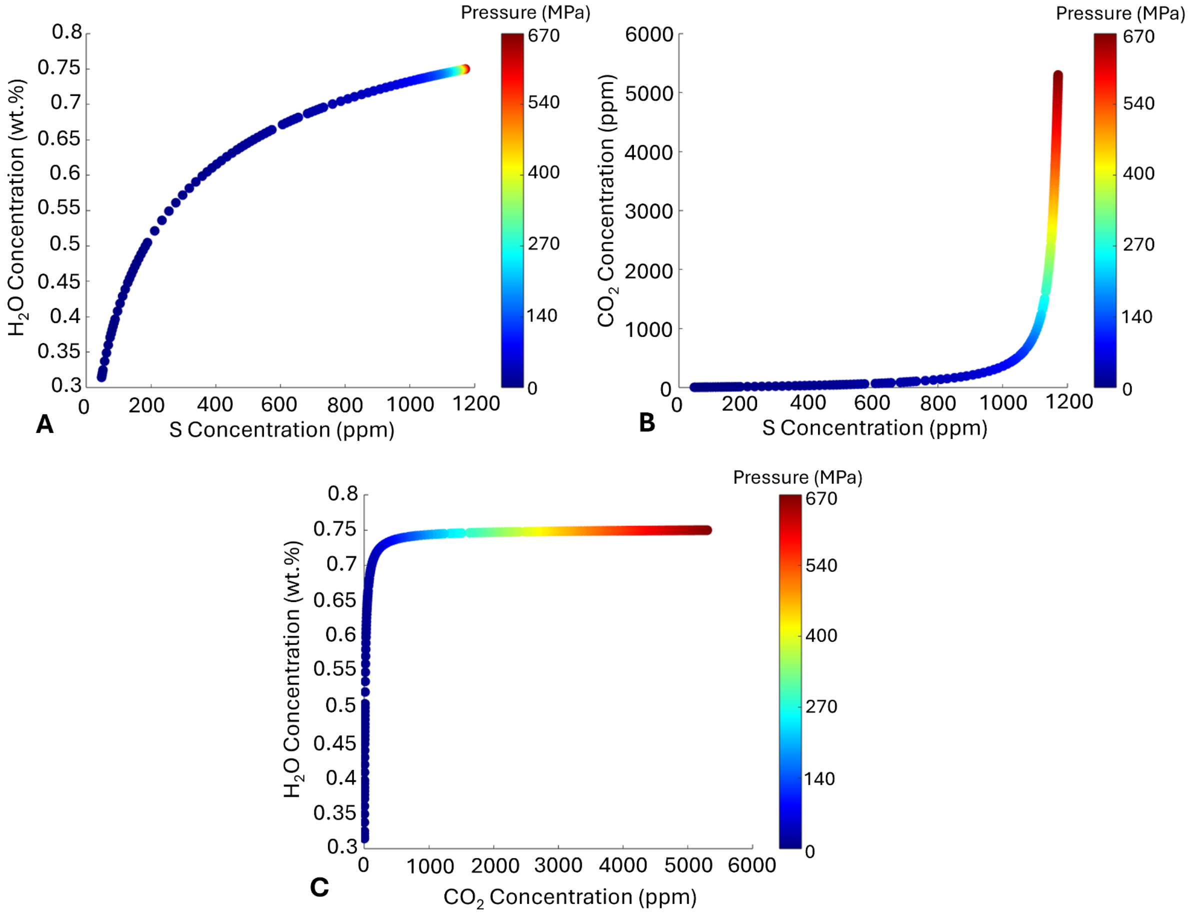

Figure 26: *H_2O-S, CO_2-S and H_2O-CO_2 degassing pathways (panels A, B and C, respectively) for a three-volatile system, under equilibrium conditions for Fagradalsfjall 2021, coloured for pressure.*

It can be seen that CO_2 exsolves at the deepest pressures, with the run starting at the saturation pressure of the system (~670 MPa). It degasses consistently until lower pressures where the melt CO_2 content is much lower, and the other volatiles begin to exsolve as their solubilities drop. This agrees with the findings of Dixon & Stolper (1995), who suggest CO_2 degasses approximately linearly with CO_2 solubility until nearly all of the CO_2 has partitioned into the vapour. S begins to exsolve at around ~250 MPa, with this increasing significantly from a pressure of around ~100 MPa. This agrees with the findings of Wallace (2001), who use sulfur emissions during volcanic eruptions to estimate the amount of sulfur being degassed as the magma rises. While their model is very generalised, the same behaviour is shown where sulfur degasses gradually, then speeds up towards the surface, followed by very rapid exsolution at very shallow depths. H_2O exsolves rapidly even shallower at around ~50 MPa, though H_2O exsolution occurs very slowly from around ~100 MPa. This also agrees with Dixon & Stolper (1995), who conclude that in a closed system, H_2O degassing is minor until very low pressures, when most of the CO_2 has partitioned into the vapour phase.

The model can also be used to investigate the molar fraction of each volatile in the bubble throughout the run. This can provide insight into how the partial pressures of each volatile change as they begin to exsolve. Figure 27 shows the molar fraction of each volatile in the bubble against pressure.

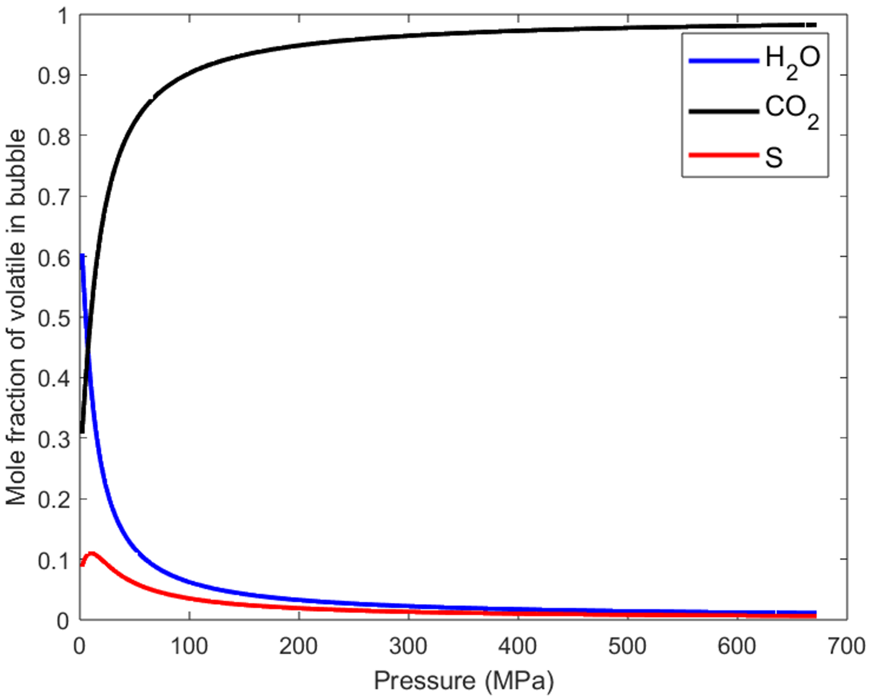

Figure 27: *Molar fractions of H_2O, CO_2 and S in the bubble against pressure, under equilibrium conditions for Fagradalsfjall 2021.*

It can be seen that at the deepest pressures the bubble is almost entirely CO_2. The small amounts of H_2O and S present in the bubble are due to their decreased partial pressures reducing solubility (caused by the bubble of CO_2), allowing deeper exsolution. S has a consistently low molar fraction in the bubble, due to its lower abundance in the system. The slight sudden decrease in S molar fraction at the shallowest depths is likely due to the rapid exsolution of H_2O near the surface, highlighting the complexities of multi-volatile solubility. H_2O can be seen to rapidly exsolve at shallower depths, and makes up around ~60% of the bubble's molar mass at the end of the run. CO_2 drops to 30% of the molar mass, and S finishes at around 10%.

The effects of CO_2 in the system can be constrained by running the model as a two-volatile system. In order to change the number of volatiles in the model, the component models for solubility must be changed accordingly. The component solubility models used for a one, two and three-volatile system are listed in Table 4.

Volatiles	**H_2O solubility model**	**CO_2 solubility model**	**S solubility model**
$H_2O + CO_2 + S$	Iacono-Marziano et al., (2012)	Iacono-Marziano et al., (2012)	Ding et al., (2023)
$H_2O + S$	Shishkina et al., (2010)	-	Ding et al., (2023)
H_2O	Shishkina et al., (2010)	-	-

Table 4: *Component solubility models used when modelling a one, two or three-volatile system.*

Note that the component models not mentioned in Section 3.2.2 were prexisting within the original Bubble-Growth Model, and so have been validated in Coumans et al., (2020), and were used for simplicity.

The degassing pathway for a H_2O-S system is shown in Figure 28.

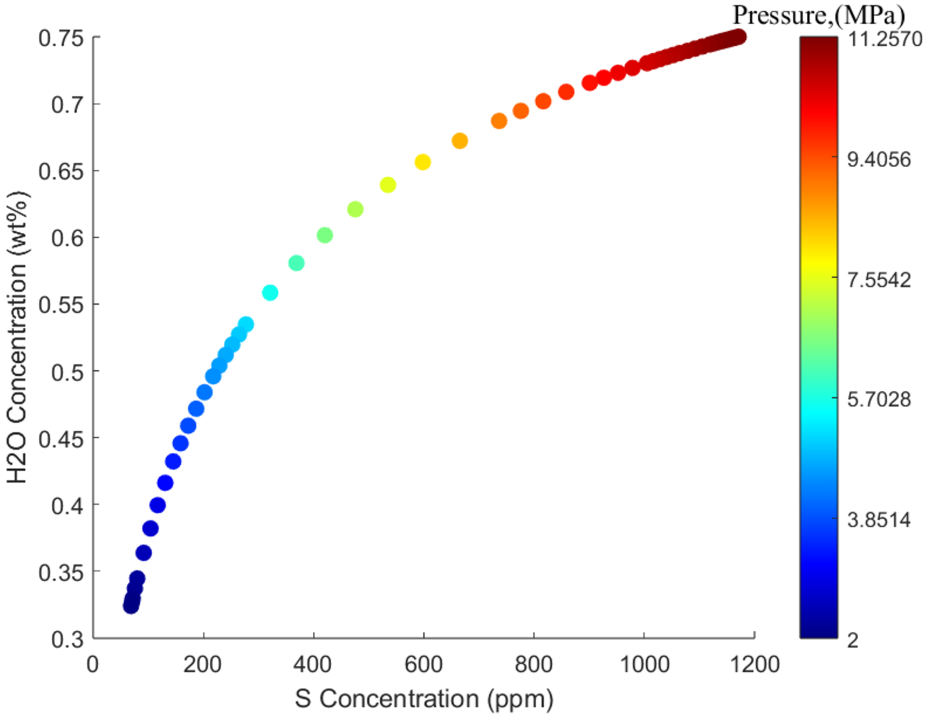

Figure 28: *H_2O-S degassing pathway for a two-volatile system, under equilibrium conditions for Fagradalsfjall 2021, coloured for pressure.*

Without CO_2, the saturation pressure of the system drops to ~11.4 MPa. It can be seen in Figure 28 that sulfur exsolves significantly first, and then both volatiles exsolve rapidly from shallower pressures of ~5.5 MPa. These are much lower pressures for rapid H_2O and S exsolution than in the three-volatile system.

The molar fractions of H_2O and S in the bubble throughout the run are shown in Figure 29.

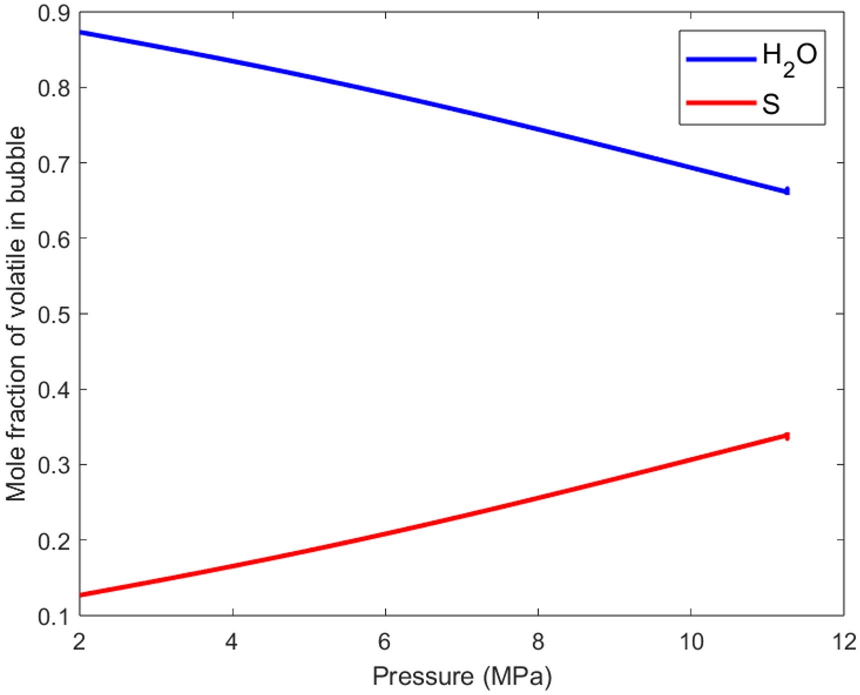

Figure 29: *Molar fractions of H_2O and S in the bubble against pressure for equilibrium conditions of Fagradalsfjall 2021.*

It can be seen that the molar fraction of S in the bubble decreases throughout the run, as more and more H_2O exsolves. At the beginning, the molar fraction of sulfur in the bubble is relatively high considering the small melt content compared to H_2O. This is because of sulfur's lower solubility and therefore deeper exsolution depth compared to H_2O. This decreases the partial pressure of H_2O across the bubble wall, driving earlier exsolution.

In order to constrain the effects of S on the saturation pressure of the system, it is possible to run the model with H_2O as a single volatile, similar to the original Coumans et al., (2020) model. Figure 30 shows H_2O concentration with pressure for a single-volatile system.

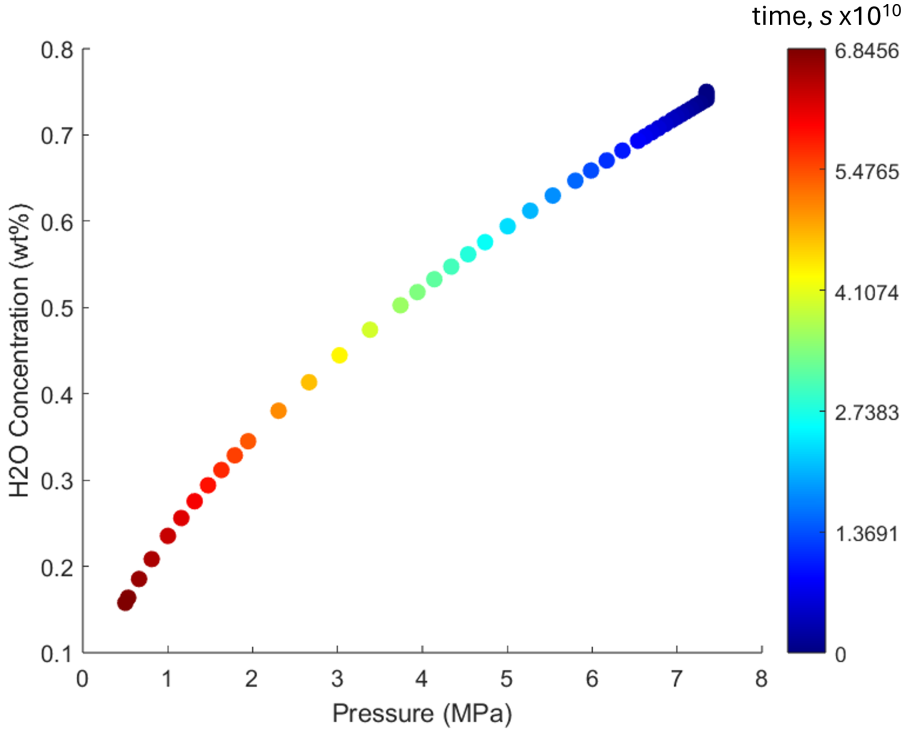

Figure 30: *H_2O degassing pathway for a single-volatile system, under equilibrium conditions for Fagradalsfjall 2021, coloured for time.*

Without sulfur, the saturation pressure of H_2O drops to ~7.5 MPa. It can also be seen in Figure 30 that H_2O begins to exsolve slightly faster below pressures of ~2MPa, again a much shallower depth for rapid exsolution than in the multi-volatile systems.

5.5 Recreating Fagradalsfjall 2021

The model was also used to investigate an eruption case study: Fagradalsfjall 2021, to attempt to constrain whether sulfur was degassing under disequilibrium conditions. The modelled eruptive conditions and their sources are listed in Table 5. Decompression was again set from ~670 MPa (saturation pressure) to 0.5 MPa.

Parameter	Value	Source
Composition	*see Appendix B*	Bindeman et al., (2022)
Melt density	2750 kg m^{-3}	Daði (2021)
Bubble number density	1×10^{12} m^3	Colombier et al., (2021)
Temperature	1200°C	Hafsteinsðottir (2021)
Decompression rate	0.003 MPa/s	Marshall et al., (2024)
Oxygen fugacity	$\Delta FMQ + 0$	Ranta et al., (2024)
Initial H_2O concentration	0.75 wt%	Radu et al., (2023)
Initial CO_2 concentration	5300 ppm	Halldorssen et al., (2022)
Initial S concentration	1171 ppm	Ranta et al., (2024)

Table 5: *Input conditions used in the model for recreating Fagradalsfjall 2021.*

Importantly, magma ascent rate (i.e., decompression rate) is thought to have varied greatly during this eruption as it shifted periodically between effusive behaviour and hawaiian-style fountaining, which is associated with faster ascent rates. Marshall et al., (2024) report a magma ascent rate of between 0.02 and 0.09 m/s, which corresponds to a decompression rate range of $5.3 \times 10^{-4} - 2.4 \times 10^{-3}$ MPa/s. This is still relatively slow for producing hawaiian style fountaining behaviour, and based on the model of Parfitt & Wilson (1995) and a water content of 0.75 wt%, the ascent rate needs to be at least 0.1 m/s to produce the lava fountaining observed. Due to the lack of literature on the decompression rate during fountaining events of Fagradalsfjall 2021, the following runs use a decompression rate of ~0.003 MPa/s, in line with the estimate from Marshall et al., (2024). The model outputs using these conditions are shown in Figure 31.

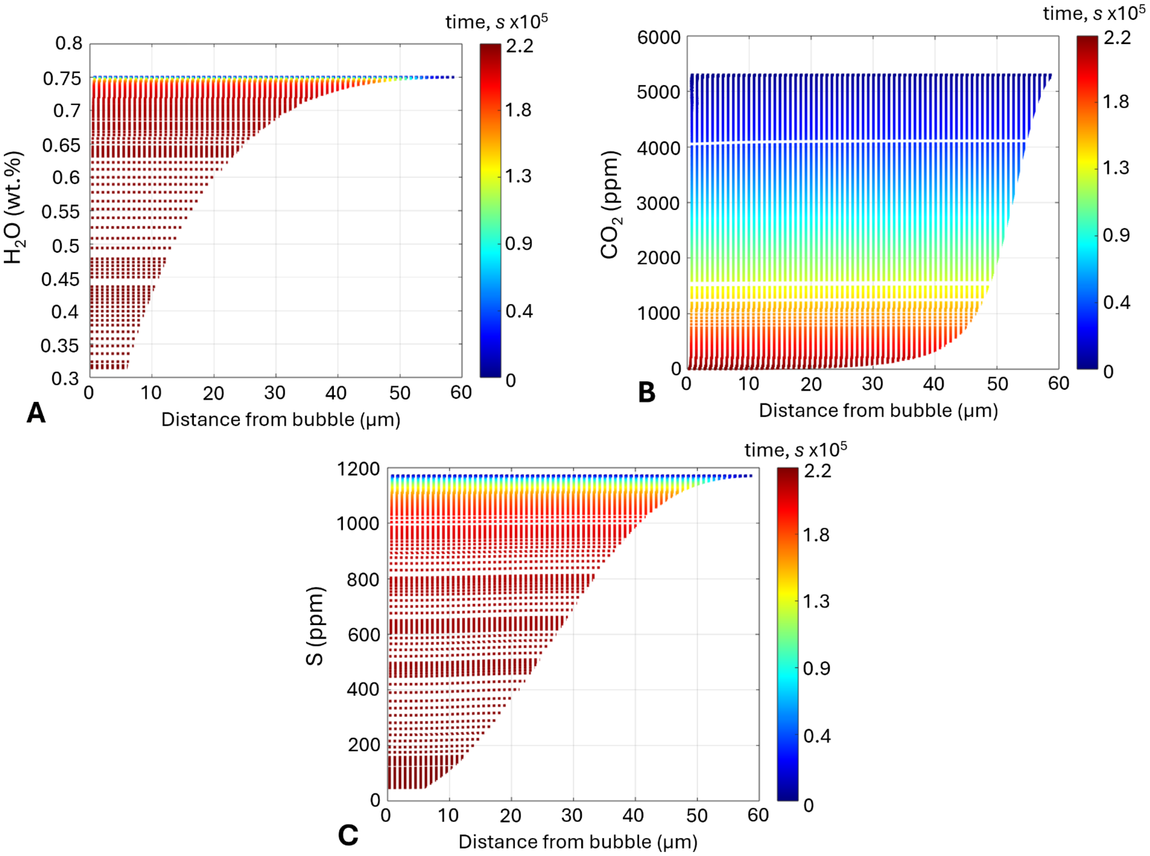

Figure 31: *Concentration Profiles for H_2O, CO_2 and S (Panels A, B and C respectively) under the conditions of Fagradalsfjall 2021, using a decompression rate of 0.003 MPa/s.*

It can be seen that all three volatiles appear to be in equilibrium. There is only a very slight wobble in the sulfur concentration profiles, but this is not enough to be significant. To further investigate these conditions, the final concentration profile for each volatile can be plotted (Figure 32).

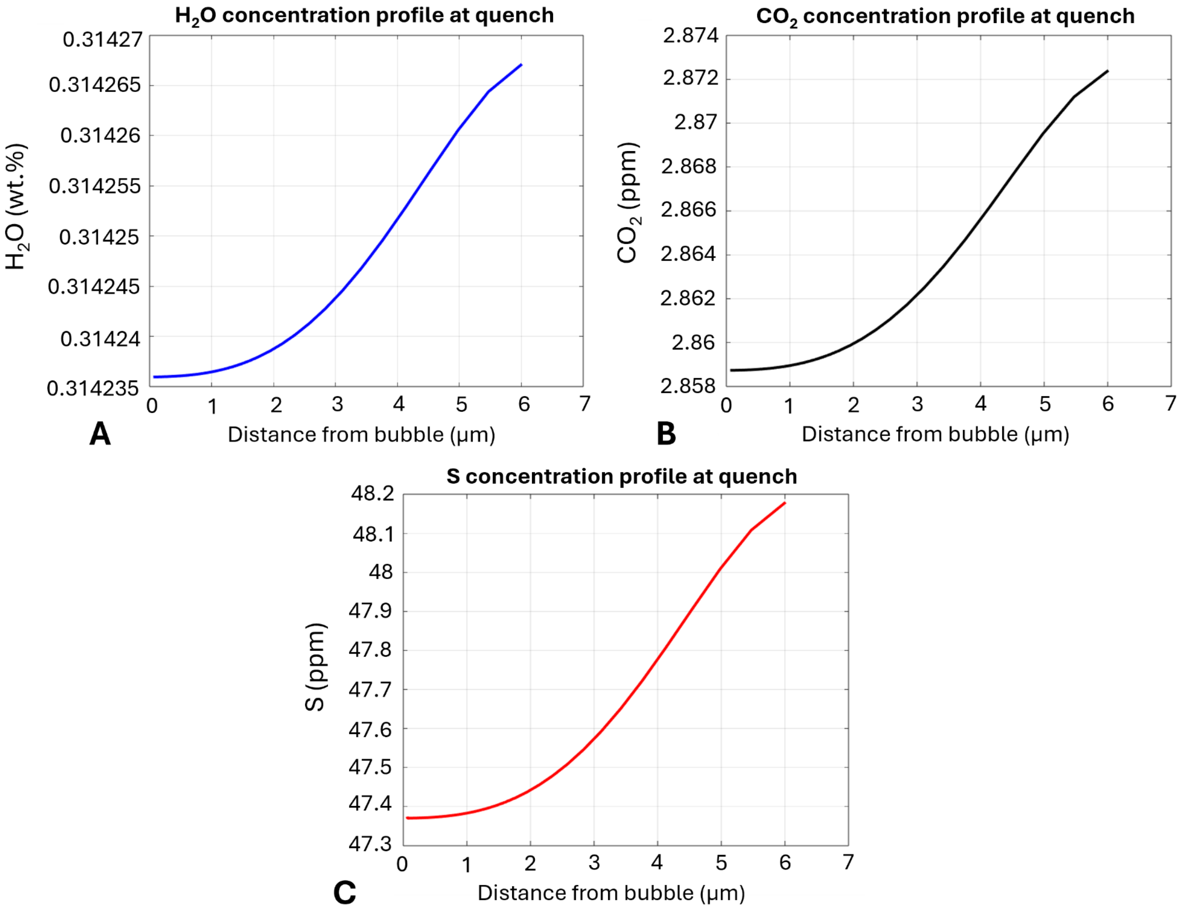

Figure 32: *Final output concentration profiles for H_2O, CO_2 and S (panels A, B and C respectively) for the conditions above.*

It can be seen that while the concentration of each volatile does increase away from the bubble wall, this variation is of such a small amount that the system can be considered in equilibrium at the time of quench. Sulfur however has the largest increase in concentration when moving away from the bubble wall, increasing by ~1.69% across the 7 μm of melt shell. CO_2 increases by ~0.47%, and H_2O by ~0.0096%.

The estimated degassing pathways can also be modelled for this eruption scenario (Figure 33).

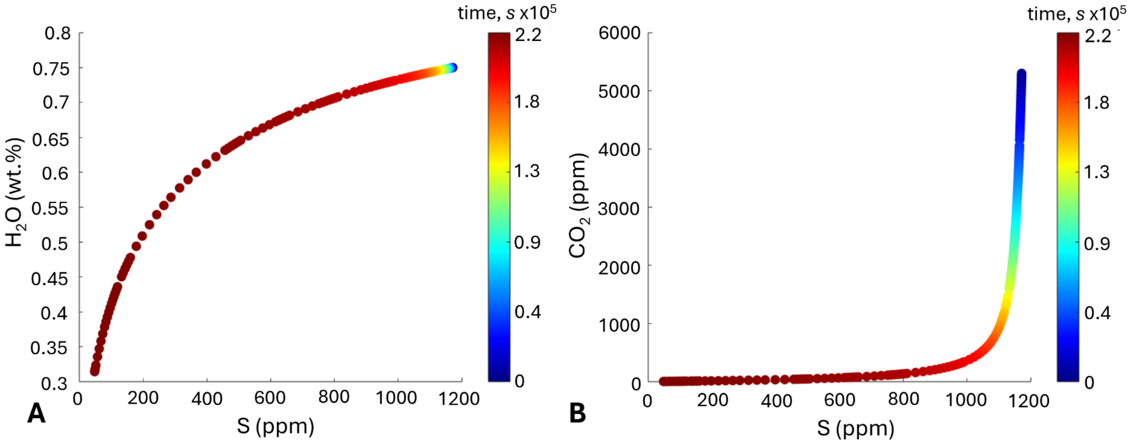

Figure 33: *Degassing pathways for H_2O-S and CO_2-S (panels A and B, respectively) for the modelled Fagradalsfjall 2021 scenario.*

It can be seen once again that CO_2 is first to exsolve, followed by S and then H_2O. Almost all of the CO_2 has already exsolved by the time S begins to drop significantly, and both H_2O and S concentrations drop very rapidly towards the end of the run. The concentrations tending towards 0 at the end of the run (set at 0.5 MPa to maintain model stability) suggests that the lavas erupted during this event were largely volatile depleted.

Finally, the modelled degassing pathways from Fagradalsfjall 2021 were compared with melt inclusion data and volatile concentrations in glasses from Halldorrssen et al., (2022). Here, only the CO_2-S pathways are compared, as this is not often done in the literature. Modelled degassing pathways using a decompression rate of 0.003 MPa/s and 1 MPa/s are plotted with the melt inclusion and glass data in Figure 34.

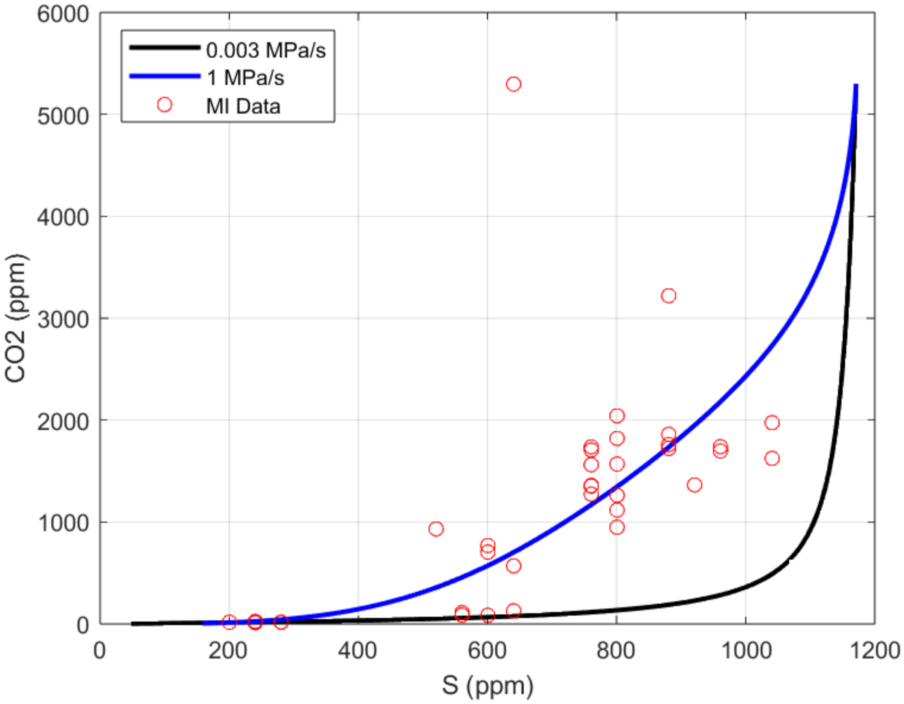

Figure 34: *Modelled CO_2-S degassing pathways plotted against melt inclusion and glass data from Halldorssen et al., (2022). Degassing pathways were modelled at decompression rates of -0.003 MPa/s and -1 MPa/s.*

It can be seen that the slower decompression rate representative of effusive behaviour is degassing towards an equilibrium trend, however this does not match the natural samples. In order to recreate the trend exhibited by the melt inclusion and glass data, the degassing pathway must exhibit disequilibrium behaviour, i.e. experience a faster decompression rate. A decompression rate of -1 MPa/s (i.e, the upper-end of values corresponding to hawaiian fountaining behaviour, Parfitt & Wilson, 1995) shows an excellent match with the natural samples, suggesting that they experienced faster decompression rates than those found in the effusive behaviour of the eruption.

6 Discussion

6.1 Disequilibrium degassing

The results show that sulfur is most likely to exhibit disequilibrium behaviour, followed by CO_2, and H_2O is not prone to degas in disequilibrium unless under extremely fast decompression rates. This can be related to the diffusivity of each volatile. In basaltic melts, sulfur diffusion is reported to be two times lower than CO_2, and two orders of magnitude lower than H_2O (Freda et al., 2005). The model shows this behaviour due to the incorporation of volatile diffusivities, and can therefore be used to investigate under what conditions each volatile degasses in disequilibrium.

6.1.1 Effects of decompression rate

Due to diffusion being the main control on whether the system degasses in equilibrium, decompression rate is extremely important, as it dictates the timescale of degassing and therefore how much time is available for the volatile to diffuse through the melt shell and enter the bubble. Figure 23 suggests that the system remains fairly close to equilibrium until a certain threshold decompression rate is crossed, causing the system to enter extreme disequilibrium. This is shown in Figure 24, which shows how the amount of sulfur degassed drops dramatically over the decompression rate range of ~0.1–1 MPa/s, with 0.1 MPa/s being the maximum estimated decompression rate that provides enough time for full diffusion (for Nb $\sim 1{\times}10^{12}$). This is also the range of decompression rates found in natural basaltic systems, associated with more explosive basaltic eruptions (Cassidy et al., 2018). This suggests that while disequilibrium sulfur degassing occurs at lower decompression rates (~0.01 - 0.1 MPa/s), it is not significant until the decompression is an order of magnitude faster, and the time available for diffusion is no longer sufficient. However, it is important to note that this switch to disequilibrium behaviour occurs at slower decompression rates for lower bubble number densities (from ~0.001 MPa s^{-1} for $N_b \sim 1{\times}10^{11}$) and at higher rates for higher bubble number densities, because of the change in distance available for diffusion. This suggests that for basaltic eruptions experiencing low-energy explosive behaviour (hawaiian fountaining - low strombolian), disequilibrium degassing of sulfur is likely occurring, but to different extremes depending on the average bubble number density of the magma, and the diffusion timescale. While such behaviour appears to be on the threshold of disequilibrium degassing, it is likely that for more explosive behaviour (sub-plinian - plinian), disequilibrium degassing has a large effect on the volatile emissions observed, particularly for sulfur and to some extent, CO_2. However, this is purely speculative and further testing and applications of the model to different eruptive conditions is necessary to fully investigate this.

6.1.2 Implications

Understanding whether a volcanic system is degassing in equilibrium is important for interpreting natural samples, measuring volatile emissions, and potentially predicting changes in eruptive behaviour; an important part of eruption forecasting.

Being able to quantify whether a system is degassing in disequilibrium is important for the interpretation of measured gas fluxes, something which is used widely within volcano monitoring (e.g. Aiuppa et al., 2010). This is particularly relevant for sulfur, which is used more extensively due to the lack of other natural sources compared to CO_2 and H_2O (e.g. Kilauea, Sutton et al., 2001). Within the literature, reductions in SO_2 flux have been reported as indicating both increasing and decreasing eruption likelihood, due to the many complex processes occuring within a volcanic system (Oppenheimer et al., 2011). For example, Stix et al., (1993) report a decrease in SO_2 flux at Galeras volcano as indicative of a reduction in permeability, leading to pressurisation of the magma and an increased likelihood of eruption. However, Watson et al., (2000) report decreasing SO_2 flux on Montserrat as indicative of a reduced volatile content in the magma, and therefore reduced eruption likelihood. Interpretations of volatile emissions are therefore usually specific to individual volcanoes and their typical behaviour, rather than generalised. This model has the potential to provide a user-friendly tool to estimate the degassing regime of a volcanic system with a few basic inputs, helping to remove speculation around intepreting gas emissions and the processes occuring at depth. Such a tool in volcano monitoring could be used to help pinpoint sources of changes in SO_2 flux, and potentially improve the accuracy of eruption forecasting.

This new understanding of the conditions which promote disequilibrium behaviour of the three most abundant volcanic volatiles in basaltic systems can be applied to natural samples, to help interpret eruptive conditions. Currently, only *EMBER* (Georgeais et al., 2021) is able to calculate decompression rates from diffusion profiles and therefore take into account disequilibrium degassing, but it does not take into account bubble growth, or provide information on predicted porosity and vesicle radii etc. This new version of the bubble-growth model is able to provide estimates on decompression rate similar to *EMBER*, and can be used as an additional benchmark, and/or for constraining other pre-eruptive conditions such as temperature, pressure, bubble evolution through time etc.

Furthermore, the evidence for the parameter space promoting drastic changes in disequilibrium behaviour occurring over the decompression rate range of natural systems could have important implications for how we model magma degassing. The results suggest that disequilibrium degassing of sulfur could be occurring in natural systems more commonly than is currently thought, and that the natural variation of decompression rate during an eruption could be enough to switch from an equilibrium regime to extreme disequilibrium over short timescales. This could provide important insight when interpreting sudden changes in eruptive behaviour. It is therefore necessary to investigate this effect further, and take it into account when interpreting degassing regimes at volcanic systems which experience these conditions.

6.2 Effects of other volatiles on solubility

The model's ability to run as a one, two or three-volatile system highlights the importance of mixed solubility. This especially applies to the presence of CO_2, which increased the saturation pressure by over ~600 MPa. This has been found in several numerical and experimental studies, and highlights the importance of including CO_2 when calculating saturation pressures and constraining degassing histories (Dixon et al., 1991; Duan, 2014). Interestingly sulfur also increased the saturation pressure compared to a H_2O-only system, due to its slightly lower solubility. This was also found by Hughes et al., (2024), when investigating the effects of sulfur and oxygen fugacity on saturation pressure. Hughes et al., (2024) conclude that sulfur has a small effect on saturation pressure, unless it is in the vicinity of the 'sulfur solubility minimum' ($0 < \Delta FMQ > +2$), which is the case under the conditions of Fagradalsfjall 2021 used to test our model. Hughes et al., (2024) also found that for mid-ocean ridge basalts from the Reykjanes peninsula, the presence of sulfur has a significant effect on the saturation pressure. This is contrary to the results from the decompression experiments of Lesne et al., (2011), which conclude that changing the amount of sulfur in the melt does not affect the behaviour of H_2O or CO_2. However, this is likely because only a small amount of sulfur is required to affect the saturation pressure of the system, and so once sulfur is present, changing the amount does not vastly affect the system. Since Lesne et al., (2011) did not include a run containing zero sulfur, they can only conclude that changing the amount of sulfur has no effect, rather than the presence of sulfur itself. Few other experimental studies of mixed-volatile solubility exist, and so our model can be used to help understand the degassing behaviour of mixed-volatile basalts, which has both experimental and natural volcanological applications.

6.3 Recreating Fagradalsfjall 2021

The results from modelling the 2021 Fagradalsfjall eruption suggest that the system first became saturated at around 670 MPa (~25 km depth) due to the low solubility of CO_2, and degassed dominantly under equilibrium conditions. This agrees with the results Halldorsson et al., (2022) who estimate a depth of around 20 km from clinopyroxene cores, and of Moussallam et al., (2024) who use $\delta 13$C emissions to estimate a saturation depth of ~27 km. They also report the system to degas in equilibrium. This supports the model's accuracy and applicability to natural systems, and provides valuable insight into the degassing processes which occurred during this eruption. This is further supported by the work of Scott et al., (2023), who interpret equilibrium degassing at shallow depths for the 2021 eruption. By using the *D-Compress* (Burgisser et al., 2015) equilibrium degassing model, they estimate residual CO_2, H_2O and S gas contents at atmospheric pressure of <1, 400 and 700 ppm, respectively. Their measured CO_2, H_2O, and S concentrations in groundmass glass from this eruption are reported as (18.0 ± 3.9) ppm, (720 ± 63) ppm, and (186 ± 100) ppm, respectively. While the bubble-growth model can only track degassing to ~2 MPa for a decompression rate of ~0.003 MPa/s (due to the model running too slow and collapsing below this value), final volatile contents are predicted to be ~2.9 ppm, ~3100 ppm and ~48 ppm, respectively. While these values do not perfectly match the natural samples, it is important to note that these are for a depth of ~0.076 km, rather than at the surface. This could explain the higher predicted H_2O contents, since H_2O exsolves rapidly in the shallow subsurface. Predicted CO_2 and S however are lower than measured samples, although both values lie close to the uncertainty range of the measured samples. This could be explained by the faster decompression rates observed during hawaiian fountaining behaviour. This is highlighted in Figure 34, which shows that equilibrium degassing does not recreate the observed melt inclusion and glass data from Halldorrsson et al., (2022). This data instead exhibits a close match with the degassing pathway observed using a decompression rate of 1 MPa/s. This decompression rate represents moderately violent hawaiian fountaining behaviour, in a basalt with 0.75 wt% water, using the model of Parfitt & Wilson (1995). It is important to note that this is a relatively fast ascent rate, which may inhibit the formation of melt inclusions. However, the data points with the lowest volatile contents are measured from glasses, which can preserve volatile concentrations even under fast ascent rates. This therefore suggests that these samples could have experienced hawaiian fountaining behaviour, and therefore disequilibrium degassing. This could explain the higher CO_2 and S contents found in measured samples by Scott et al., (2023), as disequilibrium degassing would result in higher residual volatile contents in groundmass glasses. Using this faster decompression rate of 1 MPa/s, the model predicts final CO_2, H_2O and S contents of ~5.9 ppm, ~720 ppm and ~160 ppm. These are a much better match with the measured values from Scott et al., (2023) with all of the values being within the uncertainty range except for CO_2, which is off by 8 ppm. The value for final H_2O content is an exact match with that measured by Scott et al., (2023), and this improved accuracy is also likely from the model being able to run to a depth of ~3.5 m (~ 0.1 MPa) at this decompression rate, accounting for late H_2O exsolution. It can therefore be concluded that the 2021 Fagradaslfjall eruption experienced equilibrium degassing during effusive episodes, and disequilibrium degassing during hawaiian fountaining behaviour, at a decompression rate of around ~1 MPa/s. Overall, the predicted final volatile contents from the bubble-growth model are very close to natural data, supporting the accuracy of the model and its applicability to natural systems. The ability of the model to recreate degassing histories to such accuracy therefore has large implications for interpreting natural data and understanding eruptive processes.

6.4 Future applications of the model

Due to the user-friendly design of the model, it has the potential to be used in volcano-monitoring, and during eruptions to help interpret eruptive activity. By inputting the composition, volatile contents and predicted P-T-t path, the model can inform on whether the system is likely to experience disequilibrium degassing, which is important for predicting potential increases in explosivity and a more violent eruption, as well as interpreting gas emissions. Alternatively, the model can be used to make interpretations on previous eruptions, by recreating degassing pathways and volatile concentration profiles around vesicles. By using the model in conjunction with natural samples, it has the potential to improve our understanding of degassing regimes which is vital for understanding shifts in eruptive activity, one of the main challenges in eruption forecasting.

6.5 Further work

In order to test the capabilities of this model it would be interesting to run decompression experiments on silicate melts, and measure H_2O, CO_2 and S contents surrounding the resulting vesicles. While decompression experiments are used frequently within volcanology, sulfur is rarely investigated, due to the complications of additional sulfur phases and the difficulty controlling fO_2 (this has however been done in some studies, such as Fiege et al., 2015). Such experiments however could determine whether the model can accurately reproduce volatile concentration profiles, and constrain the conditions over which it is most reliable. This would allow the model to be more confidently applied to natural systems.

Further work could also involve explicitly modelling SO_2 and H_2S. The sulfate ratio is already calculated within *Sulfur_X* to account for sulfur speciation, and so turning this into an output would allow SO_2 and H_2S to be modelled separately, producing a four-volatile system. This would make the model more applicable to volcano monitoring efforts, as SO_2 flux is used widely within this field, rather than sulfur emissions as a whole.

Another use of sulfur within volcanology is measuring sulfur isotope fractionation, to estimate the mantle source of different magmas (Marini et al., (2011). While this method has been around for decades, one of the main challenges is determining what amount of this isotope fractionation occurs from shallow-depth magma degassing (Beaudry et al., 2018). Current models for this are only able to assume equilibrium degassing, and another highlighted challenge is the effects of diffusion-induced disequilibrium sulfur degassing on sulfur isotope fractionation during bubble growth (Graham, 2009). The results from Fortin et al., (2019) however suggest that the diffusive effects of sulfur in basalts has no effect on isotope fractionation. This model therefore has the potential to be applied to this field, by incorporating calculations for sulfur isotope fractionation. This would allow the sulfur isotope fractionation to be modelled along different degassing pathways, including disequilibrium conditions. This could provide valuable insight when constraining different mantle sources at volcanic systems worldwide.

Because of the model's simple and easy to use framework, it is possible for more volatiles to be added in the future. As long as constituent models for solubility and diffusivity exist, in theory the bubble-growth model could be extended to incorporate even more volatiles, with the flexibility of adding or removing them as required. This would allow the model to be applied to more volcanic systems and increase its complexity, increasing its applicability to natural systems. While extensive research has been performed on degassing of H_2O and CO_2, little work has been done on other magmatic volatiles, so this provides a promising avenue for future research.

Finally, in order to improve the implementation of sulfur in the model, mechanisms for sulfide and sulfate saturation could be included. Being able to model the degassing behaviour of sulfur with an additional phase present would be invaluable for understanding more sulfur-rich systems, particularly arc magmas where mechanisms behind sulfur degassing are debated due to the 'excess sulfur issue' (Sharma et al., 2004). However, the current available data and theory in this field are not sufficient to develop such a model, though this may change in the future.

7 Conclusions

A bubble-growth model has been adapted to run a H_2O-CO_2-S system, accounting for sulfur speciation and mixed solubility. The model agrees well with natural samples, and has the potential to be applied to natural systems to better understand degassing behaviour. The model shows that sulfur is more prone to disequilibrium behaviour due to its low diffusivity, followed by CO_2, and H_2O requires very high decompression rates to degas in disequilibrium. Findings from the model suggest that sulfur switches to disequilibrium behaviour over the range of decompression rates found in natural systems, suggesting disequilibrium sulfur degassing may be more prevalent than previously thought. The mixed solubility within the model suggests that CO_2 greatly increases the saturation pressure of the system and causes small amounts of H_2O and S to be degassed earlier. Sulfur has the same effect on H_2O but to a much smaller degree. The model also successfully recreated the conditions of Fagradalsfjall 2021, exhibiting both equilibrium and disequilibrium degassing depending on eruptive behaviour. A decompression rate of $\sim$1 MPa/s has been estimated for the hawaiian fountaining observed during this eruption, and natural data agrees very closely with the model. Finally, the model has the potential to be used in a volcano monitoring context, helping to interpret sulfur emissions and infer processes occurring at depth. It also has the potential to be used to interpret natural samples from historical eruptions, and improve our understanding of different degassing regimes.

8 References

1. Aiuppa, A., Moretti, R., Federico, C., Giudice, G., Gurrieri, S., Liuzzo, M., Papale, P., Shinohara, H. and Valenza, M. (2007). Forecasting Etna eruptions by real-time observation of volcanic gas composition. *Geology*, 35(12), p.1115. doi:https://doi.org/10.1130/g24149a.1.

2. Alessandro Aiuppa, Burton, M.G., Caltabiano, T., Giudice, G., Guerrieri, S., Liuzzo, M., Filippo Murè and Salerno, G. (2010). Unusually large magmatic CO_2 gas emissions prior to a basaltic paroxysm. *Geophysical Research Letters*, 37(17), p.n/a-n/a. doi:https://doi.org/10.1029/2010gl043837.

3. Allison, C.M., Roggensack, K. and Clarke, A.B. (2019). H_2O–CO_2 solubility in alkali-rich mafic magmas: new experiments at mid-crustal pressures. *Contributions to Mineralogy and Petrology*, 174(7). doi: 10.1007/s00410-019-1592-4

4. Allison, C.M., Roggensack, K. and Clarke, A.B. (2022). MafiCH: a general model for H_2O–CO_2 solubility in mafic magmas. *Contributions to Mineralogy and Petrology*, 177(3). doi:https://doi.org/10.1007/s00410-022-01903-y.

5. Atsushi Toramaru (1995). Numerical study of nucleation and growth of bubbles in viscous magmas. *Journal of Geophysical Research*, 100(B2), pp.1913–1931. doi:https://doi.org/10.1029/94jb02775.

6. Baker, D.R., Freda, C., Brooker, R.A. and P. Scarlato (2005). Volatile diffusion in silicate melts and its effects on melt inclusions. *Annals of Geophysics*, 48(4-5). doi:https://doi.org/10.4401/ag-3227.

7. Baker, D.R. and Moretti, R. (2011). Modeling the solubility of sulfur in magmas: A 50-year old geochemical challenge. *Reviews in Mineralogy and Geochemistry*, 73(1), pp.167–213. doi: 10.2138/rmg.2011.73.7

8. Baker, L.L. and Rutherford, M.J. (1996). Sulfur diffusion in rhyolite melts. *Contributions to Mineralogy and Petrology*, 123(4), pp.335–344. doi:https://doi.org/10.1007/s004100050160.

9. Beaudry, P. and Grove, T.L. (2018). Sulfur partitioning in hydrous subduction zone magmas: a new experimental approach. *AGUFM*, 2018.

10. Behrens, H. (2010). Noble Gas Diffusion in Silicate Glasses and Melts. *Reviews in Mineralogy and Geochemistry*, 72(1), pp.227–267. doi:https://doi.org/10.2138/rmg.2010.72.6.

11. Behrens, H. and Stelling, J. (2011). Diffusion and Redox Reactions of Sulfur in Silicate Melts. *Reviews in mineralogy*

and geochemistry, 73(1), pp.79–111. doi:https://doi.org/10.2138/rmg.2011.73.4.

12. Bindeman, I.N., Deegan, F.M., Troll, V.R., Thordarson, T., Höskuldsson, Á., Moreland, W.M., Zorn, E.U., Shevchenko, A.V. and Walter, T.R. (2022). Diverse mantle components with invariant oxygen isotopes in the 2021 Fagradalsfjall eruption, Iceland. *Nature Communications*, 13(1), p.3737. doi:https://doi.org/10.1038/s41467-022-31348-7.

13. Blank, J.G. (1993). An experimental investigation of the behavior of carbon dioxide in rhyolitic melt. *California Institute of TechnologyProQuest Dissertations & Theses*.

14. Blank, J.G. and Brooker, R.A. (1994). Experimental studies of carbon dioxide in silicate melts; solubility, speciation, and stable carbon isotope behavior. *Reviews in Mineralogy & Geochemistry*, 30(1), pp.157–186.

15. Blower, J.D., Mader, H.M. and Wilson, S.D.R. (2001). Coupling of viscous and diffusive controls on bubble growth during explosive volcanic eruptions. *Earth and Planetary Science Letters*, 193(1-2), pp.47–56. doi:https://doi.org/10.1016/s0012-821x(01)00488-5.

16. Boulliung, J. and Wood, B.J. (2022). SO_2 solubility and degassing behavior in silicate melts. *Geochimica et Cosmochimica Acta*, 336, pp.150–164. doi:https://doi.org/10.1016/j.gca.2022.08.032.

17. Boulliung, J. and Wood, B.J. (2023). Sulfur oxidation state and solubility in silicate melts. *Contributions to mineralogy and petrology*, 178(8). doi:https://doi.org/10.1007/s00410-023-02033-9.

18. Brown, S.K., Loughlin, S.C., Sparks, R.S.J., Vye-Brown, C., Barclay, J., Calder, E., Cottrell, E., Jolly, G., Komorowski, J.-C., Mandeville, C., Newhall, C.G., Palma, J.L., Potter, S. and Valentine, G. (2015). Global volcanic hazard and risk. *Global Volcanic Hazards and Risk*, pp.81–172. doi: 10.1017/cbo9781316276273.004

19. Burgisser, A., Alletti, M. and Scaillet, B. (2015). Simulating the behavior of volatiles belonging to the C–O–H–S system in silicate melts under magmatic conditions with the software D-Compress. *Computers & Geosciences*, 79, pp.1–14. doi:https://doi.org/10.1016/j.cageo.2015.03.002.

20. Burnham, C.W. and Jahns, R.H. (1962). A method for determining the solubility of water in silicate melts. *American Journal of Science*, 260(10), pp.721–745. doi:https://doi.org/10.2475/ajs.260.10.721.

21. Burton, M., Allard, P., Muré, F. and La Spina, A. (2007). Magmatic gas composition reveals the source depth of slug-driven Strombolian explosive activity. *Science*, 317(5835), pp.227–230. doi: 10.1126/science.1141900

22. Carroll, M.R. and Holloway, J.R. (2018). *Volatiles in Magmas*. Walter de Gruyter GmbH & Co KG.

23. Cassidy, M., Manga, M., Cashman, K. and Bachmann, O. (2018). Controls on explosive-effusive volcanic eruption styles. *Nature Communications*, 9(1), p.2839. doi:https://doi.org/10.1038/s41467-018-05293-3.

24. Cole-Dai, J. (2010). Volcanoes and climate. *Wiley Interdisciplinary Reviews: Climate Change*, 1(6), pp.824–839. doi:https://doi.org/10.1002/wcc.76.

25. Colombier, M., Vasseur, J., Houghton, B.F., Cáceres, F., Scheu, B., Kueppers, U., Thivet, S., Gurioli, L., Montanaro, C., Soldati, A., Di Muro, A. and Dingwell, D.B. (2021). Degassing and gas percolation in basaltic magmas. *Earth and Planetary Science Letters*, 573, p.117134. doi:https://doi.org/10.1016/j.epsl.2021.117134.

26. Coumans, J.P., Llewellin, E.W., Wadsworth, F.B., Humphreys, M.C.S., Mathias, S.A., Yelverton, B.M. and Gardner, J.E. (2020). An experimentally validated numerical model for bubble growth in magma. *Journal of volcanology and geothermal research*, 402, pp.107002–107002. doi:https://doi.org/10.1016/j.jvolgeores.2020.107002.

27. Daði, A. (2021). Bulk density of the 2021 lava in Nátthagi, Reykjanes Peninsula, estimated with gravimetry. *Handle.net*. Available at: https://hdl.handle.net/1946/47116.

28. Ding, S., Plank, T., Wallace, P.J. and Rasmussen, D.J. (2023). Sulfur_X: A Model of Sulfur Degassing During Magma Ascent. *Geochemistry Geophysics Geosystems*, 24(4). doi:https://doi.org/10.1029/2022gc010552.

29. Dixon, J.E., Clague, D.A. and Stolper, E.M. (1991). Degassing History of Water, Sulfur, and Carbon in Submarine Lavas from Kilauea Volcano, Hawaii. *The Journal of Geology*, 99(3), pp.371–394. doi:https://doi.org/10.1086/629501.

30. Dixon, J., Stolper, E. and Stolloway, J. (1995). An Experimental Study of Water and Carbon Dioxide Solubilities in Mid-Ocean Ridge Basaltic Liquids. Part I: Calibration and Solubility Models. *Journal of Petrology*, 36. doi:https://doi.org/10.1093/oxfordjournals.petrology.a037267.

31. Dixon, J.E. and Stolper, E.M. (1995). An Experimental Study of Water and Carbon Dioxide Solubilities in Mid-Ocean Ridge Basaltic Liquids. Part II: Applications to Degassing. *Journal of Petrology*, 36(6). doi:https://doi.org/10.1093/oxfordjournals.petrolo

32. Duan, X. (2014). A general model for predicting the solubility behavior of H_2O–CO_2 fluids in silicate melts over a wide range of pressure, temperature and compositions. *Geochimica et Cosmochimica Acta*, 125, pp.582–609. doi:https://doi.org/10.1016/j.gca.2013.10.018.

33. Elias, T., Sutton, A.P., Stokes, J.B. and Casadevall, T.J. (1998). Sulfur dioxide emission rates of Kilauea Volcano, Hawaii, 1979-1997. *Open-file report /*. doi:https://doi.org/10.3133/ofr98462.

34. Fiege, A., Vetere, F., Iezzi, G., Simon, A. and Holtz, F. (2015). The roles of decompression rate and volatiles (H_2O + Cl ± CO_2± S) on crystallization in (trachy-) basaltic magma. *Chemical Geology*, 411, pp.310–322. doi:https://doi.org/10.1016/j.chemgeo.2015.07.016.

35. Fincham, C.J.B. and Richardson, F.D. (1954). The behaviour of sulphur in silicate and aluminate melts. *Proceedings of the Royal Society of London. Series A. Mathematical and Physical Sciences*, 223(1152), pp.40–62. doi:https://doi.org/10.1098/rspa.1954.0099.

36. Fleet, M.E. (2005). XANES Spectroscopy of Sulfur in Earth Materials. *The Canadian Mineralogist*, 43(6), pp.1811–1838. doi:https://doi.org/10.2113/gscanmin.43.6.1811.

37. Fogel, R.A. and Rutherford, M.J. (1990). The solubility of carbon dioxide in rhyolitic melts; a quantitative FTIR study. *American Mineralogist*, 75, pp.1311–1326.

38. Fortin, M.-A., Riddle, J., Desjardins-Langlais, Y. and Baker, D.R. (2015). The effect of water on the sulfur concentration at sulfide saturation (SCSS) in natural melts. *Geochimica et Cosmochimica Acta*, 160, pp.100–116. doi:https://doi.org/10.1016/j.gca.2015.03.022.

39. Fortin, M.-A., Watson, E.B., Stern, R.A. and Ono, S. (2019). Experimental characterization of diffusive and Soret isotopic fractionation of sulfur in a reduced, anhydrous basaltic melt. *Chemical Geology*, 510, pp.10–17. doi:https://doi.org/10.1016/j.chemgeo.2019.02.008.

40. Freda, C., Baker, D.R. and Scarlato, P. (2005). Sulfur diffusion in basaltic melts. *Geochimica et Cosmochimica Acta*, 69(21), pp.5061–5069. doi:https://doi.org/10.1016/j.gca.2005.02.002.

41. Gardner, J.E., Wadsworth, F.B., Carley, T.L., Llewellin, E.W., Kusumaatmaja, H. and Sahagian, D. (2022). Bubble Formation in Magma. *Annual Review of Earth and Planetary Sciences*, 51(1). doi: 10.1146/annurev-earth-031621-080308

42. Ghiorso, M.S. and Gualda, G.A.R. (2015). An H_2O–CO_2 mixed fluid saturation model compatible with rhyolite-MELTS. *Contributions to Mineralogy and Petrology*, 169(6). doi:https://doi.org/10.1007/s00410-015-1141-8.

43. Giada Iacono-Marziano, Yann Morizet, Emmanuel Le Trong and Gaillard, F. (2012). New experimental data and semi-

empirical parameterization of H_2O–CO_2 solubility in mafic melts. *Geochimica et Cosmochimica Acta*, 97, pp.1–23. doi:https://doi.org/10.1016/j.gca.2012.08.035.

44. Giordano, D., Russell, J.K. and Dingwell, D.B. (2008). Viscosity of magmatic liquids: A model. *Earth and Planetary Science Letters*, 271(1-4), pp.123–134. doi:https://doi.org/10.1016/j.epsl.2008.03.038.

45. Graf, Hans-F., Feichter, J. and Langmann, B. (1997). Volcanic sulfur emissions: Estimates of source strength and its contribution to the global sulfate distribution. *Journal of Geophysical Research: Atmospheres*, 102(D9), pp.10727–10738. doi:https://doi.org/10.1029/96jd03265.

46. Graham, K.A., Wing, B. and Baker, D.R. (2009). Sulfur Isotope Fractionation During Magmatic Degassing. *AGU Spring Meeting Abstracts*, 2009.

47. Guillaume Georgeais, Koga, K.T., Yves Moussallam and Rose-Koga, E.F. (2021). Magma Decompression Rate Calculations With EMBER: A User-Friendly Software to Model Diffusion of H_2O, CO_2, and S in Melt Embayments. *Geochemistry Geophysics Geosystems*, 22(7). doi:https://doi.org/10.1029/2020gc009542.

48. Hafsteinsdóttir, A.K. (2021). The effect of microlite crystallization on melt compositions and derived magma temperatures in the 2021 and 2022 Fagradalsfjall eruptions. *Handle.net*. Available at: 10.1946/46273

49. Halldórsson, S.A., Marshall, E.W., Caracciolo, A., Matthews, S., Bali, E., Rasmussen, M.B., Ranta, E., Robin, J.G., Guðfinnsson, G.H., Sigmarsson, O., Maclennan, J., Jackson, M.G., Whitehouse, M.J., Jeon, H., van der Meer, Q.H.A., Mibei, G.K., Kalliokoski, M.H., Repczynska, M.M., Rúnarsdóttir, R.H. and Sigurðsson, G. (2022). Rapid shifting of a deep magmatic source at Fagradalsfjall volcano, Iceland. *Nature*, 609(7927), pp.529–534. doi:https://doi.org/10.1038/s41586-022-04981-x.

50. Hamilton, D.L., Burnham, C.W. and Osborn, E.F. (1964). The Solubility of Water and Effects of Oxygen Fugacity and Water Content on Crystallization in Mafic Magmas. *Journal of Petrology*, 5(1), pp.21–39. doi:https://doi.org/10.1093/petrology/5.1.21.

51. Haughton, D.R., Roeder, P.L. and Skinner, B.J. (1974). Solubility of Sulfur in Mafic Magmas. *Economic Geology*, 69(4), pp.451–467. doi:https://doi.org/10.2113/gsecongeo.69.4.451.

52. Holloway, J.R. and Blank, J.G. (1994). Application of experimental results to C-O-H species in natural melts. *Reviews in Mineralogy & Geochemistry*, 30(1), pp.187–230.

53. Hughes, E.C., Saper, L.M., Liggins, P., St, H. and Stolper, E.M. (2022). The sulfur solubility minimum and maximum

in silicate melt. *Journal of the Geological Society*, 180(3). doi:https://doi.org/10.1144/jgs2021-125.

54. Hughes, E.C., Liggins, P., Saper, L. and Stolper, E.M. (2023). The effects of oxygen fugacity and sulfur on the pressure of vapor-saturation of mag. *American Mineralogist*, 109(3). doi:https://doi.org/10.2138/am-2022-8739.

55. Johnson, E.R., Wallace, P.J., Cashman, K.V. and Delgado Granados, H. (2010). Degassing of volatiles (H_2O, CO_2, S, Cl) during ascent, crystallization, and eruption at mafic monogenetic volcanoes in central Mexico. *Journal of Volcanology and Geothermal Research*, 197(1–4), pp.225–238. doi: 10.1016/j.jvolgeores.2010.02.017

56. Johnson, M.C., Anderson, A.T. and Rutherford, M.J. (1994). Pre-eruptive volatile contents of magmas. *Reviews in Mineralogy & Geochemistry*, 30(1), pp.281–330.

57. Larsen, J.F. and Gardner, J.E. (2004). Experimental study of water degassing from phonolite melts: implications for volatile oversaturation during magmatic ascent. *Journal of Volcanology and Geothermal Research*, 134(1-2), pp.109–124. doi:https://doi.org/10.1016/j.jvolgeores.2004.01.004.

58. Lerner, A., Wallace, P., Shea, T., Mourey, A.J., Kelly, P.J., Nadeau, P.A., Elias, T., Kern, C., Clor, L.E., Gansecki, C., R. Lopaka Lee, Moore, L.R. and Werner, C.A. (2021). The petrologic and degassing behavior of sulfur and other magmatic volatiles from the 2018 eruption of Kīlauea, Hawaii: melt concentrations, magma storage depths, and magma recycling. *Bulletin of Volcanology*, 83(6). doi:https://doi.org/10.1007/s00445-021-01459-y.

59. Lesne, P. Kohn, S.C., Blundy, J.D., Witham, F., Botcharnikov, R.E. and Behrens, H. (2011). Experimental Simulation of Closed-System Degassing in the System Basalt–H2O–CO2–S–Cl. *Journal of Petrology*, 52(9), pp.1737–1762. doi:https://doi.org/10.1093/petrology/egr027.

60. Liu, Y., Samaha, N.-T. and Baker, D.R. (2007). Sulfur concentration at sulfide saturation (SCSS) in magmatic silicate melts. *Geochimica et Cosmochimica Acta*, 71(7), pp.1783–1799. doi: 10.1016/j.gca.2007.01.004

61. Liu, Y., Zhang, Y. and Behrens, H. (2005). Solubility of H2O in rhyolitic melts at low pressures and a new empirical model for mixed H_2O–CO_2 solubility in rhyolitic melts. *Journal of Volcanology and Geothermal Research*, 143(1-3), pp.219–235. doi:https://doi.org/10.1016/j.jvolgeores.2004.09.019.

62. Lowenstern, J. (2001). Carbon dioxide in magmas and implications for hydrothermal systems. *Mineralium Deposita*, 36(6), pp.490–502. doi:https://doi.org/10.1007/s001260100185.

63. Mangan, M. and Sisson, T. (2000). Delayed, disequilibrium degassing in rhyolite magma: decompression ex-

periments and implications for explosive volcanism. *Earth and Planetary Science Letters*, 183(3-4), pp.441–455. doi:https://doi.org/10.1016/s0012-821x(00)00299-5.

64. Marini, L., Moretti, R. and Accornero, M. (2011). Sulfur Isotopes in Magmatic-Hydrothermal Systems, Melts, and Magmas. *Reviews in Mineralogy and Geochemistry*, 73(1), pp.423–492. doi: 10.2138/rmg.2011.73.14

65. Marshall, E.W., Caracciolo, A., Bali, E., Halldórsson, S.A., Matthews, S., Ranta, E., Rasmussen, M.B., Robin, J.G., Guðfinnson, G.H., Maclennan, J., C. Bosq, Auclair, D., O. Sigmarsson, Merrill, H., B. Gísladóttir, Johnson, S., N. Löw, Stracke, A. and Genske, F. (2024). The Petrology and Geochemistry of the 2021 Fagradalsfjall Eruption, Iceland: An Eruption Sourced From Multiple, Compositionally Diverse, Near-Moho Sills. *AGU Advances*, 5(6). doi:https://doi.org/10.1029/2024av001310.

66. Martel, C. and Schmidt, B.C. (2003). Decompression experiments as an insight into ascent rates of silicic magmas. *Contributions to Mineralogy and Petrology*, 144(4), pp.397–415. doi:https://doi.org/10.1007/s00410-002-0404-3.

67. Masotta, M., Keppler, H. and Chaudhari, A. (2016). Fluid-melt partitioning of sulfur in differentiated arc magmas and the sulfur yield of explosive volcanic eruptions. *Geochimica et Cosmochimica Acta*, 176, pp.26–43. doi:https://doi.org/10.1016/j.gca.2015.12.014.

68. Metcalfe, A., Séverine Moune, Moretti, R., Komorowski, J. and Aubry, T.J. (2023). Volatile emissions from past eruptions at La Soufrière de Guadeloupe (Lesser Antilles): insights into degassing processes and atmospheric impacts. *Frontiers in Earth Science*, 11. doi:https://doi.org/10.3389/feart.2023.1143325.

69. Moore, G. (2008). Interpreting H_2O and CO_2 contents in melt inclusions: Constraints from solubility experiments and modeling. *Reviews in Mineralogy and Geochemistry*, 69(1), pp.333–362. doi: 10.2138/rmg.2008.69.9

70. Muth, M.J. and Wallace, P.J. (2021). Slab-derived sulfate generates oxidized basaltic magmas in the southern Cascade arc (California, USA). *Geology*, 49(10), pp.1177–1181. doi:https://doi.org/10.1130/g48759.1.

71. Mysen, B.O. (1977). The solubility of H_2O and CO_2 under predicted magma genesis conditions and some petrological and geophysical implications. *Reviews of Geophysics*, 15(3), pp.351–361. doi: 10.1029/rg015i003p00351

72. Mysen, B.O., Arculus, R.J. and Eggler, D.H. (1975). Solubility of carbon dioxide in melts of andesite, tholeiite, and olivine nephelinite composition to 30 kbar pressure. *Contributions to Mineralogy and Petrology*, 53(4), pp.227–239. doi:https://doi.org/10.1007/bf00382441.

73. Nash, W.M., Smythe, D.J. and Wood, B.J. (2019). Compositional and temperature effects on sulfur speciation and solubility in silicate melts. *Earth and Planetary Science Letters*, 507, pp.187–198. doi: 10.1016/j.epsl.2018.12.006

74. Newman, S. and Lowenstern, J.B. (2002). VolatileCalc: a silicate melt–H_2O–CO_2 solution model written in Visual Basic for excel. *Computers & Geosciences*, 28(5), pp.597–604. doi:https://doi.org/10.1016/s0098-3004(01)00081-4.

75. Ni, H., Hui, H. and Steinle-Neumann, G. (2015). Transport properties of silicate melts. *Reviews of Geophysics*, 53(3), pp.715–744. doi:https://doi.org/10.1002/2015rg000485.

76. Nowak, M., Dominik Schreen and K. Spickenbom (2004). Argon and CO2 on the race track in silicate melts: A tool for the development of a CO_2 speciation and diffusion model. *Geochimica et Cosmochimica Acta*, 68(24), pp.5127–5138. doi:https://doi.org/10.1016/j.gca.2004.06.002.

77. O'Neill, H.St.C., Berry, A.J. and Mallmann, G. (2018). The oxidation state of iron in Mid-Ocean Ridge Basaltic (MORB) glasses: Implications for their petrogenesis and oxygen fugacities. *Earth and Planetary Science Letters*, 504, pp.152–162. doi:https://doi.org/10.1016/j.epsl.2018.10.002.

78. O'Neill, H.St.C. and Mavrogenes, J.A. (2022). The sulfate capacities of silicate melts. *Geochimica et Cosmochimica Acta*, 334, pp.368–382. doi:https://doi.org/10.1016/j.gca.2022.06.020.

79. Okumura, S. and Hirano, N. (2013). Carbon dioxide emission to Earth's surface by deep-sea volcanism. *Geology*, 41(11), pp.1167–1170. doi:https://doi.org/10.1130/g34620.1.

80. Okumura, S. and Nakashima, S. (2005). Water diffusion in basaltic to dacitic glasses. *Chemical Geology*, 227(1-2), pp.70–82. doi:https://doi.org/10.1016/j.chemgeo.2005.09.009.

81. Oppenheimer, C., Scaillet, B. and Martin, R.S. (2011). Sulfur Degassing From Volcanoes: Source Conditions, Surveillance, Plume Chemistry and Earth System Impacts. *Reviews in Mineralogy and Geochemistry*, 73(1), pp.363–421. doi:https://doi.org/10.2138/rmg.2011.73.13.

82. Papale, P., Moretti, R. and Barbato, D. (2006). The compositional dependence of the saturation surface of H_2O+CO_2 fluids in silicate melts. *Chemical Geology*, 229(1–3), pp.78–95. doi: 10.1016/j.chemgeo.2006.01.013

83. Parfitt, E.A. and Wilson, L. (1995). Explosive volcanic eruptions-IX. The transition between Hawaiian-style lava fountaining and Strombolian explosive activity. *Geophysical Journal International*, 121(1), pp.226–232. doi:https://doi.org/10.1111/j.1365-246x.1995.tb03523.x.

84. Proussevitch, A.A. and Sahagian, D.L. (1998). Dynamics and energetics of bubble growth in magmas: Analytical formulation and numerical modeling. *Journal of Geophysical Research: Solid Earth*, 103(B8), pp.18223–18251. doi:https://doi.org/10.1029/98jb00906.

85. Radu, I.-B., Henrik Skogby, Troll, V.R., Deegan, F.M., Geiger, H., Müller, D. and Þór Þórdarson (2023). Water in clinopyroxene from the 2021 Geldingadalir eruption of the Fagradalsfjall Fires, SW-Iceland. *Bulletin of Volcanology*, 85(5). doi:https://doi.org/10.1007/s00445-023-01641-4.

86. Ranta, E., Halldórsson, S.A., Óladóttir, B.A., Pfeffer, M.A., Caracciolo, A., Bali, E., Guðfinnsson, G.H., Kahl, M. and Barsotti, S. (2024). Magmatic Controls on Volcanic Sulfur Emissions at the Iceland Hotspot. *Geochemistry Geophysics Geosystems*, 25(5). doi:https://doi.org/10.1029/2024gc011443.

87. Rix, M., Valks, P., Hao, N., van Geffen, J., Clerbaux, C., Clarisse, L., Coheur, P.-F., Loyola R., D.G., Erbertseder, T., Zimmer, W. and Emmadi, S. (2009). Satellite Monitoring of Volcanic Sulfur Dioxide Emissions for Early Warning of Volcanic Hazards. *IEEE Journal of Selected Topics in Applied Earth Observations and Remote Sensing*, 2(3), pp.196–206. doi:https://doi.org/10.1109/jstars.2009.2031120.

88. Rose, W.I., Anderson, A.T., Woodruff, L.G. and Bonis, S.B. (1978). The October 1974 basaltic tephra from Fuego volcano: Description and history of the magma body. *Journal of Volcanology and Geothermal Research*, 4(1), pp.3–53. doi:https://doi.org/10.1016/0377-0273(78)90027-6.

89. Rose, W.I., Self, S., Murrow, P.J., Bonadonna, C., Durant, A.J. and Ernst, G. (2008). Nature and significance of small volume fall deposits at composite volcanoes: Insights from the October 14, 1974 Fuego eruption, Guatemala. *Bulletin of Volcanology*, 70(9), pp.1043–1067. doi:https://doi.org/10.1007/s00445-007-0187-5.

90. Ryan, A.G., Russell, J.K., Alexander R.L. Nichols, Hess, K.-U. and Porritt, L.A. (2015). Experiments and models on H_2O retrograde solubility in volcanic systems. *American Mineralogist*, 100(4), pp.774–786. doi:https://doi.org/10.2138/am-2015-5030.

91. Scaillet, B., Luhr, J.F. and Carroll, M.R. (2003). Petrological and volcanological constraints on volcanic sulfur emissions to the atmosphere. *Geophysical monograph*, pp.11–40. doi:https://doi.org/10.1029/139gm02.

92. Scholze, H. (1960). Zur Frage der Unterscheidung zwischen H2O-Molekeln und OH-Gruppen in Glasern und Mineralen. *Die Naturwissenschaften*, 47(10), pp.226–227. doi:https://doi.org/10.1007/bf00602759.

93. Scott, S., Pfeffer, M., Oppenheimer, C., Bali, E., Lamb, O.D., Barnie, T., Woods, A.W., Kjartansdóttir, R. and

Stefánsson, A. (2023). Near-surface magma flow instability drives cyclic lava fountaining at Fagradalsfjall, Iceland. *Nature Communications*, 14(1), p.6810. doi:https://doi.org/10.1038/s41467-023-42569-9.

94. Sharma, K., Blake, S., Self, S. and Krueger, A.J. (2004). SO2emissions from basaltic eruptions, and the excess sulfur issue. *Geophysical Research Letters*, 31(13), p.n/a-n/a. doi:https://doi.org/10.1029/2004gl019688.

95. Shea, T. (2017). Bubble nucleation in magmas: A dominantly heterogeneous process? *Journal of Volcanology and Geothermal Research*, 343, pp.155–170. doi:https://doi.org/10.1016/j.jvolgeores.2017.06.025.

96. Shi, P. and Saxena, S.K. (1992). Thermodynamic modeing of the C-H-O-S fluid system. *American Mineralogist*, 77(9-10), pp.1038–1049. Available at: https://pubs.geoscienceworld.org/msa/ammin/article-abstract/77/9-10/1038/42670/Thermodynamic-modeing-of-the-C-H-O-S-fluid-system.

97. Shinohara, H. (2008). Excess degassing from volcanoes and its role on eruptive and intrusive activity. *Reviews of Geophysics*, 46(4). doi:https://doi.org/10.1029/2007rg000244.

98. Shishkina, T.A., Botcharnikov, R.E., Holtz, F., Almeev, R.R., Jazwa, A.M. and Jakubiak, A.A. (2014). Compositional and pressure effects on the solubility of H2O and CO2 in mafic melts. *Chemical Geology*, 388, pp.112–129. doi:https://doi.org/10.1016/j.chemgeo.2014.09.001.

99. Sierralta, M., Nowak, M. and Keppler, H. (2002). The influence of bulk composition on the diffusivity of carbon dioxide in Na aluminosilicate melts. *American Mineralogist*, 87(11–12), pp.1710–1716. doi: 10.2138/am-2002-11-1221

100. Silver, L.L. and Stolper, E.M. (1989). Water in Albitic Glasses. *Journal of Petrology*, 30(3), pp.667–709. doi:https://doi.org/10.1093/petro

101. Silver, L.A., Ihinger, P.D. and Stolper, E. (1990). The influence of bulk composition on the speciation of water in silicate glasses. *Contributions to Mineralogy and Petrology*, 104(2), pp.142–162. doi: 10.1007/bf00306439

102. Sparks, R.S.J. (1978). The dynamics of bubble formation and growth in magmas: A review and analysis. *Journal of Volcanology and Geothermal Research*, 3(1-2), pp.1–37. doi:https://doi.org/10.1016/0377-0273(78)90002-1.

103. Stix, J., Zapata, A., V, M.C., Patricia, G., Fischer, T.P., M, D.G., M, L.N., V, M.O., E, A.O., C, R.T. and Williams, S.N. (1993). A model of degassing at Galeras Volcano, Colombia, 1988-1993. *Geology*, 21(11), pp.963–963. doi:https://doi.org/10.1130/0091-7613(1993)021%3C0963:amodag%3E2.3.co;2.

104. Stolper, E.M. (1982). The speciation of water in silicate melts. *Geochimica et Cosmochimica Acta*, 46(12),

pp.2609–2620. doi:https://doi.org/10.1016/0016-7037(82)90381-7.

105. Sun, C. and Yao, L. (2024). Redox equilibria of iron in low- to high-silica melts: A simple model and its applications to C-H-O-S degassing. *Earth and Planetary Science Letters*, 638, p.118742. doi:https://doi.org/10.1016/j.epsl.2024.118742.

106. Sutton, A.J., Elias, T., Gerlach, T.M. and Stokes, J.B. (2001). Implications for eruptive processes as indicated by sulfur dioxide emissions from Kılauea Volcano, Hawai'i, 1979–1997. *Journal of Volcanology and Geothermal Research*, 108(1-4), pp.283–302. doi:https://doi.org/10.1016/s0377-0273(00)00291-2.

107. Tait, S., Jaupart, C. and Vergniolle, S. (1989). Pressure, gas content and eruption periodicity of a shallow, crystallising magma chamber. *Earth and Planetary Science Letters*, 92(1), pp.107–123. doi: 10.1016/0012-821x(89)90025-3

108. Toramaru, A., Noguchi, S., Oyoshihara, S. and Tsune, A. (2008). MND (microlite number density) water exsolution rate meter. *Journal of Volcanology and Geothermal Research*, 175(1-2), pp.156–167. doi: 10.1016/j.jvolgeores.2008.03.035

109. Tuttle, O.F. and Bowen, N.L. (1958). *Origin of Granite in the Light of Experimental Studies in the System NaAlSi3O8–KAlSi3O8–SiO2–H2O*. *Memoir - Geological Society of America*. Geological Society of America. doi:https://doi.org/10.1130/mem74.

110. Wallace, P. and Carmichael, I.S.E. (1992). Sulfur in basaltic magmas. *Geochimica et Cosmochimica Acta*, 56(5), pp.1863–1874. doi:https://doi.org/10.1016/0016-7037(92)90316-b.

111. Wallace, P.J. (2001). Volcanic SO_2 emissions and the abundance and distribution of exsolved gas in magma bodies. *Journal of Volcanology and Geothermal Research*, 108(1-4), pp.85–106. doi:https://doi.org/10.1016/s0377-0273(00)00279-1.

112. Wallace, P.J. and Edmonds, M. (2011). The Sulfur Budget in Magmas: Evidence from Melt Inclusions, Submarine Glasses, and Volcanic Gas Emissions. *Reviews in Mineralogy and Geochemistry*, 73(1), pp.215–246. doi:https://doi.org/10.2138/rmg.2011.73.8.

113. Wallace, P.J., Plank, T., Edmonds, M. and Hauri, E.H. (2015). Volatiles in Magmas. *The Encyclopedia of Volcanoes*, pp.163–183. doi:https://doi.org/10.1016/b978-0-12-385938-9.00007-9.

114. Watson, E.B. (1991). Diffusion of dissolved CO2 and Cl in hydrous silicic to intermediate magmas. *Geochimica et Cosmochimica Acta*, 55(7), pp.1897–1902. doi:https://doi.org/10.1016/0016-7037(91)90031-y.

115. Watson, E.B., Wark, D.A. and Delano, J.W. (1993). Initial report on sulfur diffusion in magmas. *EOS*, 74, p.620.

116. Watson, I.M., Oppenheimer, C., Voight, B., Francis, P.W., Clarke, A., Stix, J., Miller, A., Pyle, D.M., Burton, M.R., Young, S.R., Norton, G., Loughlin, S., B. Darroux and Staff, M. (2000). The relationship between degassing and ground deformation at Soufriere Hills Volcano, Montserrat. *Journal of Volcanology and Geothermal Research*, 98(1-4), pp.117–126. doi:https://doi.org/10.1016/s0377-0273(99)00187-0.

117. Wendlandt, R.F. (1982). Sulfide saturation of basalt and andesite melts at high pressures and temperatures. *American Mineralogist*, 67, pp.877–885.

118. Witham, F., Blundy, J.D., Kohn, S.C., Priscille Lesne, Jacqueline Eaby Dixon, Churakov, S.V. and Botcharnikov, R.E. (2012). SolEx: A model for mixed COHSCl-volatile solubilities and exsolved gas compositions in basalt. *Computers & Geosciences*, 45, pp.87–97. doi:https://doi.org/10.1016/j.cageo.2011.09.021.

119. Yoshimura, S. (2015). Diffusive fractionation of H_2O and CO_2 during magma degassing. *Chemical Geology*, 411, pp.172–191. doi:https://doi.org/10.1016/j.chemgeo.2015.07.003.

120. Yves Moussallam, Rose-Koga, E.F., Fischer, T.P., Guillaume Georgeais, Lee, H.J., Birnbaum, J., Pfeffer, M.A., Talfan Barnie and Regis, E. (2024). Kinetic Isotopic Degassing of CO_2 During the 2021 Fagradalsfjall Eruption and the ^{13}C Signature of the Icelandic Mantle. *Geochemistry Geophysics Geosystems*, 25(12). doi:https://doi.org/10.1029/2024gc011997.

121. Zajacz, Z., Candela, P.A., Piccoli, P.M. and Sanchez-Valle, C. (2012). The partitioning of sulfur and chlorine between andesite melts and magmatic volatiles and the exchange coefficients of major cations. *Geochimica et Cosmochimica Acta*, 89, pp.81–101. doi:https://doi.org/10.1016/j.gca.2012.04.039.

122. Zhang, C. and Duan, Z. (2009). A model for C–O–H fluid in the Earth's mantle. *Geochimica et Cosmochimica Acta*, 73(7), pp.2089–2102. doi:https://doi.org/10.1016/j.gca.2009.01.021.

123. Zhang, L., Van, J.A. and Lacks, D.J. (2010). Molecular dynamics investigation of $MgO–CaO–SiO_2$ liquids: Influence of pressure and composition on density and transport properties. *Chemical Geology*, 275(1-2), pp.50–57. doi:https://doi.org/10.1016/j.chemgeo.2010.04.012.

124. Zhang, Y. (1999). H2O in rhyolitic glasses and melts: Measurement, speciation, solubility, and diffusion. *Reviews of Geophysics*, 37(4), pp.493–516. doi:https://doi.org/10.1029/1999rg900012.

125. Zhang, Y. and Gan, T. (2022). Diffusion in Melts and Magmas. *Reviews in Mineralogy and Geochemistry*, 87(1),

pp.283–337. doi:https://doi.org/10.2138/rmg.2022.87.07.

126. Zhang, Y. and Ni, H. (2010). Diffusion of H, C, and O Components in Silicate Melts. *Reviews in mineralogy and geochemistry*, 72(1), pp.171–225. doi:https://doi.org/10.2138/rmg.2010.72.5.

127. Zhang, Y. and Stolper, E.M. (1991). Water diffusion in a basaltic melt. *Nature*, 351(6324), pp.306–309. doi:https://doi.org/10.1038/351306

128. Zhang, Y., Stolper, E.M. and Wasserburg, G.J. (1991). Diffusion of water in rhyolitic glasses. *Geochimica et Cosmochimica Acta*, 55(2), pp.441–456. doi:https://doi.org/10.1016/0016-7037(91)90003-n.

129. Zhang, Y., Xu, Z., Zhu, M. and Wang, H. (2007). Silicate melt properties and volcanic eruptions. *Reviews of Geophysics*, 45(4). doi:https://doi.org/10.1029/2006rg000216.

Appendices

A Calculations and constants used in *Sulfur_X*

The following section contains the full calculations and constants used within *Sulfur_X*. For further explanation/clarification see the original python script published in Ding et al., (2023).

Table A shows the constants used in the calculations within *Sulfur_X*.

Constant	Value	Units
TK0	1673.15	K
A	0.196	–
B	11492	–
C	-6.675	–
DWFEO	-1.828	–
DWAL2O3	-2.243	–
DWCAO	3.201	–
DWNA2O	5.854	–
DWK2O	6.215	–
E	-3.36	–
F	-7.01×10^{-7}	kPa^{-1}
G	-1.54×10^{-10}	Pa^{-1}
H	3.85×10^{-17}	kPa^{-2}

Table A.1: *Constants used in the calculations within* Sulfur_X.

The calculation for *con* used in Equation 28 is as follows:

$$\begin{aligned}\text{con} \;&= \frac{B}{T} + C \\ &+ \Big(\text{DWAL2O3}\, X_{\text{Al}_2\text{O}_3} + \text{DWCAO}\, X_{\text{CaO}} + \text{DWNA2O}\, X_{\text{Na}_2\text{O}} + \text{DWK2O}\, X_{\text{K}_2\text{O}} + \text{DWFEO}\, X_{\text{FeO(T)}}\Big) \\ &+ E\left(1 - \frac{TK0}{T} - \log\frac{T}{TK0}\right) + F\,\frac{p_p}{T} + G\,\frac{(T - TK0)\,p_p}{T} + H\,\frac{p_p^2}{T}.\end{aligned} \tag{A.1}$$

Where X_i is the mole fraction of oxide i in the melt, T is the temperature in K and p_p is the system pressure in bar.

A.1 Fugacity coefficient calculations

The following section details the constants and calculations for the fugacity coefficients of SO_2, H_2S and H_2O.

A.1.1 SO_2

Name	Value	Units
P_0	1	bar
T_{cr}	430.95	K
P_{cr}	78.7295	bar

Table A.2: *Reference and critical values for calculating* ΦSO_2*. from Shi & Saxena, 1992*

Name	Value
$AQ_1 \ldots AQ_8$	$[\,0.92854,\ 0.043269,\ -0.24671,\ 0,\ 0.24999,\ 0,\ -0.53182,\ -0.016461\,]$
$BQ_1 \ldots BQ_8$	$[\,8.4866 \times 10^{-4},\ -1.8379 \times 10^{-3},\ 6.6787 \times 10^{-2},\ 0,\ -2.9427 \times 10^{-2},\ 0,\ 2.9003 \times 10^{-2},\ 5.4808 \times 10^{-3}\,]$
$CQ_1 \ldots CQ_8$	$[\,-3.5456 \times 10^{-4},\ 2.3316 \times 10^{-5},\ 9.4159 \times 10^{-3},\ 0,\ -8.1653 \times 10^{-3},\ 0,\ 2.3154 \times 10^{-3},\ 5.5542 \times 10^{-4}\,]$

Table A.3: *EOS coefficients for* SO_2 *(Shi & Saxena, 1992).*

Coefficient	Formula
A	$A = A_{Q1} + A_{Q2}\left(\frac{T}{T_{\mathrm{cr}}}\right) + A_{Q3}\left(\frac{T}{T_{\mathrm{cr}}}\right)^{-1} + A_{Q4}\left(\frac{T}{T_{\mathrm{cr}}}\right)^{2} + A_{Q5}\left(\frac{T}{T_{\mathrm{cr}}}\right)^{-2}$ $+A_{Q6}\left(\frac{T}{T_{\mathrm{cr}}}\right)^{3} + A_{Q7}\left(\frac{T}{T_{\mathrm{cr}}}\right)^{-3} + A_{Q8}\ln\left(\frac{T}{T_{\mathrm{cr}}}\right)$
B	$B = B_{Q1} + B_{Q2}\left(\frac{T}{T_{\mathrm{cr}}}\right) + B_{Q3}\left(\frac{T}{T_{\mathrm{cr}}}\right)^{-1} + B_{Q4}\left(\frac{T}{T_{\mathrm{cr}}}\right)^{2} + B_{Q5}\left(\frac{T}{T_{\mathrm{cr}}}\right)^{-2}$ $+B_{Q6}\left(\frac{T}{T_{\mathrm{cr}}}\right)^{3} + B_{Q7}\left(\frac{T}{T_{\mathrm{cr}}}\right)^{-3} + B_{Q8}\ln\left(\frac{T}{T_{\mathrm{cr}}}\right)$
C	$C = C_{Q1} + C_{Q2}\left(\frac{T}{T_{\mathrm{cr}}}\right) + C_{Q3}\left(\frac{T}{T_{\mathrm{cr}}}\right)^{-1} + C_{Q4}\left(\frac{T}{T_{\mathrm{cr}}}\right)^{2} + C_{Q5}\left(\frac{T}{T_{\mathrm{cr}}}\right)^{-2}$ $+C_{Q6}\left(\frac{T}{T_{\mathrm{cr}}}\right)^{3} + C_{Q7}\left(\frac{T}{T_{\mathrm{cr}}}\right)^{-3} + C_{Q8}\ln\left(\frac{T}{T_{\mathrm{cr}}}\right)$

Table A.4: *Formulas for A, B, and C where T is the temperature in K.*

The calculations for Φ_{SO_2} are as follows:

$$Z_{\mathrm{comp}} = A\ln\left(\frac{P/P_{\mathrm{cr}}}{P_0/P_{\mathrm{cr}}}\right) + B\left(\frac{P}{P_{\mathrm{cr}}} - \frac{P_0}{P_{\mathrm{cr}}}\right) + \frac{C}{2}\left[\left(\frac{P}{P_{\mathrm{cr}}}\right)^2 - \left(\frac{P_0}{P_{\mathrm{cr}}}\right)^2\right] \tag{A.2}$$

$$\ln\Phi_{\mathrm{SO_2}} = Z_{\mathrm{comp}} - \ln(P) \tag{A.3}$$

Where P is the system pressure in bar.

A.1.2 H_2S

Name	Value	Units
P_0	1	bar
T_{cr}	373.55	K
P_{cr}	90.0779	bar

Table A.5: *Reference and critical values for calculating* $\Phi_{\mathrm{H_2S}}$ *(Shi & Saxena, 1992).*

Name	Value
$AQ_1 \dots AQ_8$	$[\,0.59941,\ -1.5570\times10^{-3},\ 4.5250\times10^{-2},\ 0,\ 3.6687,\ 0,\ -7.9248,\ 2.6058\,]$
$BQ_1 \dots BQ_8$	$[\,2.2545\times10^{-2},\ 1.7473\times10^{-3},\ 4.8253\times10^{-2},\ 0,\ -1.9890\times10^{-2},\ 0,\ 3.2794\times10^{-2},\ -1.0985\times10^{-2}\,]$
$CQ_1 \dots CQ_8$	$[\,5.7375\times10^{-3},\ -2.0944\times10^{-6},\ -1.1894\times10^{-2},\ 0,\ 1.4661\times10^{-2},\ 0,\ -7.5605\times10^{-3},\ -2.7985\times10^{-3}\,]$

Table A.6: *EOS coefficients for* H_2S *(Shi & Saxena, 1992).*

Coefficient	Formula
A	$A = A_{Q1} + A_{Q2}\left(\frac{T}{T_{\mathrm{cr}}}\right) + A_{Q3}\left(\frac{T}{T_{\mathrm{cr}}}\right)^{-1} + A_{Q4}\left(\frac{T}{T_{\mathrm{cr}}}\right)^{2} + A_{Q5}\left(\frac{T}{T_{\mathrm{cr}}}\right)^{-2} + A_{Q6}\left(\frac{T}{T_{\mathrm{cr}}}\right)^{3} + A_{Q7}\left(\frac{T}{T_{\mathrm{cr}}}\right)^{-3} + A_{Q8}\,\ln\left(\frac{T}{T_{\mathrm{cr}}}\right)$
B	$B = B_{Q1} + B_{Q2}\left(\frac{T}{T_{\mathrm{cr}}}\right) + B_{Q3}\left(\frac{T}{T_{\mathrm{cr}}}\right)^{-1} + B_{Q4}\left(\frac{T}{T_{\mathrm{cr}}}\right)^{2} + B_{Q5}\left(\frac{T}{T_{\mathrm{cr}}}\right)^{-2} + B_{Q6}\left(\frac{T}{T_{\mathrm{cr}}}\right)^{3} + B_{Q7}\left(\frac{T}{T_{\mathrm{cr}}}\right)^{-3} + B_{Q8}\,\ln\left(\frac{T}{T_{\mathrm{cr}}}\right)$
C	$C = C_{Q1} + C_{Q2}\left(\frac{T}{T_{\mathrm{cr}}}\right) + C_{Q3}\left(\frac{T}{T_{\mathrm{cr}}}\right)^{-1} + C_{Q4}\left(\frac{T}{T_{\mathrm{cr}}}\right)^{2} + C_{Q5}\left(\frac{T}{T_{\mathrm{cr}}}\right)^{-2} + C_{Q6}\left(\frac{T}{T_{\mathrm{cr}}}\right)^{3} + C_{Q7}\left(\frac{T}{T_{\mathrm{cr}}}\right)^{-3} + C_{Q8}\,\ln\left(\frac{T}{T_{\mathrm{cr}}}\right)$

Table A.7: *Formulas for A, B, and C, where T is the temperature in K.*

The calculations for $\Phi_{\mathrm{H_2S}}$ are as follows:

$$Z_{\mathrm{comp}} = A \ln\left(\frac{P/P_{\mathrm{cr}}}{P_0/P_{\mathrm{cr}}}\right) + B\left(\frac{P}{P_{\mathrm{cr}}} - \frac{P_0}{P_{\mathrm{cr}}}\right) + \frac{C}{2}\left[\left(\frac{P}{P_{\mathrm{cr}}}\right)^2 - \left(\frac{P_0}{P_{\mathrm{cr}}}\right)^2\right] \tag{A.4}$$

$$\ln \Phi_{\mathrm{H_2S}} = Z_{\mathrm{comp}} - \ln(P) \tag{A.5}$$

where P is the system pressure in bar and T the temperature in K.

A.1.3 H_2O

Name	Value	Units
P_0	1	bar
ε	510	–
σ	2.88	–
R	0.08314467	$\mathrm{cm^3\,bar\,K^{-1}\,mol^{-1}}$

Table A.8: *Reference constants for calculating* Φ_{H_2O} *(Zhang & Duan, 2009).*

Coefficient	Value
a_1	$2.95177298930 \times 10^{-2}$
a_2	$-6.33756452413 \times 10^{3}$
a_3	$-2.75265428882 \times 10^{5}$
a_4	$1.29128089283 \times 10^{-3}$
a_5	$-1.45797416153 \times 10^{2}$
a_6	$7.65938947237 \times 10^{4}$
a_7	$2.58661493537 \times 10^{-6}$
a_8	0.52126532146
a_9	$-1.39839523753 \times 10^{2}$
a_{10}	$-2.36335007175 \times 10^{-8}$
a_{11}	$5.35026383543 \times 10^{-3}$
a_{12}	-0.27110649951
a_{13}	$2.50387836486 \times 10^{4}$
a_{14}	0.73226726041
a_{15}	$1.54833359970 \times 10^{-2}$

Table A.9: *EOS coefficients for* H_2O *(Zhang & Duan, 2009).*

The reduced variables are defined as

$$P_m = \frac{3.0636\,\sigma^3\,P}{\varepsilon}, \qquad T_m = \frac{154\,T}{\varepsilon}. \tag{A.6}$$

where P is the system pressure in bar, and T the temperature in K.

The pressure as a function of molar volume V_m is defined as:

$$\begin{aligned} P_{\text{calc}}(V_m) = \Bigg[1 &+ \frac{a_1 + a_2/T_m^2 + a_3/T_m^3}{V_m} + \frac{a_4 + a_5/T_m^2 + a_6/T_m^3}{V_m^2} + \frac{a_7 + a_8/T_m^2 + a_9/T_m^3}{V_m^4} \\ &+ \frac{a_{10} + a_{11}/T_m^2 + a_{12}/T_m^3}{V_m^5} + \frac{a_{13}}{T_m^3 V_m^2}\left(a_{14} + \frac{a_{15}}{V_m^2}\right) e^{-a_{15}/V_m^2} \Bigg] \frac{RT_m}{V_m}. \end{aligned} \tag{A.7}$$

$P_{\text{calc}}(V_m) \approx P_m$ is then iteratively solved to find V_m. This is then used in Equation A.8:

$$Z = \frac{P_m V_m}{RT_m}. \tag{A.8}$$

The fugacity coefficient is then calculated using:

$$\ln \Phi_{\text{H}_2\text{O}} = Z - 1 - \ln Z + S_1 \tag{A.9}$$

where S_1 is defined as:

$$\begin{aligned} S_1 = &\frac{a_1 + a_2/T_m^2 + a_3/T_m^3}{V_m} + \frac{a_4 + a_5/T_m^2 + a_6/T_m^3}{2V_m^2} + \frac{a_7 + a_8/T_m^2 + a_9/T_m^3}{4V_m^4} \\ &+ \frac{a_{10} + a_{11}/T_m^2 + a_{12}/T_m^3}{5V_m^5} + \frac{a_{13}}{2a_{15}T_m^3}\left[a_{14} + 1 - \left(a_{14} + 1 + \frac{a_{15}}{V_m^2}\right) e^{-a_{15}/V_m^2}\right]. \end{aligned} \tag{A.10}$$

A.2 Calculations for kd_1 and kd_2

In order to calculate the two partition coefficients, the residuals for each reaction occurring (RXNI and RXNII) are required (Equations 35 and 36).

Name	Value	Units
R	8.3145	J K^{-1} mol^{-1}
$\Delta V_{\text{RXN I}}$	13.35 – 22.1	–
$P_{0,\text{RXN I}}$	200	MPa
$T_{0,\text{RXN I}}$	1000	°C
$\Delta V_{\text{RXN II}}$	-49.5	–
$\Delta H_{\text{RXN II}}$	32379	–
$P_{0,\text{RXN II}}$	200	MPa
$T_{0,\text{RXN II}}$	1100	°C

Table A.10: *Constants for calculating the residuals of RXNI and RXNII.*

Name	Formula	Units
Excess Ca	$2X_{\mathrm{CaO}} - X_{\mathrm{Al_2O_3}}$	–
Excess Na	$X_{\mathrm{Na_2O}} - X_{\mathrm{Al_2O_3}}$	–
NBO (non-bridging oxygens)	$\dfrac{\text{total oxygen} - 4\,(X_{\mathrm{SiO_2}} + X_{\mathrm{TiO_2}} + X_{\mathrm{Al_2O_3}} + X_{\mathrm{P_2O_5}})}{X_{\mathrm{SiO_2}} + X_{\mathrm{TiO_2}} + X_{\mathrm{Al_2O_3}} + X_{\mathrm{P_2O_5}}}$	–

Table A.11: *Derived compositional parameters used in calculations for the residuals of RXNI and RXNII, where X_i is the mole fraction of oxide i in the melt.*

The enthalpy term for RXNI is calculated as follows:

$$\Delta H_{\mathrm{RXN\,I}} = \frac{-0.4739\,(T_{0,\mathrm{RXN\,I}} + 273.15) + 45431}{R} \tag{A.11}$$

The residual of RXNI is calculated using Equation A.12:

$$\begin{aligned}
\mathrm{residual}_{\mathrm{RXN\,I}} = 0.616843 &+ \big(20.844\,(X_{\mathrm{H_2O}})^2 - 8.7151\,X_{\mathrm{FeO(T)}}\big) \\
&- \frac{\Delta V_{\mathrm{RXN\,I}}}{RT}\left(\frac{P_b}{10} - P_{0,\mathrm{RXN\,I}}\right) \\
&- \Delta H_{\mathrm{RXN\,I}}\left(\frac{1}{T} - \frac{1}{T_{0,\mathrm{RXN\,I}} + 273.15}\right) \\
&+ \ln(P_b\,\Phi_{\mathrm{H_2O}}) - \ln(X_{\mathrm{FeO(T)}}) \\
&- \frac{1}{RT}\bigg[(1 - X_{\mathrm{FeO(T)}})^2\Big(28870 - 14710X_{\mathrm{MgO}} + 1960X_{\mathrm{CaO}} \\
&\qquad + 43300X_{\mathrm{Na_2O}} + 95380X_{\mathrm{K_2O}} - 76880X_{\mathrm{TiO_2}}\Big) \\
&\qquad + (1 - X_{\mathrm{FeO(T)}})\Big(-62190X_{\mathrm{SiO_2}} + 31520(X_{\mathrm{SiO_2}})^2\Big)\bigg] \\
&- \ln(P_b\,\Phi_{\mathrm{H_2S}}).
\end{aligned} \tag{A.12}$$

where T is the temperature in K.

The residual of RXNII is calculating using Equation A.13:

$$\begin{aligned}
\mathrm{residual}_{\mathrm{RXN\,II}} = &-0.2394 - \frac{\Delta V_{\mathrm{RXN\,II}}}{RT}\left(\frac{P_b}{10} - P_{0,\mathrm{RXN\,II}}\right) \\
&- \Delta H_{\mathrm{RXN\,II}}\left(\frac{1}{T} - \frac{1}{T_{0,\mathrm{RXN\,II}} + 273.15}\right) \\
&- \ln(\Phi_{\mathrm{SO_2}}) - \ln(P_b) \\
&- 8.9170\,(\text{excess Ca}) - 21.7846\,(\text{excess Na}) - 1.715\,(\text{NBO}).
\end{aligned} \tag{A.13}$$

where T is the temperature in K, and P_b is the system pressure in bar.

B Compositional inputs in the bubble-growth model

For Fagradalsfjall from Bindeman et al., (2022):

Oxide	wt%
SiO_2	49.03
TiO_2	1.05
Al_2O_3	15.07
FeO(T)	11.00
MnO	0.17
MgO	8.98
CaO	12.55
Na_2O	1.84
K_2O	0.20
P_2O_5	0.11
F_2O^{-1}	0

Table B.1: *Major element composition of Fagradalsfjall 2021 used in the bubble-growth model (Bindeman et al., 2022).*

For Fuego from Ding et al., (2023):

Oxide	wt.%
SiO_2	50.39
TiO_2	0.93
Al_2O_3	17.21
FeO(T)	10.51
MnO	0.17
MgO	5.20
CaO	8.51
Na_2O	2.83
K_2O	0.46
P_2O_5	0.21
F_2O^{-1}	0

Table B.2: *Major element composition of Fuego volcano used in the bubble-growth model (Ding et al., 2023).*

C Model Instructions

The model code is available as a supplementary folder.

The model consists of three core scripts: Bubble_Growth_Modelling_v2, getFunctions_v2, and Numerical_Model_v2. The other scripts contain component solubility models, and functions for finding saturation pressures, all of which are called from the main script.

The main script is Bubble_Growth_Modelling_v2. This is the only script that requires editing in order to customise a model run. It contains all of the input values, and existing component models can be switched on/off by commenting out lines. This works identically to the original Coumans et al., (2020) model (the instructions for which are open source), the only difference being the additional input values for multiple volatiles. The model is currently set to run equilibrium conditions of Fagradalsfjall 2021 (Table 5).

The script getFunctions_v2 contains and calls all the necessary functions for the model, depending on the set component models. Numerical_Model_v2 contains the model itself, and outputs the results back to Bubble_Growth_Modelling_v2, which produces the final figures. There are many figures available at the end of this script which can be commented in/out, but the model is currently set to output the most comprehensive overview of the model run.

In order to change the model to find the saturation pressure and initial gas mole fractions of each volatile (recommended before a full model run, to ensure the system starts in equilibrium), the operation switch at the beginning of the main script can be changed to 'Find Psat'. The model will then calculate the saturation pressure and mole fractions, and putting a breakpoint at line 238 is recommended to copy and paste these values into the inputs section. The model is currently set to start at saturation and equilibrium for Fagradalsfjall 2021.

All of these files are .m scripts, and so must be ran in MATLAB. For more detailed instructions on how to use the model see Coumans et al., (2020).